Epitaxy, Thin lms and Superlattices

Christensen, Morten Jagd

Publication date:
1997

Document Version
Publisher's PDF, also known as Version of record

Risø–R–980(EN)

Epitaxy, Thin films and Superlattices

Morten Jagd Christensen

Risø National Laboratory, Roskilde, Denmark
May 1997

Abstract This report contains the result of structural investigations of 3d transition metal superlattices consisting of Fe/V, Cr/Mn, V/Mn and Fe/Mn, and a structural and magnetic study of a series of Ho/Pr alloys.

The work includes preparation and characterization of substrates as well as growth of thin films and Fe/V superlattices by molecular beam epitaxy, including in-situ characterization by reflection high energy electron diffraction and Auger electron spectroscopy. Structural characterization has been done by x-ray diffraction and neutron diffraction. The x-ray diffraction experiments have been performed at the rotating copper anode at Risø, and at synchrotron facilities in Hamburg and Brookhaven, and the neutron scattering was done at the Danish Research Reactor DR3 at Risø. In addition to longitudinal scans, giving information about the structural parameters in the modulation direction, non-specular scans were also performed. This type of scans gives information about in-plane orientation and structure.

From the analysis, structural information about lattice parameters, epitaxial strain, coherence lengths and crystallographic orientation is obtained for the superlattice systems, except Fe/Mn superlattices, which could not be modelled. For the Ho/Pr alloys, x-ray magnetic scattering was performed, and the crystal and magnetic structures were investigated.

This thesis, *"Epitaxy, Thin films and Superlattices"*, is written in partial fulfillment of the requirements for obtaining a Ph.D degree in physics at the University of Copenhagen. The supervisors were Robert Feidenhans'l at Risø National Laboratory, Allan Mackintosh and Poul Erik Lindelof at the University of Copenhagen.

The Ph.D thesis is partly based on four papers, three on 3d transition metal superlattices and one on Ho/Pr alloys. One of these has recently been submitted for publication and one is in preparation. These papers are listed in section 6. Other involvements during the Ph.D. work, has resulted in the following papers which are not regarded a part of the thesis:

- Hansen L-U W, Christensen M J and Mosekilde E 1995 *Physica Scripta* **51** 35
- Gidalevitz D, Feidenhans'l R, Matlis S, Smilgies D, Christensen M J, Leiserowitz L 1997 *Angewandte Chemie: november issue*
- McMorrow D, Lussier J-G, Lebech B, Sørensen S Aa, Christensen M J and Vogt O 1997 *J. Phys.: Condens. Matter* **9** 1133

ISBN 87–550–2298–7
ISSN 0106–2840

Grafisk Service · Risø · 1997 Typeset in LaTeX

Contents

"Every successful person has had failures but repeated failure is no guarantee of eventual success."

–Anonymous

1 Introduction

Artificially grown superlattices and multilayers are layered structures with dimensions from a few Å to thousands of Å.

Multilayer investigations can be said to originate with the work of DuMond and Youtz in 1940 [21]. As a part of the investigation of diffusion of copper in gold, artificial thin films of varying Cu/Au concentration were grown. By analyzing the decay of the diffraction peaks, measured by x-ray diffraction, they were able to measure diffusion constants of 10^{-20}cm^2/s, eight orders of magnitudes smaller than so far measurable.

Another study of metallic multilayers in 1969 investigated the predicted breakdown of the law for chemical diffusion when the chemical gradients were steep. The prediction was confirmed and furthermore, large anomalies in the elastic modulus were observed for certain modulation lengths. These results are reviewed in 1979 [39].

In the 70s, semiconductor superlattices were successfully grown. The nearly identical lattice parameters, within 1%, produced epitaxial superlattices with large coherence lengths.

The first metal superlattices can be said to be grown in 1980. Here, it was demonstrated that two elements, with a large lattice mis-match and different crystal structures, such as Nb and Cu, could be grown in coherent structures. The structure, at the time denoted LUCS for Layered Ultrathin Coherent Structures, produced clear superlattice modulations in high angle x-ray diffraction [77].

Figure 1 shows two modulated structures. For clarity they are represented as two-dimensional structures. The top figure, shows a periodic stacking of two materials with a sharp chemical modulation. This structure will qualify to the description superlattice. The bottom figure shows a concentration variation, and is neither a superlattice nor a multilayer. There is a distinction between superlattices and multilayers. Loosely defined, a superlattice is atomically ordered in all three directions, where a multilayer is ordered along the modulation direction only. It has been common practice, however, to accept the usage of the word superlattice, even for multilayered structures where one component is amorphous. We will not distinguish rigorously between superlattices, modulated structures and multilayers.

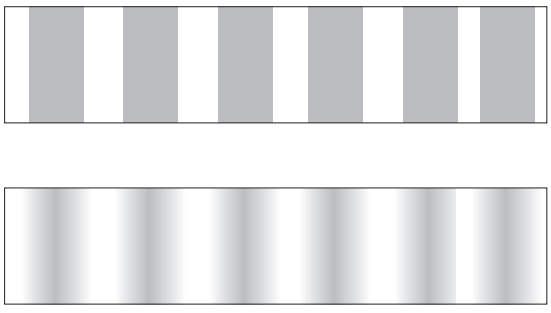

Figure 1. Two chemically modulated structures. Top: multilayer with a sharp chemical modulation. Bottom: A sinusoidal chemical modulation.

1.1 Physical properties of superlattices

The possibility to engineer artificial superlattices, grown one atomic plane at a time, has offered new model systems for investigation. The targets for investigations are structural properties, magnetic properties, transport properties, electronic structure, etc.

It is possible to stabilize new structures, such as fcc Fe and bcc Mn, in thin layers surrounded by appropriate spacer materials. Superlattices offer the possibility to grow such metastable structures in 'bulk' quantities for measurement. Such structures are often tetragonally distorted because of in-plane lattice expansions or compressions.

Giant magnetoresistance was first seen in Fe/Cr superlattices [5, 7], and is an example of new physical properties observed in these systems. A magnetoresistance of 50% was observed. For comparison, the widely used $Ni_{80}Fe_{20}$ permalloy has a magnetoresistance of 2%. Values as high as 120% in Co/Cu superlattices have been observed [79].

Magnetic properties of superlattices are of great interest. Interface magnetism, magnetism in two-dimensional systems and magnetic coupling across nonmagnetic spacers are all hot topics. Oscillatory behavior of giant magnetoresistance and exchange coupling, as a function of spacer thickness, in Co/Ru, Co/Cr and Fe/Cr superlattices has been seen [70]. Although the initial discrepancy with the oscillation periods predicted by RKKY theory has been explained, an exhaustive theory still remains to be made.

Long range magnetic order is abundant in rare earth superlattices. These systems have shown a wealth of magnetic structures, like ferromagnets, basal-plane antiferromagnets, cones, longitudinally modulated structures and such odd behaviors as the helifan [45]. Gd/Y superlattices, with a quasiperiodic modulation created from the Fibonacci sequences, have shown hard magnetic behavior, with high saturation fields at low temperatures [59].

Another physical property observed in superlattices, is the supermodulus effect mentioned earlier [39, 84]. The supermodulus effect is named so, because enhancements of the biaxial modulus of several hundred percent have been observed.

1.2 Applications

It is not an exaggeration to say that most of todays technology is influenced, directly or indirectly, by thin film technology. The semiconductor based, chip technology is the main example, but not the only one. Information storage and retrieval in the form of magnetic tapes and harddisks is another. Coatings of various complexity, from corrosion protection in thick Cr layers, to the multilayered coatings used in camera optics, are other examples. New usages regularly appear on the market.

Just as multilayered structures of transparent compounds are used in optics for visible light, multilayers are used in x-ray and neutron optics to produce supermirrors [6]. For x-rays, these multilayers are composed of layers with alternating high and low electron density. Examples are Au/C and W/Si. For neutrons, the materials are chosen to provide a large contrast in the scattering lengths. Neutron supermirrors of Co/Ti multilayers and Fe/Ni superlattices are used as neutron polarizers, to select one spin component from a neutron beam. At the Danish research reactor DR3, a Ti/Ni supermirror is used to guide neutrons from the reactor to a neighboring building, where diffraction experiments can be performed.

Present day magnetic storage media are based on magnetoresistance: as a 'bit' sweeps by the reading head the resistance changes. In order to accommodate the demand for increasing capacity, the technology faces the task of developing reading/writing heads with good signal to noise ratios and higher sensitivities. Giant magneto resistance will be likely to play an important role in this development [24].

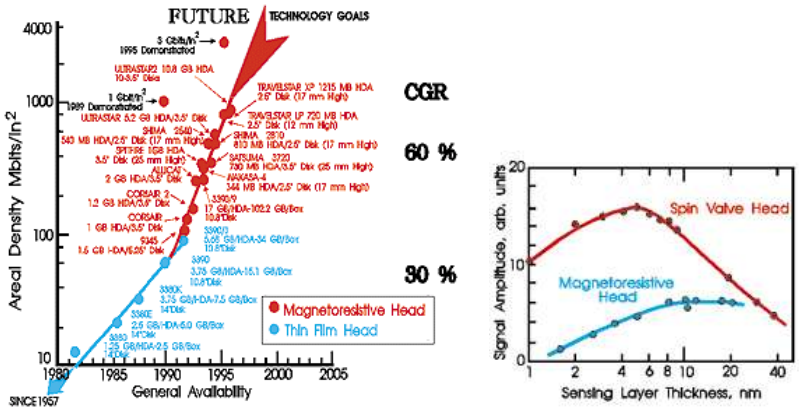

Figure 2. Magnetoresistance materials have taken the lead in reading head technology for storage media. (Ed Grochowsky, IBM Research Division, Almaden Research Center)

Si/SiO_2 superlattices have been demonstrated to emit light, tunable by changing the modulation length. Such achievements offers the possibility of integration of electronics and photonics [57]. The potential application of such a combination, could be massively parallel optical processing in future computers.

The bandpass characteristics of superlattices made up from $GaAs/Al_xGa_{1-x}As$ have been applied to infrared detectors. This has improved both the dark current and the sensitivity [13].

1.3 Theoretical work

In order to explain or predict physical properties occurring in superlattice and multilayer structures, much theoretical work has been done. We here give a few examples of physical properties which has been investigated theoretically.

In a theoretical investigation of modulated structures in 1965, diffraction from such systems was modelled by analogue electronic circuits with the 'diffracted intensity' connected to an oscilloscope. Here several different modulations were considered, among which, the square modulation corresponding to a modern superlattice. The characteristic appearance of the diffraction pattern from superlattices are illustrated here [17].

Band structure calculations of transition metal superlattices, have been used to investigate the distribution of the magnetic moments throughout the atomic layers (see for example [34]).

Theoretical arguments, based on the equations governing interdiffusion and surface mobility, have led to an estimate of the optimal growth temperature for metallic superlattices [26].

Diffraction from quasiperiodic superlattices is another example of theoretical exercises. Here a general method is given, for determining the relative intensity of

the Bragg reflections, from multilayered structures created by *two letter substitution rules* [46].

Theoretical work on magnetoresistance in superlattices and multilayers has also been done. Both for semiconductor superlattices [68] and for magnetic/nonmagnetic superlattices [96].

1.4 Experimental methods

A large number of experimental techniques are available for the investigation of superlattices. The techniques range from surface structure and surface magnetism probes, to traditional tools probing bulk properties.

Surface structure is determined by techniques, such as Reflection High Energy Electron Diffraction (RHEED), Low Energy Electron Diffraction (LEED), Atomic Force Microscopy (AFM) and Scanning Tunneling Microscopy (STM), whereas surface composition can be determined by Auger Electron Spectroscopy (AES) and X-ray Photoelectron Spectroscopy (XPS). Surface magnetism is determined by probes like spin polarized electron diffraction techniques, such as polarized Auger spectroscopy, XPS, LEED and Electron Energy-Loss Spectroscopy (EELS). Scanning Electron Microscopy with Polarization Analysis (SEMPA) is an impressive technique, which can directly image the magnetic domains on the surface.

Among bulk magnetic probes are neutron diffraction, Mössbauer spectroscopy, magnetometry, magneto optical Kerr effect and Magnetic Circular X-ray Dichroism (MCXD). The last two techniques involves rotation of the polarization of the radiation scattered or reflected from magnetized thin films.

For non destructive investigation of bulk structural properties, there is a choice between x-ray and neutron scattering. X-ray diffraction is certainly the most used technique, but neutron diffraction is often used for magnetic investigations in a supplementary way. Both techniques can be made surface sensitive, however, this requires high intensity beams, and is rarely used in superlattice investigations. Transmission Electron Microscopy (TEM) has been used to directly image the superlattice layers, but generally involves the destruction of part of the superlattice.

1.5 Scope and outline

This thesis will be organized as follows: In section 2 the basic theory of x-ray scattering will be outlined. The focus will be on diffraction from atoms and simple lattices. We will also describe the equations for diffractometry. Section 3 is an introduction to the MBE equipment at Risø. The analysis tools integrated in the system will also be mentioned. The principles of thin film growth and epitaxy is the theme in section 4, where also substrate structure and preparation is described. Finally, one example of thin film growth and characterization is given. In section 5 we consider diffraction from superlattices. This includes an overview of current superlattice models. We also consider superlattice diffraction in nonstandard scanning geometries. Section 6 is a short introduction to the experimental platforms which have been used as part of this work, leading up to the following four sections describing work on selected systems. One such system is the Fe/V superlattice system described in section 7. Section 8 is a study of Cr/Mn superlattices, and section 9 is a comparison of Cr/Mn, V/Mn and Fe/Mn superlattices. In section 10, results on x-ray magnetic resonant scattering experiments on Ho/Pr alloys are discussed. The conclusion is section 11.

2 X-ray diffraction

In this chapter x-ray diffraction will be discussed. Starting with scattering from a free electron we will consider elastic and inelastic scattering. From here we will move on to scattering from an atom to a group of atoms until we reach the general formula for scattering from a crystal. In section 10, this theory will be supplemented with x-ray magnetic scattering.

Scattering of electromagnetic waves on electrons in the general case is a complicated process, where ultimately both the photons and the electrons must be treated quantum mechanically.[1] Such a treatment is beyond the scope of this work and therefore the focus will be on the application of the theory to scattering from thin films, and superlattices. The main references in this section are James [44] and Warren [90].

2.1 Scattering from a free electron

The scattering of x-rays from a free electron calculated by the classical approximation is given by the Thompson formula:[2]

$$I_e = I_0 \left(\frac{\mu_o e^2}{4\pi m R} \right)^2 (\varepsilon_\perp + \varepsilon_\parallel \cos^2 2\theta) \tag{1}$$

Here $\varepsilon_\perp$ and $\varepsilon_\parallel$ denote the polarization components of the incident x-ray beam with respect to the scattering plane. For example we have for unpolarized radiation, like a rotating anode, $\varepsilon_\perp = \varepsilon_\parallel = 1/2$ in which case the Thompson scattering is:

$$I_e = I_0 \left(\frac{\mu_o e^2}{4\pi m R} \right)^2 \left(\frac{1 + \cos^2 2\theta}{2} \right) \tag{2}$$

For synchrotron radiation, the beam is mainly polarized in the plane of the synchrotron ring [85]. For vertical and horizontal scattering geometries we have:

$$I_{vert} = I_0 \left(\frac{\mu_o e^2}{4\pi m R} \right)^2 \tag{3}$$

$$I_{horiz} = I_0 \left(\frac{\mu_o e^2}{4\pi m R} \right)^2 \cos^2(2\theta) \tag{4}$$

The polarization factors affect the recorded intensity and the experimental data must be corrected for these prior to fitting.

In actual scattering experiments one observes that only part of the scattered radiation has the same wavelength as the incident radiation, whereas a considerable part has longer wavelengths. This is called Compton scattering, and is due to energy transfer from the x-rays to the electron. The shift in wavelength is a function only of the scattering angle θ:

$$\lambda_c = \lambda_0 + \frac{h}{mc}(1 - \cos 2\theta) \tag{5}$$

The Thompson formula can still be used to describe the scattered intensity provided that a small correction factor is applied. Since the incident and scattered waves have different wavelengths there is no phase relation between them,

[1] Often the field is treated classically and the atom quantum mechanically. For a good textbook see [10].

[2] The formula gives the scattered intensity per unit area at the distance R from the electron.

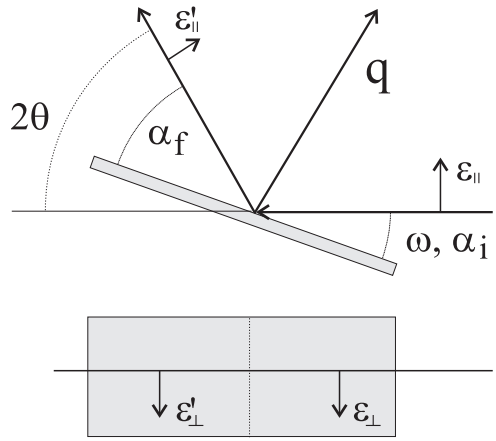

Figure 3. Definition of the incident and exit scattering angles with respect to the substrate. Also shown are the components of the polarization vector parallel to ($\varepsilon_{\parallel}$) and perpendicular ($\varepsilon_{\perp}$) to the scattering plane for the incoming and diffracted beams.

and the scattering is incoherent. Incoherent scattering gives rise to an increased background, which is small in diffraction from crystals.

2.2 Scattering from an atom

If we denote the electronic charge density by $\rho(\bar{r})$, the coherent scattering from an atom is proportional to

$$I \propto f(\bar{q})^2 \tag{6}$$

where the scattering factor

$$f(\bar{q}) = \int \rho(\bar{r}) e^{i\bar{q}\cdot\bar{r}} d\bar{r} \tag{7}$$

is the Fourier transform of the electronic charge density. In the case where the charge is centro-symmetrically distributed f is simply a function of q, with f(0)=Z. In our diffraction experiments the variation of $f(q)$ is so great that we need to take that into account.

The above formula is only correct if the x-ray wavelength is far from wavelengths corresponding to any absorption edges in the atom. If this is not the case we need to make some corrections to the scattering factor, which is now rewritten as

$$f = f_0 + \Delta f' + i\Delta f'' \tag{8}$$

One can find values for the scattering factor and the dispersion in *International tables* [92] or similar works. Very often the scattering factor for an atom is listed as a function of q, ignoring the non centro-symmetric electron distribution. The error introduced in doing so is in our case probably negligible [32].

For calculation purposes one can use a very accurate formula for approximation of the form factor [33],

$$f(q) = \sum_{i=1}^{4} A_i \exp\left(\frac{-B_i q^2}{16\pi^2}\right) + C \tag{9}$$

where, f' and f'' can be calculated from certain program packages. Figure 4 shows the result of such calculations on Fe and V.

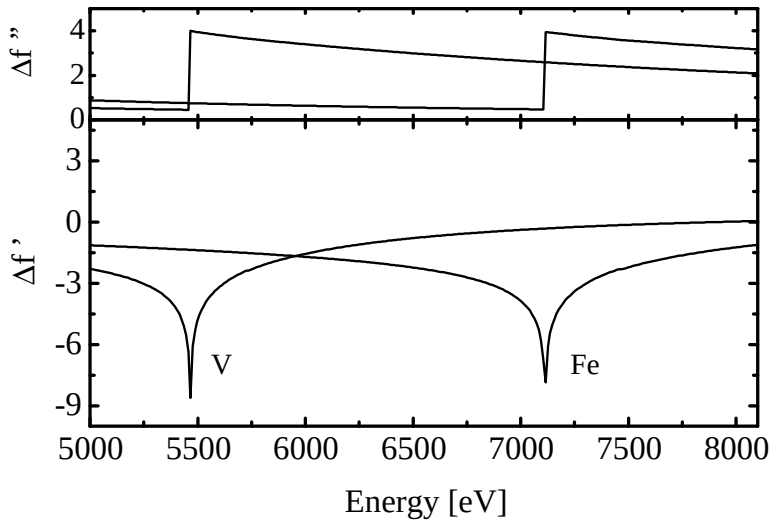

Figure 4. Dispersion curves for Fe and V. Top: Imaginary part (Δf”). Bottom: Real part (Δf’). The Fe K and V K edges are at 7112eV and 5465eV respectively. (Fortran routines courtesy of F.E. Christensen, DRI.)

2.3 Structure factor

For an arbitrary collection of atoms with scattering factors $f_j(q)$ situated at positions $\bar{r}_j$ the structure factor is calculated as

$$F(\bar{q}) = \sum_j f_j(q) e^{i\bar{q}\cdot\bar{r}_j} \tag{10}$$

where $\bar{q}$ is the momentum transfer $\bar{k}_f - \bar{k}_i$.

The structure factor $F(q)$ is very important in determining crystallographic structures from diffraction profiles. Where the structure factor vanishes, so does the scattered intensity and the systematic absence of scattered intensity is the information we need to distinguish between different crystal structures [90].

For the bcc structure, the atoms of the unit cell are placed in $(0,0,0)$ and $(1/2,1/2,1/2)$. The structure factor for the bcc structure, ignoring the atomic form factor $f(q)$, is then $F(h,k,l) = 1 + \mathrm{e}^{i\pi(h+k+l)}$, which is nonvanishing only when $h+k+l$ is even. Some of the low-index reflections are (000), (011), (002), (022) and (013). Figure 6 show the $(h0l)$ reflections in reciprocal space.

2.4 Scattering from an array of atoms

Let us consider the simple case of a one dimensional array of N identical atoms. The atomic positions are then $r_j = ja$ where a is the lattice spacing. The structure factor calculated from equation 10 is then given by

$$F(q) = f(q)\frac{1-\mathrm{e}^{iqaN}}{1-\mathrm{e}^{iqa}} \tag{11}$$

Functions of this type will here be referred to as Laue functions. Equation 11 describes a static lattice. In a real lattice, however, atoms are vibrating around their average positions because of thermal motion. This motion leads to a correction factor called the Debye-Waller factor, and has the form $\exp(-q^2M)$, where M includes the magnitude of the vibrations and a temperature dependence. We can now rewrite the form factor $f(q) = \exp(-q^2M)(f + f' + if'')$ so that it contains

the above mentioned corrections. The scattered intensity from our array of atoms is proportional to the square of the structure factor

$$I(q) \propto f^2(q)\frac{\sin^2(qaN/2)}{\sin^2(qa/2)} \tag{12}$$

Equation 12 is periodic with a period of $2\pi/a$. When $q = 2\pi n/a$ the intensity peaks as $f^2(q)N^2$. The width of the peak (FWHM) is $2\sqrt{6}/Na$. Figure 5 shows the characteristic appearance of the scattered intensity.

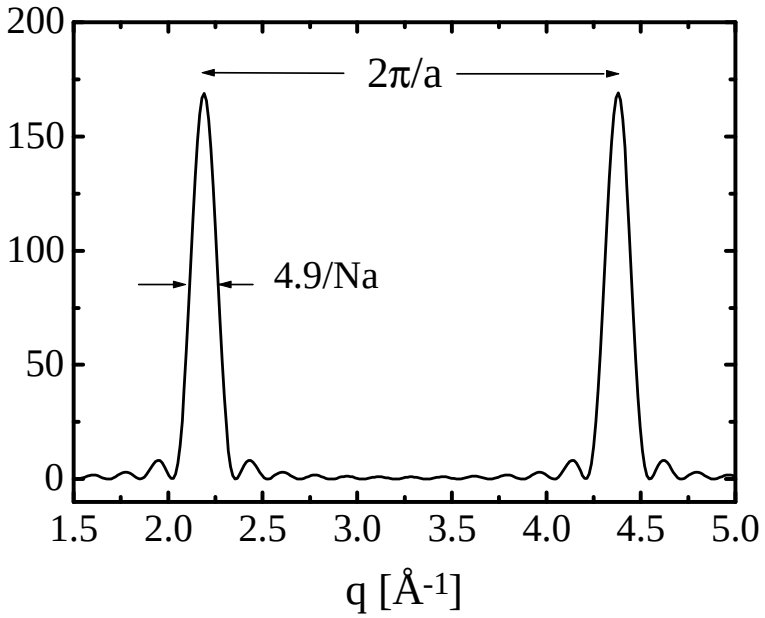

Figure 5. The Laue function squared for $a = 2.87$Å and N=13. The peak intensity is $N^2 = 169$, and the peak width (FWHM) is $4.9/37.3 = 0.13\text{Å}^{-1}$. The distance between the peaks is $2\pi/a = 2.19\text{Å}^{-1}$.

2.5 Diffractometers

Here we will consider how to calculate the position in reciprocal space[3] from a given setting of the diffractometer.

The incoming and outgoing waves in a scattering experiment defines the momentum transfer $\bar{q} = \bar{k}_f - \bar{k}_i$, with $k = 2\pi/\lambda$.

The incoming wave is often fixed and we are then varying our sample position and the detector position. One can choose to consider the incoming and outgoing waves as variable and the sample as fixed, which is mathematically equivalent.

Two-axis diffractometer

The two-axis diffractometer is probably the most common setup because of its simplicity: Two angles completely describe the scattering geometry.

With the definitions of the angles, ω and 2θ, from figure 3 we obtain the following equations for the momentum transfer

$$q_z = k[\sin\omega + \sin(2\theta - \omega)] \tag{13}$$

$$q_x = k[\cos\omega - \cos(2\theta - \omega)] \tag{14}$$

[3]For a mathematical description of reciprocal space see [4].

Without restrictions we can assume that the angles ω and 2θ belong to the interval $[0;\pi]$. If we exclude the positions of the diffractometer, where the momentum transfer implies that we are shooting x-rays through the sample, we are limiting our movements is reciprocal space. The amount of reciprocal space that the x-ray diffractometer at Risø can reach in this geometry is illustrated in figure 6.

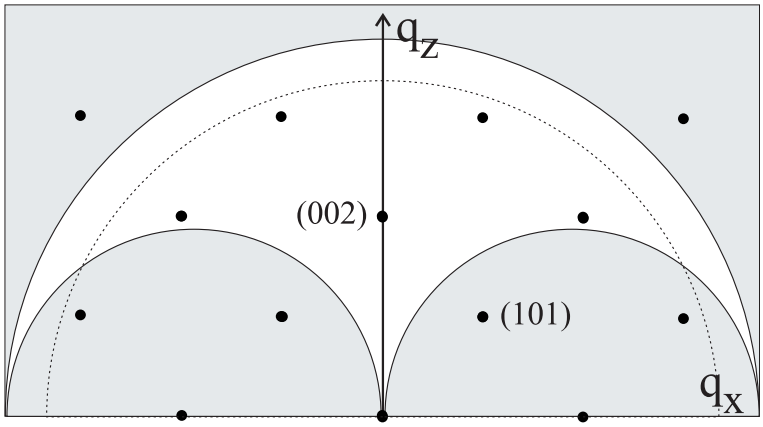

Figure 6. The parts of reciprocal space theoretically within our reach for $\lambda = 1.5406$Å. The half circle with the largest radius is the maximum momentum transfer q =8.157Å^{-1}. The dotted line represents the actual reachable part due to implementation specific limitations on 2θ. Also plotted are the bulk reflections for an Fe crystal.

Even though five reflections from Fe can be theoretically examined this way, the instrumental implementations will restrain us from all but the (002) reflection. Cables, step motors and mountings will prevent 2θ from reaching angles higher than $\approx 115°$. Tracing a curve in the available area, and recording the measured intensity at the points sampled is called a scan. Two frequently used scans should be mentioned here, namely the longitudinal scan or $[00\ell]$ scan and the transverse scan or ω-scan. For the $[00\ell]$ scan, the angle ω is set to $2\theta/2$, reducing equation 13 to: $q_z = 2k\sin\theta$. It is seen that the momentum transfer is parallel to the surface normal. For superlattices this is also the modulation direction, which is why this scan is so important. The other scan is the transverse scan, where 2θ is fixed and ω is varied from ω-δ to ω+δ. In this type of scan q_z is nearly constant while q_x is varying. With these two types of scans we can obtain information about domain sizes in the modulation direction and in the transverse direction.

Surface diffractometers

In order to span a larger part of reciprocal space one can add more degrees of freedom to the diffractometer. This is illustrated in figure 7 where the angles α_i,α_f,ω and 2θ are defined. Note that ω and 2θ are defined differently compared to figure 3. This is similar to the setup at the BW2 beamline in HASYLAB, however at BW2 the two additional angles χ_u and χ_l are cradles used for initial alignment only.

Now the momentum transfer vector q can be written as

$$\bar{q}(\alpha_i,\alpha_f,\omega,2\theta) = k\begin{pmatrix}\cos\alpha_f\cos 2\theta - \cos\alpha_i\cos\omega\\ \cos\alpha_f\sin 2\theta - \cos\alpha_i\sin\omega\\ \sin\alpha_f + \sin\alpha_i\end{pmatrix} \tag{15}$$

We can now reach the (101) reflection, for instance, in infinitely many ways. However, the incident angle α_i is typically fixed, which immediately gives us the

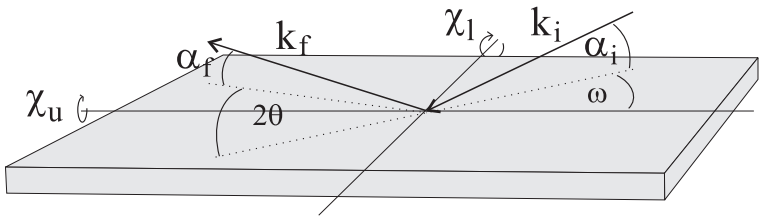

Figure 7. Angle definitions for the surface diffractometer. The two χ circles used for alignment are also shown.

value for the exit angle α_f. This leaves us with two equations which should be solved for the two unknowns 2θ and ω. If $\omega = 2\theta = 0$, we recover the simpler θ-2θ formula from equation 13, with ω substituted by α_i, and $(2\theta - \omega)$ substituted by α_f.

2.6 Data corrections

In order to compare experimental data with simulations we need to correct our data for a number of effects. Generally one can write the observed intensity as

$$I \propto \int_{-\infty}^{\infty} PLA \mid F(q') \mid^2 R(q - q')dq' \tag{16}$$

where P is the polarization described section 2.1, L is the Lorenz factor and A is an area correction that accounts for the illuminated area of the sample. Finally, we need to convolute the theoretical intensity with a resolution function $R(q)$ depending on the spectrometer setup. We often estimate the resolution from the width of the MgO (002) reflection since it is close to the superlattice reflections and is believed to be resolution limited. For more detailed descriptions of these corrections we refer to [25, 90].

3 The MBE system

The Risø MBE system consists of two interconnected vacuum chambers: The MBE chamber shown in figure 8 and the analysis chamber. In the MBE chamber there are two types of evaporators: Effusion cells and electron beam evaporators. The evaporators can hold up to eight elements at a time, where three need to have relatively low melting points since the effusion cells can only reach about 1400°C. The film growth is monitored by RHEED and the deposition is controlled by a system of computerized shutters and a quartz monitor.

The MBE chamber is pumped by a turbo pump with a forepump, an ion pump and a titanium sublimation pump. Liquid nitrogen can be directed through a heat shield inside the chamber in order to produce additional cryo pumping where gases are trapped on the cold shield. The pressure is monitored by ionization gauges when in the UHV region.

The analysis/preparation chamber is a multi purpose chamber equipped with LEED, AES and argon-ion sputtering as well as a quadrupole mass spectrometer. The pumping facilities are the same as for the MBE chamber with the exception of the cryogenic pumping.

Sample transfer between the two chambers is done by translating the sample on a long manipulator arm through a pipeline connecting the two chambers. For both chambers there are electric feedthroughs to accommodate temperature measurements, high voltages, sample heating and UHV illumination.

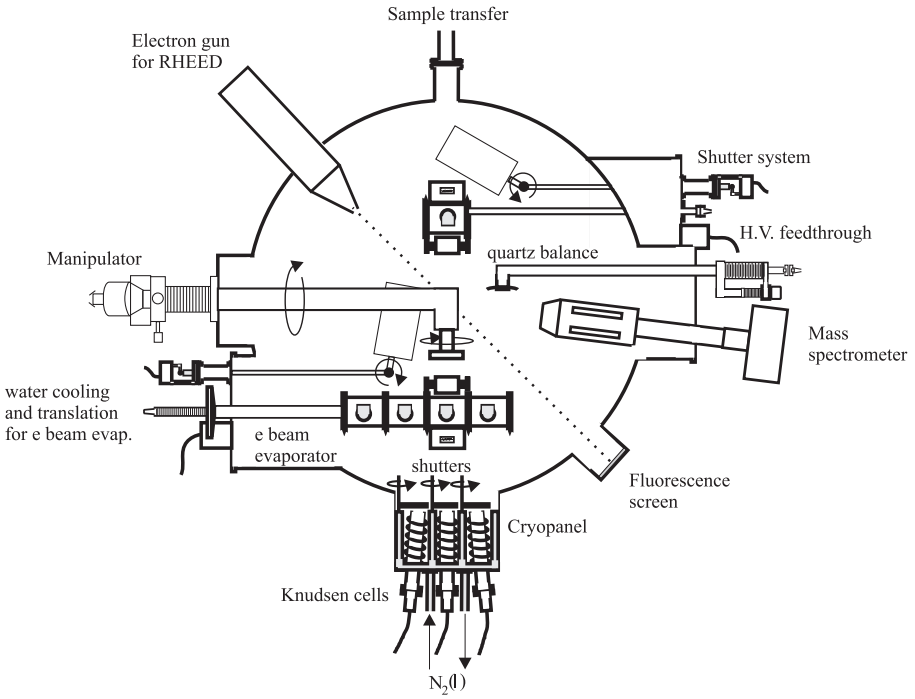

Figure 8. Top view of the MBE chamber at Risø. The RHEED electron gun and the fluorescence screen have been rotated 90° counter clock-wise for clarity (J. G. Larsen).

3.1 In-situ analysis

During deposition we can measure deposition rates, sample temperatures, pressure, residual gases and growth modes. For chemical composition of the surface we have to transfer the sample to the analysis chamber. We will here briefly look into the principles behind the techniques employed.

Electron scattering

For electron energies in the range from a few eV to tens of thousands eV, depending of the angle of incidence, the mean free path of electrons can be as low as a few monolayers. In the same range of energies, the wavelength of the electrons is comparable to the atomic distances in the samples. Several techniques involving elastic as well as inelastic scattering of electrons can be used to give information about electronic structure, chemical composition, surface vibrational states and crystal growth. The two electron scattering techniques used in this work are RHEED and AES and these will be explained briefly. For a detailed account of the capabilities of these techniques the reader is referred to [58] and [94].

RHEED

Reflection High Energy Electron Diffraction is one example of a simple but very useful technique employed in almost every MBE system. In RHEED a beam of monochromatic high energy electrons is directed to the substrate at a low angle of incidence, enabling surface sensitivity. The electrons are accelerated over a voltage V. We can now relate the wavelength of the electrons to their kinetic energy V, by the following equation

$$\lambda = \sqrt{\frac{150.4}{V}} \tag{17}$$

Where λ is given in Å and V in eV. Typical energies are 10keV which gives wavelengths of 0.1226Å, and wavevectors of 51.2Å^{-1}. The Evald sphere will be rather large as illustrated in figure 9. The Bragg rods from the surface will now intersect the Evald sphere over some interval giving rise to streaks on the fluorescence screen. The distance between the streaks, d, is related to the in-plane distance a by $a = \lambda L/d$, where L is the distance from the surface to the screen.

RHEED is an affordable in-situ technique, which can provide information about the growth mode and lattice constants in the surface plane. Combined with a CCD camera and some data acquisition equipment this is a powerful tool. By continuously measuring the streak distances we can monitor in-plane relaxations as a function of layer thickness during deposition. In order to verify the in-plane structure of the surface, one will have to perform RHEED along the relevant crystal axis.

RHEED is also used as an initial indication of the substrate quality, because here the streaks must be sharp to indicate good crystallinity of the surface. It is possible to accurately measure the number of monolayers deposited on a surface by recording the streak intensity. For true layer by layer growth the RHEED intensity should oscillate with minimum intensity at half a monolayer [81]. If the deposited material is poly-crystalline the RHEED pattern is a set of concentric diffraction rings. For a surface covered by 3d islands one will observe a spot-like transmission diffraction pattern.

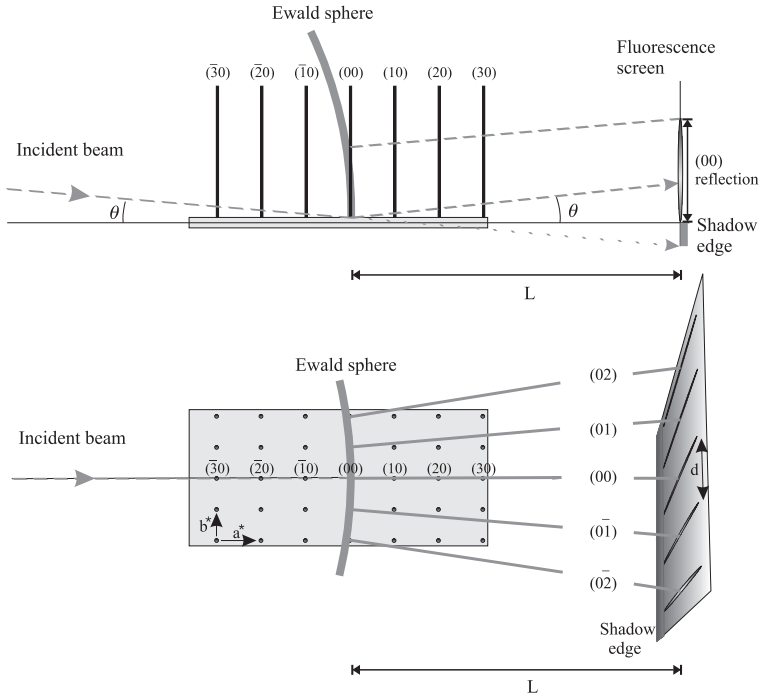

Figure 9. Schematic overview of the RHEED technique (J. G. Larsen).

The Risø MBE equipment does not yet fully support continuous recording of the RHEED patterns.

AES

The principles behind Auger Electron Spectroscopy, AES, is that an incident electron can create an excited state in an atom, which in turn is filled by a higher lying electron. The surplus energy is then used to emit another electron. The final state is doubly ionized. Figure 10 illustrates the Auger $KL_1L_{2,3}$ process. The energy of the emitted electron is

$$E = E_K - E_{L_1} - E_{L_{2,3}} - U \tag{18}$$

where E_K, etc., are one-electron binding energies and U includes corrections from the local electronic environment, screening and hole-hole interaction energies. Clearly, the energy of the emitted electron is a fingerprint of the element probed by the electron.

AES spectra from pure elements and compounds are tabulated, and the measured spectrum can be directly compared to these for identification. The measured Auger spectrum is normally displayed after differentiation in order to suppress the large background of secondary electrons. AES can also, with some care, give quantitative information about coverages [19]. For less accurate estimates one can simply use the peak to peak value for two elements as an indication of the relative concentrations. In this work we have used the peak to peak values as estimates of the coverages.

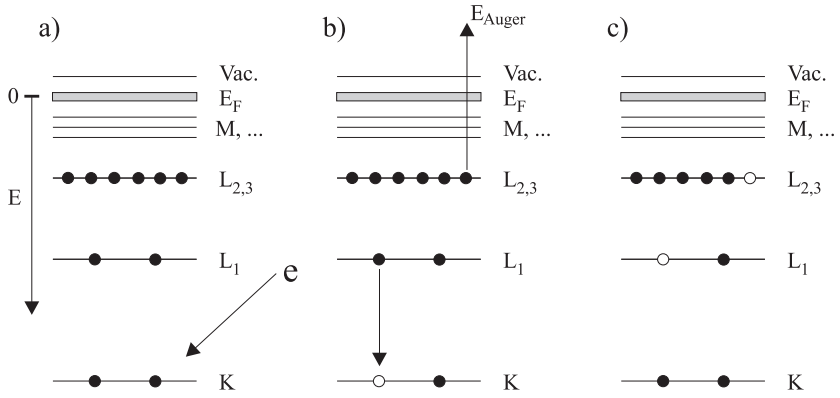

Figure 10. The Auger process: a) Ground state of the atom and the incoming electron. b) Excited state produced by the incident electron, and indication of the electronic rearrangement. c) Doubly ionized state (J. G. Larsen).

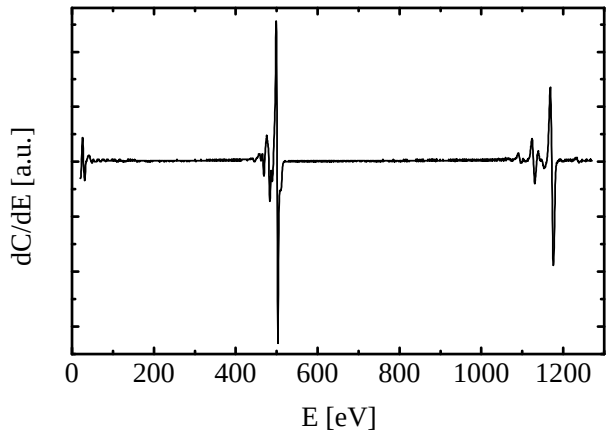

Figure 11. AES spectrum on MgO(001) surface after deposition of 200Å MgO. The peaks at 500eV arise from oxygen atoms, the ones at 1200 eV from magnesium.

Pressure

Several methods of pressure measurement exist and must be employed in order to monitor the pressure from atmospheric pressure to UHV. However when operating in the UHV regime from 10^{-8}-10^{-11} torr only ionization gauges are needed. The operating principle of the ionization gauges is that electrons emitted from a hot filament are accelerated in an electric field. The electrons will undergo collisions with gas molecules in the system. If the kinetic energy of the electrons are sufficiently high the collisions will result in creation of positive ions of the gas molecules. These ions are collected at a thin wire which will produce a current proportional to the pressure. Modern ionization gauges are also called Bayard-Alpert gauges.

The ionization gauges cannot be used at too high pressures since the filament will become permanently damaged. In the region from atmospheric pressure to 10^{-5} torr one can however measure the thermal conductivity of the gas, which is a function of pressure. The first gauges using this method were made by Pirani and they are also called Pirani gauges. The Pirani gauges in our MBE equipment are reliable in the 1000 torr - 10^{-3} torr range.

The MBE chamber has a base pressure of 6×10^{-11}torr. This pressure is made up from mainly H_2 and CO. However leaks in the system, which are not at all uncommon, will result in water vapor and N_2. In order to investigate the 'health'

of the vacuum system, and to measure partial pressures of the residual gases, mass spectrometers are used. The quadrupole mass spectrometer is based on the trajectories of ions in an electric field produced by applying a potential to four metal rods. These rods are subjected to a combination of DC and AC voltages, which results in complicated trajectories of the ions. A further analysis is out of the scope of this work, but the mass selectivity comes out as narrow stable regions in a (V_{dc},V_{ac}) plot. The quadrupole mass spectrometer is essential when leaks need to be detected. Helium gas is sprayed on parts of the UHV chamber and the spectrometer is set to measure the partial pressure of helium. When leak finding, the equipment often provides an audible signal with a frequency somewhat proportional to the pressure.

Deposition

The principle behind measuring the amount of deposited material is quite simple:

A quartz crystal with with a thickness t_x and density ρ_x will oscillate with an eigen frequency f_x when a voltage is applied. If a thin film with density ρ_f is deposited on the crystal the mass of the oscillating system will increase which leads to a new oscillation frequency f.

The equation governing this frequency shift is derived from acoustic theory [65, 64] and is related to the thickness of the deposited film t_f by:

$$t_f = \frac{t_x f_x \rho_x}{\pi f \rho_f} \tan^{-1}\left(Z \tan\left[\frac{\pi(f_x - f)}{f_x}\right]\right) \tag{19}$$

where μ is the shear modulus and Z is the acoustic impedance ratio given by

$$Z = \sqrt{\frac{\rho_x \mu_x}{\rho_f \mu_f}} \tag{20}$$

Typical eigenfrequencies of the quartz crystals are 6.050×10^6Hz, and as long as the frequency shift is below 15% the film thickness obtained by equation 19 is accurate to within 1% in our equipment [52]. When the frequency shift becomes too large the crystal must be replaced.

The accuracy of equation 19 is dependent on the accuracy of the densities and shear moduli of the deposited materials. These values are generally taken from tables of bulk properties. Thin films rarely have bulk properties and this is often a source of systematic deviations between the thickness derived from the quartz monitor and the x-ray or neutron diffraction profiles. For example we have grown identical superlattices with nominal thicknesses of 39Å. The obtained thicknesses, measured by x-ray diffraction, were 40.13Å and 39.87Å respectively. This is a deviation of about 3% from the nominal thickness, but only a relative deviation of 0.6%. There is one other source of systematic errors that should be mentioned here. When the shutters are opened to expose the red-hot evaporant, a heat wave will hit the quartz crystal which will produce frequency shifts leading to negative deposition values. It is not uncommon that the reading goes down one or two angstroms in the beginning of a deposition. This will result in films which are thicker than the nominal values. The effect also means that statistical fluctuations in the bi-layer thickness will occur. Compensation for the heat shock can be made by introducing an extra shutter in front of the sample. Prior to deposition the shutter in front of the evaporators is opened and after a few seconds the crystal will give stable readings. Now the shutter in front of the sample can be opened so deposition can proceed.

Sample temperature

Sample temperatures can be measured in two different ways. The most simple is a thermocouple of W/Re[4] wire which is touching the back of the sample mount. The resistance of the wire reflects the temperature, which can be read in a LCD display. Temperatures in the interval from 0°C - 2000°C can be measured this way. If for some reason the thermocouple is not in direct contact with the sample mount the measured temperature will be lower than the true sample temperature. For comparison we have also measured the sample temperature with an infra red thermometer at temperatures above 600°C and there is a discrepancy of up to 50°C between the two readings. This discrepancy is probably due to missing calibration of the infra red thermometer. Therefore, the referenced temperatures are based on the thermocouple.

3.2 Sample mount

Construction of heat resistant, flexible and UHV compatible sample mounts and manipulators is a task of endless repetition of trial and error. Samples are no good if the only way to mount them is to expose the UHV system to atmospheric pressure. Therefore movable parts must be invented to allow the sample to be inserted, heated, deposited on, subjected to RHEED , AES or sputtering etc. and finally to be extracted from the UHV system. The choice of material used as sample mount, ball bearings or springs is by no means trivial. On the one hand, the material should be one that can stand temperatures of say 1000°C, and on the other hand it should be easily tooled. Favorite choices of materials are tungsten and tantalum.

In our MBE system the sample is resting on a molybdenum cap and fixed by two tungsten springs, which are tightened by tantalum screws. Behind the cap there is a filament of tungsten for heating of the cap and sample. A voltage difference can be applied between the filament and cap so electrons emitted can be accelerated and be used as an additional means of heating the sample. Sample temperatures of 1000°C can easily be achieved this way. Figure 12 shows the sample mount.

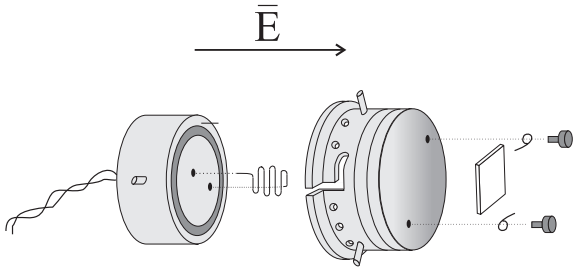

Figure 12. Exploded view of the sample mount. The sample is mounted on the cap which can be inserted on the manipulator arm. Sample heating is done by applying a current to the filament. There is also a thermocouple on the manipulator arm, which touches the back side of the cap when mounted.

3.3 Evaporators

In order to produce the molecular beams necessary for the film production we employ two techniques: Electron beam evaporators and Knudsen cells.

[4]Actually a 74%W-26%Re/95%W5%Re wire.

Electron beam evaporators

In electron beam evaporators the adsorbant is placed in an open crucible and is heated by a beam of electrons which are produced by a filament. The electrons are accelerated by an electric field and directed to the adsorbant by a magnetic field. The heating is very efficient and large deposition rates can be achieved this way. The deposition rates can be controlled by adjusting the current of the electron beam. In this work the values of the current were between 20mA and 150mA. The electron beam is hitting the adsorbant in a tiny spot. In order to produce a more uniform heating of the adsorbant an AC field can be applied causing the electron beam to sweep over the surface thus heating a larger area. The molecular beam produced by electron beam evaporation is divergent and generally no calibration is required.

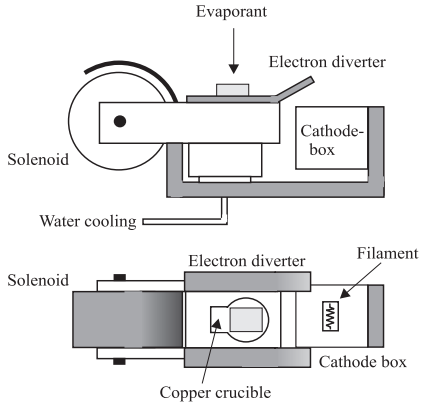

Figure 13. The electron beam evaporator (J. G. Larsen).

Knudsen cells

In the Knudsen cells[5] the evaporant is placed in a ceramic crucible[6] which is surrounded by a filament. In our equipment with currents up to 14A, the cells can reach temperatures up to 1400°C. The beam divergence in very small and deposition is dependent on the positions of the Knudsen cells relative to the sample. Therefore the deposition yield must initially be calibrated for each cell.

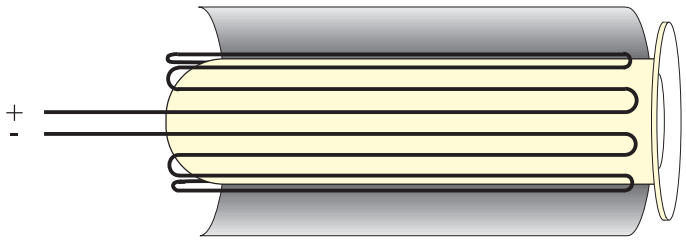

Figure 14. Knudsen cell. The heating element and the heat shield, here shown only in part, are made of tantalum. The evaporant is placed in the bottom of the crucible.

[5] After the Danish physicist Martin Knudsen, who contributed to the understanding of molecular flow at low pressures.

[6] In our case BN. Rare earth superlattices will react chemically with BN so a tantalum shield must be used.

4 Film growth and epitaxy

Here we will give a cursory introduction to thin film studies and crystal growth. The study of growth modes are part of this thesis only so far as we are content that the thin films grow properly on the substrates used. But it has not been subject of intense studies here. However, as a subject it is of course immensely important as it is the basis upon which thin film studies rely. The information in the introductory sections (4.1 and 4.2) are heavily borrowed from [62] and [51], and references given by name and year, refer to these volumes. After this we will move on to a description of the structure and preparation of the samples that we have used in our work. Finally, some experimental results of thin film growth performed as part of this thesis will be mentioned.

4.1 Development in thin film studies

The growth and structural characterization of thin films have been studied since the beginning of the century, and are still subjects of intense research. The field of thin film studies has evolved through a continuous development of experimental methods and technological landmarks, and many of the earliest studied systems have been continuously taken up for studies. One example is the study of silver on rock salt (Ag/NaCl). Initial studies of Ag/NaCl were done in 1934, but new results on the growth of Ag on NaCl were published as recent as 1996 [76] - 62 years later!

The first systems studied were of alkali halides on alkali halides, grown in solutions and investigated by optical microscopy. At that time, in 1906, it was concluded that epitaxy was more likely to occur if the misfit between the two alkali halides were small. However neither epitaxy nor misfit as concepts were invented at the time. The discovery of x-ray diffraction in 1912 soon provided more crystallographic insight in for example crystal orientation. A large study by Royer in 1928 led to a more specific definition of misfit as $100(b-a)/a$, where a and b are the lattice spacings of the substrate and the overgrowth, respectively. Royer concluded that the two components should have similar crystal structure and a small misfit. Royer also coined the word epitaxy in the meaning "arrangement on".

Further progress in the surface and thin film studies were made with the discovery of electron diffraction in 1927. Due to the difficulty in obtaining a good vacuum, high energy electron diffraction (HEED) was the only practical technique at that time. Studies of zinc oxide on zinc by Finch and Quarrell (1933,1934) lead to the conclusion that the initial growth layer was strained in such a way that the misfit was zero. This zero misfit was called "pseudomorphism", and led to the theoretical model of layer by layer growth, by van der Merwe in 1949. RHEED data on other systems suggested that the initial growth also could have the form of isolated 3d nuclei, which was confirmed by TEM investigations in the 1950s.

The advent of UHV techniques made feasible the low energy electron diffraction technique (LEED) which is suitable for sub-monolayer overgrowth investigations. The better vacuum led to more well controlled experimental conditions, as the residual gases were reduced. In 1967, the electron scattering techniques were augmented by means of chemical analysis by measuring the energy of the emitted Auger electrons.

From around 1975 the standard thin film production and analysis vacuum chambers were fully developed [62], and little new functionality has been added since.

Exceptions are in-situ x-ray diffraction [25] section 4, scanning tunneling microscopy (STM) and atomic force microscopy [11], though these techniques are rarely implemented in today's MBE systems.

The choice of materials for investigation has been made partly for technological reasons and partly because of trends in physics. Up to the 50s the investigated systems were often alkali halides, metals and metal oxides on alkali halides. In the 60s and 70s the new and promising semiconductor devices led to intense semiconductor investigations. In the 80s and up to today much focus has been on magnetic interactions in rare earth and transition metals, where new tools, such as synchrotron radiation have provided new means for thin film investigations.

4.2 Growth

From earlier studies of thin films it is found that the process of film growth is a complex process involving arrival of atoms at the surface, adsorption of atoms, diffusion/mobility across the surface, nucleation and coalescence. It was also found that there are four parameters that influence the film growth: pressure, deposition rate, substrate temperature and substrate structure. Also the binding energy of the adsorbant to the substrate is of vital importance but since this is not a controllable parameter we will ignore it here.

For metals adsorbed on insulator surfaces we assume that every atom that impinges on the surface stays there. For other systems one may operate with a sticking coefficient, which is the probability of an atom sticking to the surface upon impingement.

The adsorbed atoms can exhibit a complicated dynamical behavior at the surface: Atoms can move around on the surface, they can diffuse into the substrate or even desorb from the substrate. When two atoms meet formation of metastable nuclei can occur. This is referred to as nucleation. Nuclei can also split up, rotate or migrate across the surface. At a certain critical size the nuclei become stable, and this is where actual crystal growth begins.

Initial film growth is categorized in three different types of behaviors. The three growth modes are called Volmer-Weber (VW), Stranski-Krastonov (SK) and Frank-van der Merwe growths (FM). Figure 15 illustrates the different growth modes, which can be described as follows. For VW growth the growth is occurring as 3d nuclei which later coalesce. SK growth is characterized as the formation of one or more layers upon which nucleation and growth dominate. Each growth mode has a characteristic RHEED signal, and can thus be verified [72]. FM growth or layer-by-layer growth is the growth mode that have our interest because of the well ordered surfaces produced this way.

Figure 15. Illustration of the three different growth modes: Left: FM growth. Center: SK growth. Right: VW growth.

In order to achieve layer-by-layer growth of atoms instead of 3d growth one must try to reduce the nucleation rate. This can be done by 1) reducing the pressure since it is believed that residual gases can create nucleation sites on the substrate

surface, 2) increasing the substrate temperature which promotes the mobility of the atoms on the surface, or 3) reduce the deposition rate. RHEED can be used to verify the growth mode because oscillations of the intensity indicate that layer-by-layer growth is occurring.

For metallic superlattices we cannot just crank up the temperature in order to improve the crystal growth. With increasing temperature, interdiffusion between the two metals becomes significant and causes a degradation or even loss of interfacial order. The competition between bulk- and surface diffusion has been subject to theoretical speculation which has led to a suggested growth temperature T_g of 3/8'th of the melting temperature of the metals [26]. For metals with a large difference in melting temperature and different crystal structures such as Au/Cr [48] there is no applicable theory concerning optimal growth conditions.

A final aspect of importance to growth is the substrate. The crystallographic structure of the substrate should in some sense be similar to the adsorbant in order to facilitate oriented crystal growth. Since we cannot expect to grow smooth thin films on a rough surface, efforts must be made to produce the finest surfaces possible. The procedures for cleaning substrate surfaces are highly material dependent, but usually involves sputtering and annealing as the final steps.

Despite years of theoretical and experimental work, the process of MBE growth and formation of layered structures is still far from well understood. This means that from a crystal-growers point of view there is still not a solid theoretical alternative to trial and error.

4.3 Thin film production

Various methods for thin film production exist: Laser ablation, sputtering techniques, chemical vapor deposition (CVD), electro deposition and molecular beam evaporation (MBE) to name the most common. One of the most promising in terms of production of well defined thin films, with a low density of impurities is MBE.

MBE is simply the heating of the adsorbant in UHV until the adsorbant evaporates at a suitable rate, thus producing a beam of atoms or molecules. In the UHV region all gases and molecules can be assumed to travel in straight lines until they hit the chamber walls or the sample. By carefully controlling the heating of the adsorbant, the flow can be well controlled. Deposition rates of 0.2Å/s and less can be easily achieved. The MBE process is unlikely to be used in industrial processes with large specimens because of the relatively small area covered by the molecular beam and the cost involved with scaling the technique. However, MBE has been used to produce high quality thin films, alloys and superlattices suitable to physics experiments thus making it a much used technique.

The main obstacle when working with MBE is the good vacuum we need. In order to avoid impurities in the film originating from the residual gases in the chamber, a base pressure in the chamber around 10^{-10} torr is needed. The impact rate, R, of a gas of molecules of molar mass M, temperature T in K, and a pressure of P torr is given by:

$$R = 3.51 \times 10^{22} \frac{P}{(MT)^{1/2}} \tag{21}$$

Giving an impact rate of $\approx 4{\times}10^{13}$ molecules/$(cm^2 s)$ for a gas of nitrogen at 300K at a pressure of 10^{-7} torr. If we assume that a surface has a density of the order of 10^{15} atoms/cm^2 and that a molecule sticks to the surface when it

impinges on it, we will get a full coverage of 'impurities' in roughly 30 seconds. When growing thin films with MBE, the typical growth rates are 1.0 Å/s or less, so it is clear that in order to produce high quality films with a low amount of impurities we need pressures in the 10^{-8}-10^{-10} torr range. This is why ultra high vacuum is needed[7]. We will not consider the details about molecular flow, but mention that even though the flow is molecular it need not be homogeneous. Sample rotation can be employed in order to ensure very homogeneous films, and without it the samples may develop thickness gradients during growth.

4.4 Sample preparation

Two types of substrates have been used in the MBE work at Risø: Al_2O_3 (sapphire) and MgO substrates. MgO (001) substrates[8] were mostly used but also (111) surfaces have been used. The sapphire substrates[9] were $(11\bar{2}0)$ surfaces. The MgO crystal structure can be described as two interpenetrating fcc lattices each with a lattice parameter of 4.211Å [95]. Sapphire can be described as oxygen atoms in a slightly distorted hexagonal lattice, with aluminum atoms located along the c axis. The lattice parameters are $a = 4.763$Å and $c = 13.003$Å [95]. Figure 16 shows the atomic arrangement of sapphire.

The reflections in reciprocal space, $\tau_{hkl} = 2\pi/d_{hkl}$, from cubic and hexagonal lattices can be found by the following formulae [90]:

$$1/d_{hkl}^2 = \frac{h^2+k^2+l^2}{a^2} \qquad (cubic) \tag{22}$$

$$1/d_{hkl}^2 = \frac{4}{3}\frac{h^2+hk+k^2}{a^2} + \frac{l^2}{c^2} \qquad (hexagonal) \tag{23}$$

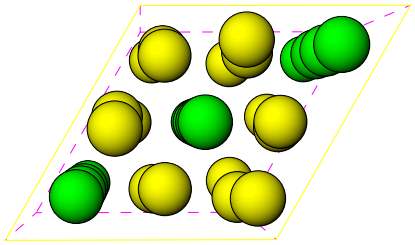

Figure 16. The sapphire structure viewed along the c axis.

MgO substrates

Initially the MgO substrates were subjected to a cycle of chemical baths. First the sample was given an ultrasonic massage in methanol for 15 min. Then in distilled water and ultrasonic treatment for 5 min. Finally in ultra pure water for a few minutes. After this treatment all water should easily slide off the surface when subjected to a light, filtered airflow. The cycle was repeated if necessary. The preparation was done in an air filtered room. The procedure was simply adopted as a standard of practice. However, it turned out that the ultra clean water was actually alive with bacteria for a long time without us being aware of

[7] See [91] for detailed information about vacuum techniques.
[8] From Kelpin Kristallhandel.
[9] From L&K.

that. Furthermore, the sample was exposed to dusty air during transport from the clean room to the MBE laboratory. Therefore we began to look for a new preparation method.

A new turn in the sample treatment came about after our attention had been brought to investigations on ceramic surfaces [3, 37]. Here it was suggested that by heating the substrates in air to high temperatures, one could promote faceting on the surface.

In the hope that the heat promoted faceting would produce a smoother surface with the desired orientation, we heated MgO samples to 1600°C for 12 hours. The following analysis of the surface quality and composition by AES, AFM and x-ray reflectometry has provided evidence that this treatment does have a positive effect [48]. The positive effect is, however, partly canceled by the fact that we may have been using too high temperatures and that MgO could be evaporating from the surface [69]. Figure 17 shows AFM pictures of MgO(001) and MgO(111) surfaces after the heat treatment. It is seen that in both cases a terrassed structure is present at the surface. For untreated MgO surfaces no such structure is observed. The untreated surfaces appear bubbly and cloudy with no sharp features.

After the heat treatment the samples were immersed in methanol in an ultrasonic bath for a few minutes, and then introduced into the UHV system. Here the samples were annealed at 600°C for 5 minutes. RHEED pictures of the substrates showed sharp streaks which indicates a well ordered surface lattice, and Kikuchi lines arising from inelastic scattering in the surface region signifying a fine crystallinity of the substrates [2].

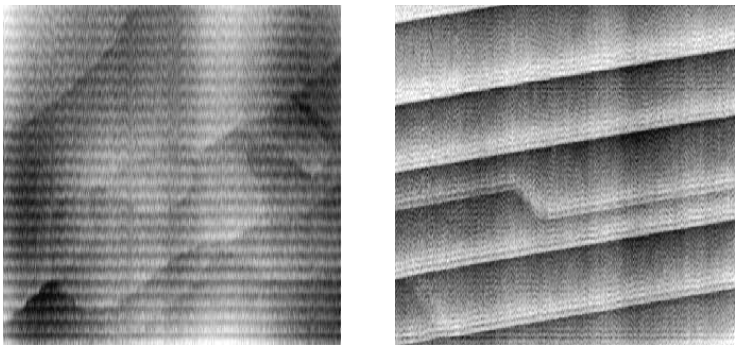

Figure 17. AFM of MgO substrates after heat treatment. Left: MgO(100). Area: 3μm×3μm, height 37Å. Right: MgO(111). Area: 1μm×1μm, height 151Å. The smallest streaky features in the figures are artifacts from the AFM scanning.

Sapphire substrates

The heat treatment of the sapphire substrates[10] proved to be more impressive. Figure 18 show AFM pictures of the same sapphire substrate before and after the heat treatment. It is clear to see that the surface is more well ordered after the treatment. In both pictures the maximum height difference is about 160Å. For the heat treated surface we clearly count at least eight terraces each being on average 23Å high. Within the resolution of the AFM we must conclude that these terraces appear to be atomically flat over a distance larger than 1μm. The positive effect

[10] Identical to the treatment of MgO.

of the heat treatment was confirmed by reflectometry and diffuse x-ray scattering experiments, where the surface roughness is demonstrated to decrease significantly [48].

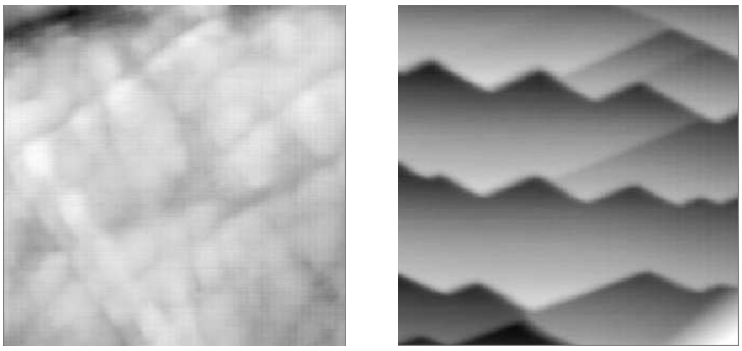

Figure 18. AFM picture of sapphire $(11\bar{2}0)$ substrate. Left: prior to heat treatment. Right: after heat treatment. The area scanned are in both cases 1μm$\times 1\mu$m. For both pictures the height difference is about 160Å (J. G. Larsen).

The further treatment of the sapphire substrates is identical to the procedure for the MgO substrates.

Other substrates

Ge(001) substrates have been used for growth of M/Mn superlattices (M=Fe, V, Cr), on which several measurements have been made. Ge has the diamond structure which consists of two fcc lattices offset by $(a/4, a/4, a/4)$, with $a = 5.657$Å. The first germanium reflection in the $[00\ell]$ direction is the (004) reflection at 4.442Å^{-1}.

4.5 Growth of a Nb thin film

As an example of the production of a thin film of high structural quality in an UHV environment we will mention the growth of Nb thin films on sapphire substrates. Niobium grown on sapphire is often used as a buffer for growing rare-earth thin films and superlattices [28] and is known to give very well aligned films [75]. We have grown Nb films on sapphire in an effort to produce a good substrate for Ce thin films. Nb has a rather high melting temperature of 2741K and it is therefore expected that the sample temperature during growth should exceed the 600°C that is possible with the ohmic heating alone. It was therefore necessary to apply a voltage between the filament and the sample mount and then adjust the current to produce additional heating. The substrate was heated to 1000°C for 5 minutes by applying 300V and 200mA. During deposition the temperature was 800°C (110V,120mA). At this temperature RHEED showed very thin and fine streaks during growth. A RHEED picture was taken during growth and is shown in figure 19. The total deposition took 16 minutes. After deposition the quartz monitor showed 278Å, which corresponds to a deposition rate of ≈0.3Å/s.

Figure 20 shows a specular scan of a Nb film grown on sapphire taken at beamline BW2 at HASYLAB. The setup used a Ge (111) analyzer crystal and the resolution in the $[00\ell]$ direction is estimated from the width (FWHM) of the sapphire $(11\bar{2}0)$ reflection to be 0.0008Å^{-1}. The resolution of the transverse scans are

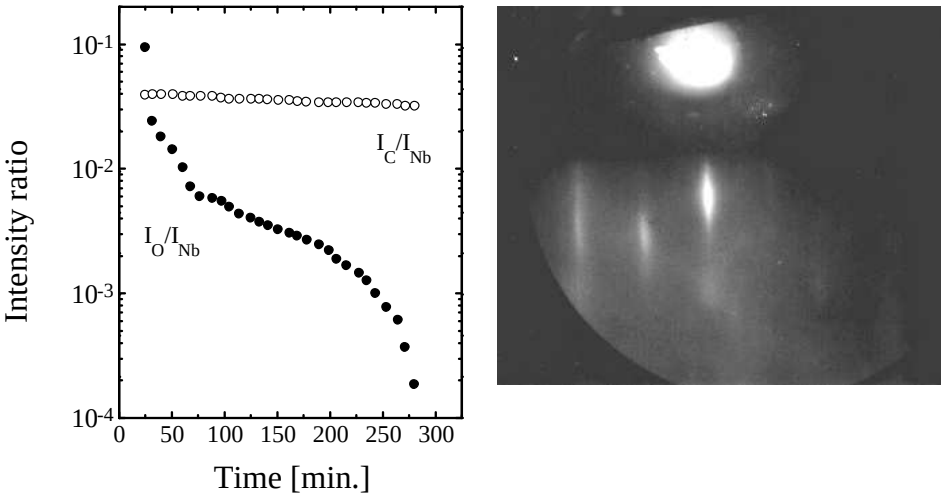

Figure 19. Left: AES peak ratios as function of sputtering time. (•) oxygen to niobium ratio, (○) carbon to niobium ratio. Right: RHEED of the Nb thin film during growth. A wrong setting of aperture and exposure time, combined with the light emitted from the 800°C sample mount, has caused the streaks to look much less sharp than observed in the laboratory.

estimated to be 0.032°. The scan shows two peaks: The one at $q = 2.636\text{Å}^{-1}$ is originating from the sapphire $(11\bar{2}0)$ reflection and the peak at $q = 2.703\text{Å}^{-1}$ is the Nb (110) reflection. The nominal thickness of the Nb film is 278Å. The structural parameters obtained from modeling the niobium peak with a simple Laue-function squared reveal that the lattice parameter $d = 2.324$Å and a total film thickness of 249Å. This means that the quartz monitor must have been mis-calibrated. The width of the central Nb peak is 0.0242Å^{-1} corresponding to a coherence length of 260Å. This means that we can consider our thin film to be a single crystal in the growth direction. The FWHM of the transverse scan on the Nb peak was 0.085° giving a coherence length of ≈2500Å in the plane. We therefore conclude that the Nb film is of a high crystalline quality, and must be considered an excellent buffer for further film growth.

After the growth of the film AES revealed that oxygen and carbon were present on the surface. Since the substrates were meant for Ce thin film growth, and Ce is very reactive with oxygen, it was investigated by repeated sputtering and AES measurements, whether these impurities could be removed. An example of the result of a cycle of sputtering and AES analysis is shown in figure 19. The sputtering voltage was 600 eV and the current was between 3 and 5μA. The curves are obtained by measuring the peak to peak heights of the AES signals and then take the ratio of these signals. As mentioned in section 3.1 this ratio is proportional to the relative concentrations. As is clearly seen from the figure oxygen is readily removed by sputtering, whereas the sputtering does not affect the carbon coverage noticeably. This could mean that carbon is strongly bonded to the surface, or that carbon is present in our Nb film. It is not clear where that carbon originates from, but one suggestion is that the niobium metal contains carbon and another is that the carbon are residues from the methanol cleaning process. In this case one can conclude that the oxygen can be removed from the surface.

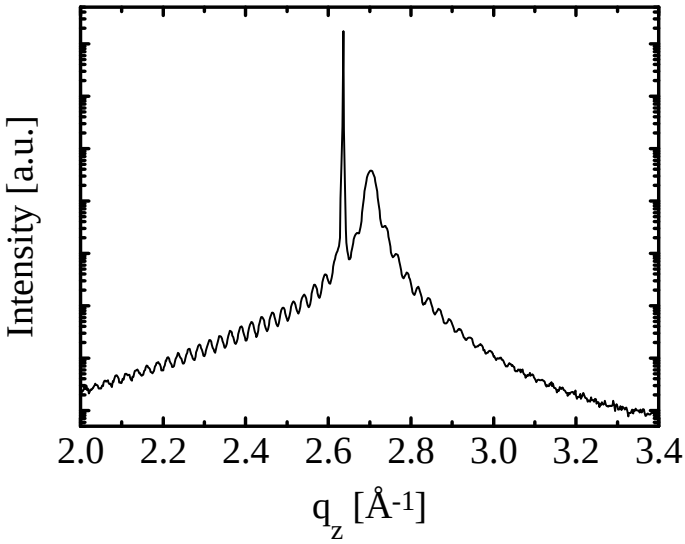

Figure 20. x-ray diffraction profile for the Nb thin film. The Nb (220) reflection occurs at 2.703Å^{-1}. The sharp peak at $2.636\text{Å}^{-1}$is the sapphire $(11\bar{2}0)$ reflection.

5 Diffraction from superlattices

We will first consider diffraction from the perfect or ideal superlattice, then we shall move on to consider more realistic models. We will mainly consider the special case of diffraction where the momentum transfer is parallel to the modulation direction. However, non-specular scans will be briefly commented.

Since 1980 there has been a continuous development of superlattice diffraction models. Mostly, these models have been used to describe diffraction from a specific superlattice system. One paper stands out in the sense that it presents the accumulated knowledge at the time of writing[11] and describes a general framework for modeling many structural properties [27].

5.1 Diffraction from perfect superlattices

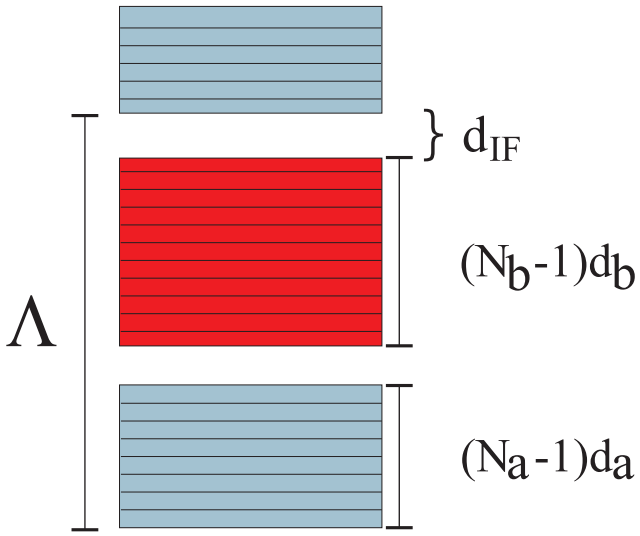

Figure 21. Definition of the parameters used to characterize a superlattice. For each constituent of the superlattice N_x is the number of scattering planes and d_x is the lattice parameter. The interface distance between the two materials is denoted d_{IF} and Λ is the modulation period.

Using the general formula 2.3 for scattering from a crystal, we obtain the following expression for scattering from two layers A and B with complex atomic formfactors $\tilde{f}_A$ and $\tilde{f}_B$, structure factors $F_A(q)$ and $F_B(q)$ with a phase factor ϕ whose form depend on the offset of the scattering planes.

$$F(q) = \tilde{f}_A F_A(q) + e^{i\phi}\tilde{f}_B F_B(q) \tag{24}$$

For the intensity we then take the absolute square of the total structure factor, noting that the squares in the formula are absolute squares.

$$I(q) \propto \tilde{f}_A^2 F_A^2(q) + \tilde{f}_B^2 F_B^2(q) + 2Re\{\tilde{f}_A F_A(q)\tilde{f}_B^* F_B^*(q)e^{-i\phi}\} \tag{25}$$

We now make the assumption that the atomic form factors are real, ignoring the imaginary part of the correction f''. By doing so we neglect small interference terms in the third part of the above sum. With this assumption we can simplify equation 25 further. Our perfect superlattice can now be described with only five

[11] From [77],[78],[66], [53],[54] and references therein.

parameters: The lattice constants and the number of atomic planes for each of the layers, and the number of repeats (bi-layers).

$$F(q) = \sum_{j=0}^{Nbl-1} e^{iq\Lambda j} \left(\sum_{k=0}^{Na-1} f_a(q) e^{iqak} + e^{i\phi q} \sum_{l=0}^{Nb-1} f_b(q) e^{iqbl} \right) \tag{26}$$

Here $\Lambda = (Na-1)a + (Nb-1)b + 2d_{IF}$ is the modulation length and ϕ is the distance from the bottom of layer a to the bottom of layer b: $\phi = (Na-1)a + d_{IF}$.

In this simple case we can find an explicit expression for the diffracted intensity:

$$\begin{aligned} I(q) \propto \mid F(q) \mid^2 &= \frac{\sin^2(q\Lambda N_{BL}/2)}{\sin^2(q\Lambda/2)} \left(f_a^2 \frac{\sin^2(qaN_a/2)}{\sin^2(qa/2)} + f_b^2 \frac{\sin^2(qbN_b/2)}{\sin^2(qb/2)} \right. \\ &+ \left. 2\cos(q\Lambda/2) f_a f_b \frac{\sin(qaN_a/2)}{\sin(qa/2)} \frac{\sin(qbN_b/2)}{\sin(qb/2)} \right) \end{aligned} \tag{27}$$

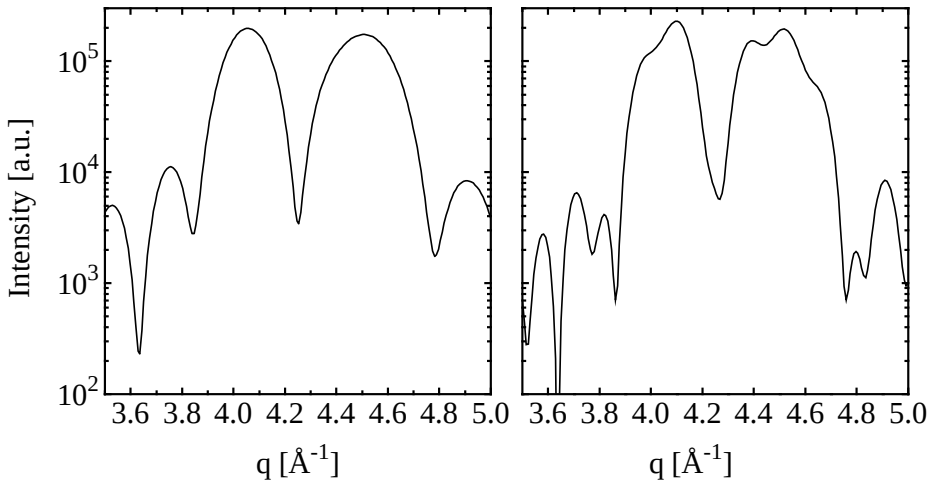

Figure 22. Demonstration of the effect of interference where two Laue functions overlap. Left: Sum of two Laue functions. Right: With the interference term. The structural parameters used for the simulation are d_A=1.395Å, n_A=16, d_B=1.55Å and n_B=19.

Figure 22 shows the diffracted intensity from a bi-layer of 20Å Fe and 30Å V calculated from equation 27. In the left profile we see the scattering from two independent layers. Here the intensities from each layer are simply added. However, if we include the interference term we see that the profiles develop wiggles where the two contributions overlap. If we include the influence of repeated bi-layers this profile will be further modulated by oscillations with a period of $2\pi/\Lambda$. This is shown in figures 23 and 24. The structural parameters are the same as for figure 22 with four and ten bi-layers respectively. The effect of increasing the number of bi-layers is to narrow the peak widths, and to raise the intensities. At a low number of bi-layers such as in figure 23, we see additional peaks between the main superlattice peaks. This is due to the properties of the Laue function described in section 2.4. These peaks are suppressed as the number of bi-layers increase. In figure 24 they are barely resolved.

5.2 Imperfect superlattices

The ideal superlattice described in section 5.1 suffers from the fact that real superlattices are not perfect. In general, the measured widths of the superlattice peaks are much broader than predicted from the ideal superlattice model. Deviations

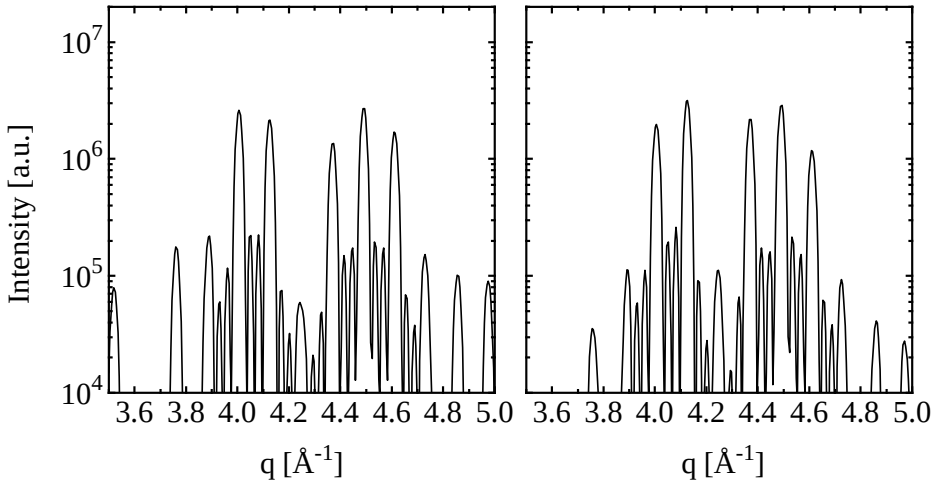

Figure 23. Superlattice diffraction profile calculated from formula 27. Left: without the interference term. Right: including the interference term. The number of bi-layers is arbitrarily chosen to be four.

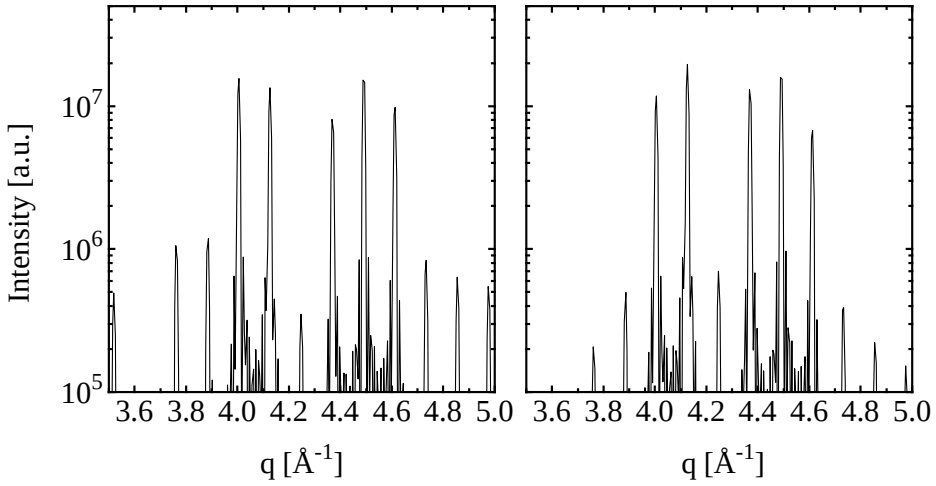

Figure 24. As the previous figure, but here the number of bi-layers is 10. The superlattice peaks become narrower, and the intensity increases.

from the perfect lattice arise from thermal oscillation of the atoms, misfit dislocations, intermixing at the interfaces, internal strain and from fluctuations from the deposition process. We must here distinguish between two types of disorder: cumulative and noncumulative.

For noncumulative disorder in a layer, the atomic positions can be written as $r_n = n\bar{d} + \delta d_n$, where $\bar{d}$ is the average lattice constant and δ_n is the deviation. If the fluctuation is Gaussian distributed, this will give rise to a Debye-Waller-like factor.

For cumulative disorder, however, the atomic position of one layer has an influence on the position of all following atoms, so

$$r_n = n\bar{d} + \sum_{i=1}^{n} \delta_i \tag{28}$$

The effect of cumulative disorder will not only affect the intensity but also the width of the diffraction peaks [27]. Cumulative disorder can be continuous, where the lattice parameter for example, is allowed to fluctuate around a nominal value,

or it can be discrete, such as the variation of the number of scattering planes from one layer to another. Because thin films and superlattices are grown layer by layer, cumulative disorder is most important.

Noninteger number of scattering planes

So far, we have treated the number of scattering planes in each layer as integers. For real superlattices grown on substrates with areas in the range of cm^2, this is never the case. We can easily grow, say, 3.6 monolayers of a material. An illustration of a thin film with, on average, a non-integer number of scattering planes, is shown in figure 25. If we have a well controlled MBE environment we can, however, expect the amount of deposited material to have an average value $\bar{N}$ with a standard deviation, or fluctuation width, of σ_N. Now $\bar{N}$ is noninteger and this will modify the formula for the structure factor.

We assume that the fluctuation of N is Gaussian so that the probability for having N scattering planes is

$$P(N) = \frac{1}{K} \exp\left[\frac{(N-\bar{N})^2}{-2\sigma^2}\right] \tag{29}$$

where K is normalized so that $\sum_{N=1}^{\infty} P(N) = 1$ [54]. Now we calculate an effective structure factor for a layer by averaging over all possible values of N. By doing this, the structure factor can be written

$$F(q) = \sum_{N=1}^{\infty} F(q,N)P(N) \tag{30}$$

For practical purposes the sum can limited to N values from $\bar{N}-3\sigma_N$ to $\bar{N}+3\sigma_N$.

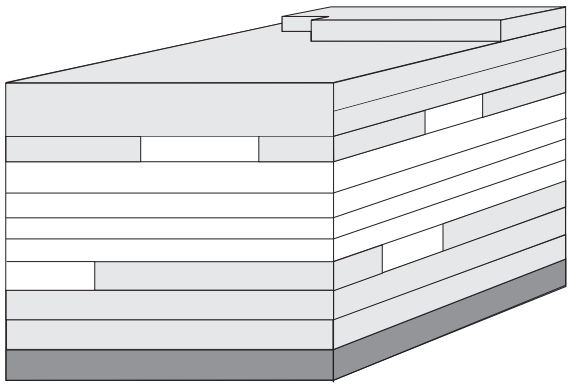

Figure 25. A more realistic superlattice model: The interfaces are still sharp but on average there is a noninteger number of scattering planes of the two materials.

Epitaxial strain

It is often the case that the grown thin films do not have bulk lattice parameters. If we assume that thin films, which are compressed with respect to their bulk values, can relax the lattice near the interfaces, this can be modelled as

$$d_j = d + \Delta e^{-\alpha j} \tag{31}$$

where d_j is the lattice parameter of the j'th layer, Δ is the relaxation, and d is the superlattice 'bulk' lattice parameter. Figure 26 illustrates the lattice expansion or

reduction near the interfaces. When modeling relaxations near the interfaces like the above mentioned, one generally have to calculate the average lattice parameters of the layers. For thick layers the deviation from the parameter d_X is often small, but especially for very thin layers one has to be particularly careful. If the layer contains less than 8 scattering planes, the intra layer distance d_X is never reached. In that case d_X must be considered a parameter used for generating the distortions only. In order to reduce the number of parameters, we have chosen to fix $\alpha = 0.55$ as suggested by the authors.

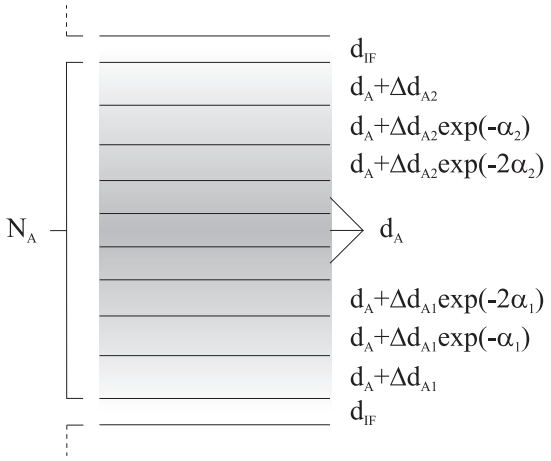

Figure 26. Illustration of the lattice parameters relaxation or compression near the interfaces (J. Pohl).

Interdiffusion

We have so far assumed that the chemical modulation of the superlattices was ideal, leading to sharp interfaces separating material A from B. Depending on the growth conditions and the miscibility of the constituents of the superlattices, a large intermixing may in fact occur. Detailed knowledge about the structural properties of superlattice interfaces is scarce, and it is difficult to distinguish between alloying, intermixing and interdiffusion in the interface regions. Nevertheless, if we assume that intermixing occurs over a region of N planes this could be modelled by employing an effective form factor for the 'alloy' in that region. If we denote the concentration of material A in layer j of the intermixing region as c_j the form factor is then modified as

$$f_j(q) = c_j f_A(q) + \{1 - c_j\} f_B(q), \qquad c_i \in [0; 1] \tag{32}$$

This could then be combined with a separate lattice parameter for the intermixing layer. With this approach, the basic superstructure is no longer a bi-layer, but a 'quad-layer'. A method similar to this has been successfully used to simulate alloying at the interfaces of InP/InAlAs superlattices [12].

The simulation software

The effects of introducing fluctuations in the superlattice models are reducing the intensity, increasing the background, broadening the diffraction peaks and suppressing the Laue oscillations. All the described imperfections can be modelled

by using a program called SUPREX[12] We have primarily used a PC version of SUPREX for the simulations. This version does not include interdiffusion modeling. The program is free and distributable. However, the authors require the following articles referenced: Schuller 1980 [77], Sevehans et al. 1986 [78] and Fullerton et al. 1992 [27].

5.3 Nonspecular diffraction

When performing scans in reciprocal space where the momentum transfer is not along the modulation direction but in, say, the $[10\ell]$ direction, the interpretation of the diffraction profile is more complicated. The structure factor is now written as

$$F(\bar{q}) = F_{\parallel}(q_x, q_y)F_{\perp}(q_z) + G_{\parallel}(q_x, q_y)G_{\perp}(q_z) \tag{33}$$

where F and G are the structure factors for material A and B respectively. The structure factors are divided into components parallel with and perpendicular to the surface plane.

$$F_{\parallel}(q_x, q_y) = \sum_{j,k} \mathrm{e}^{iq_x aj}\mathrm{e}^{iq_y bk} \tag{34}$$

$$F_{\perp}(q_z) = \sum_{l} \mathrm{e}^{iq_z cl} \tag{35}$$

It is clear that when we are scanning by varying l, whether in an $[00\ell]$ or $[10\ell]$ direction, h and k are constant. Therefore, the scan is still only sensitive to structural variation along the modulation direction. However, the relative positions of the peaks from the individual layers are different in the two types of scan. As seen from figure 27 the two (011) reflections are closer to each other than the (002) reflections, leading to more symmetric superlattice modulations.

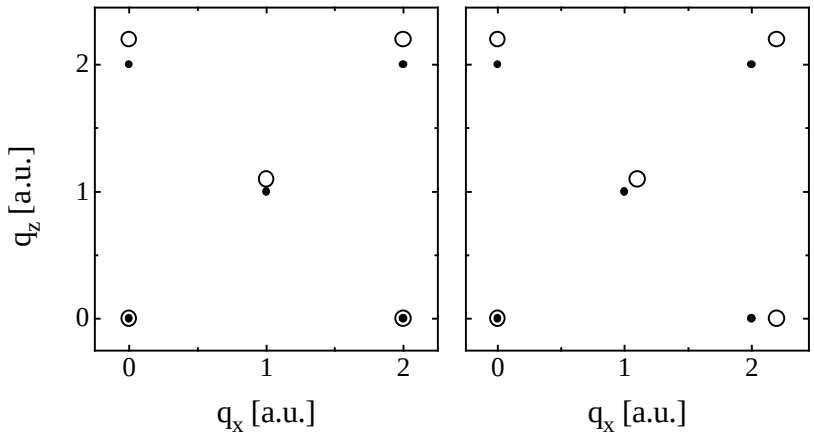

Figure 27. Diffraction pattern in the (h0l) plane. Left: Two materials with commensurate in-plane lattice constants. Right: Two independent lattices. Note the difference between the (101) and the (002) reflections.

[12]SUPerlattice REfinement from X-ray diffraction

5.4 Neutron diffraction

Concerning the structural properties of solids, the structure factor for neutrons is calculated in a similar way as for x-rays.

$$F(\bar{q}) = \sum_i b_i \mathrm{e}^{i\bar{q}\bar{r}_i} \tag{36}$$

Here, b_i is the scattering length. The form factors for x-rays increase with the number of electrons, whereas the scattering length is varying from one isotope to another. Moreover, light x-ray scatterers, like H, Be etc. can easily scatter neutrons. Furthermore, the neutron possesses a magnetic moment and thus interacts with magnetic moments through the magnetic dipole interaction. In addition, due to the low absorption of neutrons, we are free to choose a scattering geometry, in which we are shooting through the substrate. This is in contrast to x-rays which are easily absorbed by, for example, 1mm Ge. This makes it possible to measure in-plane lattice parameters without changing the spectrometer setup much. Moreover, since neutrons are sensitive to magnetic moments perpendicular to the momentum transfer, detailed knowledge about these can be found by changing the scattering geometry. Figure 28 shows two useful scattering geometries for thin film and superlattice studies.

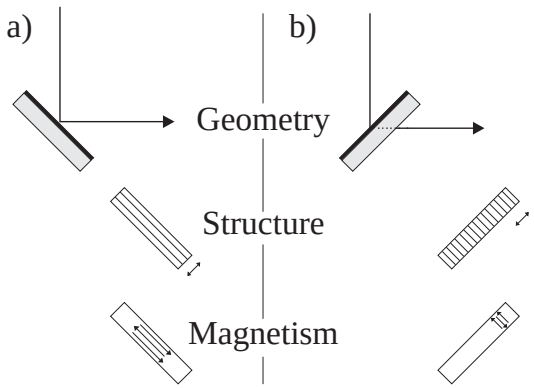

Figure 28. Neutron scattering geometries. Left: Standard [00ℓ] scan probing structural properties along the [00ℓ] direction and magnetic moments in the [hk0] direction. Right: [h00] (or [k00]) scan sensitive to structure in the [h00] direction and magnetism in the [00ℓ] direction.

6 Experiments

In the following four sections, we present experimental results from five MBE grown thin film systems: Fe/V, Cr/Mn, Fe/Mn and V/Mn superlattices and Ho/Pr alloys. The Fe/V superlattices were grown at Risø, the other superlattice systems were grown at the University of Konstanz, while the Ho/Pr alloys were grown at the physics department at Oxford University. The results are partly based on the following four papers:

- Christensen M J, Feidenhans'l R and Nielsen M 1995 *Vacuum* **46** 1113
- Pohl J, Christensen M J, Huljic D, Köhler J, Malang E U, Albrecht M and Bucher E 1997 *J. Appl. Phys.* **81** 169
- Christensen M J, Pohl J, Larsen J G, Köhler J, Feidenhans'l R and Bucher E 1997 *Submitted for publication.*
- Vigliante A, Christensen M J, Hill J P, Helgesen G, Sørensen S Aa, McMorrow D F, Doon Gibbs, Ward R C C and Wells M R 1997 *In preparation*

Measurements on these systems were performed on various diffractometers, which will be mentioned briefly here.

6.1 BW2

The beam at BW2 is produced from a multipole wiggler and is monochromatized by a pair of Si(111) crystals. A toroidal mirror after the monochromator is used to focus the beam. The diffractometer normally operates in the vertical plane, eliminating the need for polarization corrections when scanning in that plane. However the diffractometer can be converted to a 6 circle diffractometer with an arm operating perpendicular to the vertical plane providing for other types of scans in reciprocal space. The resolution of the spectrometer is defined by the divergence of the beam and by 1mm slits over a distance of 800mm. If resolution is crucial the spectrometer can be equipped with an analyzer setup for improved resolution. The spectrometer control program is TASCOM[13]. The beam is attenuated by inserting plates of aluminum in the beam. The plated are located on a motorized attenuation wheel. The detector is a NaI scintillator, and the monitor consist of two capacitor plates with a high voltage across giving rise to a small current when the air molecules are ionized by the x-radiation. For further information about BW2 we refer to reference [20].

6.2 Rotating anode

The x-ray diffractometer setup at Risø is illustrated in figure 29. Although nominally a 12kW rotating copper anode, it was rarely operated at more than 5kW (50kV and 100mA). The setup is very flexible and individual setups can be easily tailored. We mostly used the diffractometer in the θ-2θ mode, although a four circle setup has also been used. The resolution of the diffractometer was defined by four slits located on either side of the Ge(111) monochromator, after the sample and in front of the detector. Evacuated flight tubes were employed in order to reduce air scattering and subsequent loss of intensity.

[13] Triple Axis Spectrometer COMmands, developed at Risø.

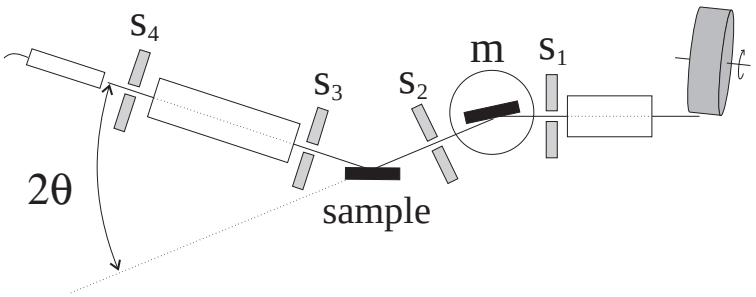

Figure 29. Top view of the standard setup at the rotating copper anode. m: the monochromator within a radiation shield, S_i: slits. The evacuated flight tubes are also shown.

6.3 X22C

X22C at NSLS in Brookhaven is a bending magnet beamline. The beamline is equipped with a doubly focusing nickel-coated mirror and a fixed exit Ge(111) double crystal monochromator. The spectrometer operates in the vertical scattering geometry, similar to BW2. The software controlling the spectrometer is called SPEC. The spectrometer slits defining the incoming beam are motorized and a polarization device can be mounted on the 2θ arm. In order not to destroy the NaI detector when measuring Bragg peaks, aluminum foils are inserted in front of the detector.

6.4 TAS1

The triple axis spectrometer TAS1 is located at the Danish research reactor DR3 at Risø. Although the spectrometer can adjust both energy and momentum transfer, it was setup for elastic scattering only. The resolution of the spectrometer is controlled by cadmium collimators and an analyzer crystal of pyrolytic graphite, and is $\approx 0.035\text{Å}^{-1}$ as estimated from the substrate bulk reflections in these investigations. The neutron beam will, even when monochromatized to the wavelength λ, also contain contributions with $\lambda/2$ and $\lambda/3$ components. These contributions will give rise to additional peaks in the spectrum, but can be filtered out with a cooled Be filter. For technical data on TAS1 please refer to reference [49].

6.5 Fitting

As mentioned in section 5.2, we have used SUPREX to fit the superlattice diffraction profiles. However, we use the term fit in a loose manner along with terms as simulation and modeling. For superlattices of compositions similar to ours, where the thickness and the form factors of the two layers are nearly equal, the calculated structure factor has large interference terms where the Laue functions overlap. Since we are investigating fairly thin layers, the Laue functions are broad and the overlap is large. This means that the parameters used to describe the superlattice couples in a strongly nonlinear way. This makes automated fitting a difficult task so, despite the advanced nonlinear fitting routine, we often found the parameters to converge to the wrong values. Therefore, we refer to 'fit' as adjusting the parameters by hand.

7 Fe/V superlattices

Fe/V superlattices have been investigated by various groups since 1984 and the Fe/V system is still an area of active research. Most work has been concerned with the electronic structure and magnetic properties. Work on Fe/V superlattices in the 80s includes band structure calculations [34], investigations of the superconducting properties [93], magnetic properties [41] and structural properties [22]. In the 90s, new interest in Fe/V superlattices arose from reports on antiferromagnetic [87] and oscillatory [70] exchange coupling. Studies of interdiffusion and alloy formation were also done [80]. Still, magnetism is studied in greatest detail by x-ray magnetic circular dichroism [36, 83], band structure calculations with intermixing at the interfaces [16] and decoupling of superconducting V by thin Fe layers [47]. Dedicated studies of structural, electronic and magnetic properties of Fe/V superlattices and thin films can be found in a collection of papers [42]. Two main results from this collection are evidence of giant magnetoresistance in Fe/V superlattices [31] and reversible tuning of the exchange coupling using hydrogen [40].

Early superlattices were grown at relatively low temperatures on mylar, glass and sapphire substrates, of which only the last could produce epitaxial superlattices. However, details of early structural investigations are scarce. A couple of later studies used Si(001) substrates and one reported the superlattices to be polycrystalline with (100) textures when grown by MBE and (110) textures obtained from sputtering. Later yet, Fe/V superlattices were grown on MgO(001) substrates at higher temperatures which have produced superlattices with an ordered lattice in-plane as well as along the modulation direction [15] and [63]. These superlattices may well be the first Fe/V superlattices qualifying to their name.

In the following section, we report on results of structural investigations of MBE grown Fe/V superlattices on MgO(001) substrates. To our knowledge, no reports have been made so far on this combination.

7.1 Experimental details

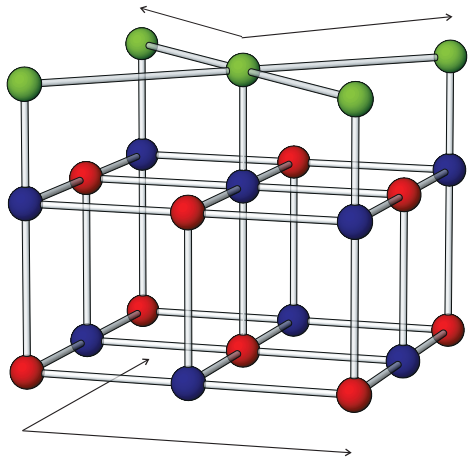

Figure 30. Crystallographic orientation of the SL relative to the MgO substrate. The in-plane axis of the SL is rotated 45°with respect to the substrate. The arrows indicate the directions of the (100) and (010) crystal axis. The SL atoms are are here placed on a top site of the crystal, but this has not been investigated.

Figure 30 show the orientation of the superlattice with respect to the MgO substrate in real space. The superlattices are denoted $[Fe_xV_y]_z$, where x and y are the thicknesses in Å of the Fe and V layers, and z is the number of bi-layers. All superlattices in this investigation have 20 repeats, so the z subscript is omitted. The earliest of our superlattices were grown on a 200Å V seed layer. This layer was later omitted since the superlattices were found to grow just as well on the MgO(001) substrates directly. The superlattices are terminated by a 25Å Au cap layer to limit the oxidation.

The x-ray scattering was performed at beamline BW2 and the rotating anode at Risø. The neutron scattering experiments were performed at the Danish research reactor DR3. The crystallographic orientation of the superlattices with respect to the MgO(001) substrate in reciprocal space is seen in figure 31 together with the different types of scans performed. The shaded squares represent the substrate $(hk0)$ and $(hk2)$ planes, and the dots represent the superlattice reflections. Since $\sqrt{2}a_{SL} \approx a_{MgO}$ the superlattice can be fitted on the substrate if the unit cell of the superlattice is rotated 45° with respect to the substrate as can be seen in figure 30. The lattice parameters at room temperature are $a_{Fe} = 2.867$Å, $a_V = 3.024$Å and $a_{MgO} = 4.211$Å [95]. The lattice mismatch with respect to the MgO lattice is 3.7% for Fe and 1.6% for V.

Sample alignment was done on MgO {002} reflections. References to scanning directions are relative to the orientation of the Fe/V reciprocal lattice unless otherwise stated. Scans along $[00\ell]$ are denoted θ-2θ scans. For scans along $[10\ell]$ we establish the crystallographic orientation of the superlattice with respect to the substrate, and transverse scans at a $(11z)$ reflection are called $[h1z]$ scans, denoting that z is kept fixed and h is varied. This type of scan will give information about domain sizes in the (hk) plane. For a more detailed discussion about non specular scans see [25]. The resolution of the spectrometers was estimated by the widths (FWHM) of the MgO (002) and (111) reflections. The x-ray data is fitted with the model explained in section 5.2. For the high angle neutron scattering we use a very simple model with only five parameters: d_A, n_A, d_B, n_B and d_{IF}. Where d_X is the lattice parameter of material X, n_X is the number of scattering planes which is an integer. d_{IF} is the distance between the top of layer A and the bottom of layer B.

7.2 High angle diffraction

In figure 32 we show a θ-2θ scan for the $[Fe_{20}V_{30}]$ superlattice. The upper part of the figure shows the x-ray diffraction profile taken at $\lambda = 1.417$Å with the fit indicated. The lower part shows neutron data taken at a wavelength of 2.015Å. The characteristic superlattice modulation can easily be seen. The central part of the spectrum has a dip in intensity, separating two broad envelopes. These envelopes originate from scattering from the Fe and V layers respectively. The dip itself is caused by a large separation of the Laue functions from Fe and V. The neutron data look completely different. There are three main peaks in the neutron diffraction profile: The peaks at q=3.97Å^{-1} and q=4.47Å^{-1} are due to a MgO (008) reflection by $\lambda/3$ and a MgO (006) reflection by $\lambda/2$, only the peak at q=4.39Å^{-1} comes from the superlattice. In addition, we can just see some tiny superlattice modulations around the main superlattice reflection. The fit to the neutron data is obtained from a much simpler model than the x-ray fit. The data from the fits are shown in table 1.

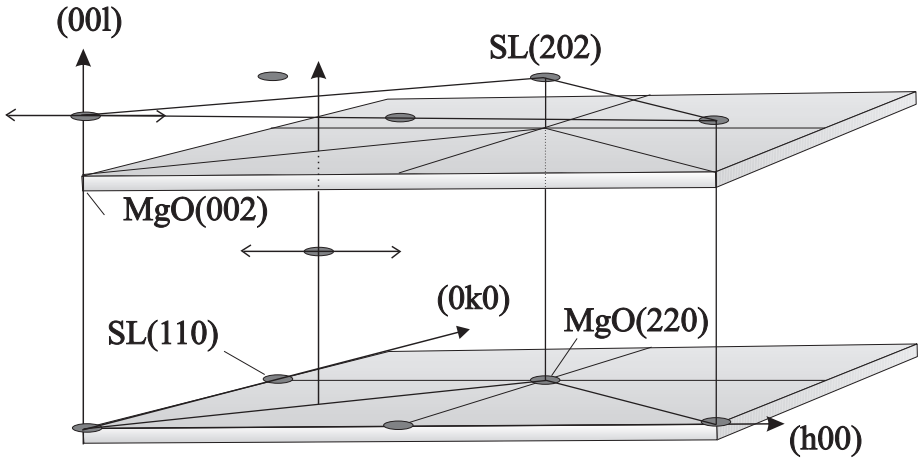

Figure 31. The crystallographic orientation of the superlattices with respect to the substrate viewed in reciprocal space. The grey planes indicate the substrate (hk0) and (hk2) planes. Half of the superlattice fcc reciprocal lattice is shown as thin lines. Black dots are superlattice reflections. An [00ℓ] scan is coinciding with the [00ℓ] axis. The [10ℓ] scan is parallel with the [00ℓ] axis and goes through the (101) reflection. The smaller double arrows indicate transverse scans.

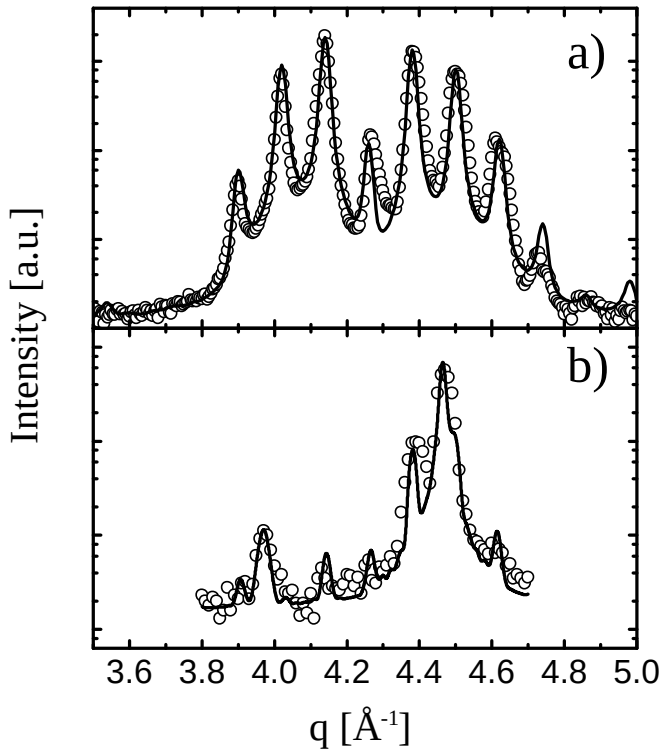

Figure 32. θ-2θ scans on [$Fe_{20}V_{30}$]. a) x-ray data (○) and fit (–) b) Neutron data (○) and fit (–).

The comparison is a good example of the numerical difference between the form factors and the scattering lengths. If we define $\eta_x = f_{Fe}^2/f_V^2$ and $\eta_n = b_{Fe}^2/b_V^2$ we can compare the 'contrasts' of the diffraction profiles. Using the data from table 1, we see that η_n is of the order 600 times larger than η_x in this case. The structural parameters obtained from the analysis show that the lattice parameter of Fe is compressed 2.45% with respect to the bulk value. For scattering planes near the interface the lattice parameters are expanding up to 0.04Å. Assuming

		x-ray		neutron	
		Fe	V	Fe	V
a(q=0)		26	23	0.95	-0.038
d	[Å]	1.395	1.550	1.410	1.550
n	[ML]	16.45	18.99	18	17
σ_n	[ML]	0.50	0.50	-	-
δ_1	[Å]	0.042	-0.103	-	-
δ_2	[Å]	0.038	-0.099	-	-
d_{IF}	[Å]	1.53		1.44	
Λ	[Å]	52.3		51.7	

Table 1. Structural parameters obtained from the fits of the $[Fe_{20}V_{30}]$ superlattice. For the neutron fit the obtained values for d_V and n_V are arbitrary in the sense that because of the low scattering amplitude, the major influence of the V layer is to produce a spacing to affect the total bi-layer length. Other values might produce the same fit. The parameters are: the form factor for x-rays and the scattering lengths for neutrons ($10^{-12}m$), the lattice constant d, the number of scattering planes n with the fluctuation σ_n. The interface relaxations δ and the interface distance d_{IF}.

that Fe is stretched in the surface plane in order to match the MgO lattice, the opposite behavior, relaxation, is expected in the perpendicular direction due to Poissons law. For V the opposite behavior is seen. V is expanded 2.65% compared to the bulk value, but contracts as much as 0.1Å at the Fe-V interface. In this case, the lattice distortions near the interfaces were identical for the Fe-V and V-Fe interfaces. Furthermore, we see that the obtained thickness of the bi-layer is about 5% larger than the nominal thickness which is believed to be due to calibration of the quartz monitor as mentioned in section 3.1.

7.3 Reflectivity

For small angle scattering, the diffraction profile is governed by the optical principles. x-rays are reflected and refracted at the interfaces between different materials, with transmission and reflection amplitudes given by the Fresnel equations. We will not go into detail here, since our experiments have not focused on reflectivity. For references see [9] and [44]. In figure 33 we show another comparison between x-rays and neutrons for the same sample. Here we have a reflectivity scan from q=0.05Å^{-1} to q= 0.55Å^{-1}. The x-ray data show that the superlattice modulations are almost buried in a large background. This background, and also the broad peak at 0.38Å^{-1}, are due to the 25Å Au cap layer which has a scattering power comparable to the bi-layer. For the neutron data the influence of the Au cap layer is not so dominant and we are left with a more 'clean' diffraction profile. The comparison also indicates the trade off in using neutron scattering, namely that the intensity is often lower and the data points are less dense.

7.4 Non-specular scans

In order to establish the crystallographic orientation of the superlattice with respect to the substrate, non-specular scans must be performed. Figure 34 shows a $[10\ell]$ scan on the $[Fe_{20}V_{30}]$ superlattice. The figure has three distinct features: a symmetric superlattice diffraction pattern, one broad peak from the Au cap at 1.6 Å^{-1} and a narrow peak at 1.48 Å^{-1} which is the weak MgO (111) reflection. The scan confirms the picture of the superlattice unit cell being rotated 45° with

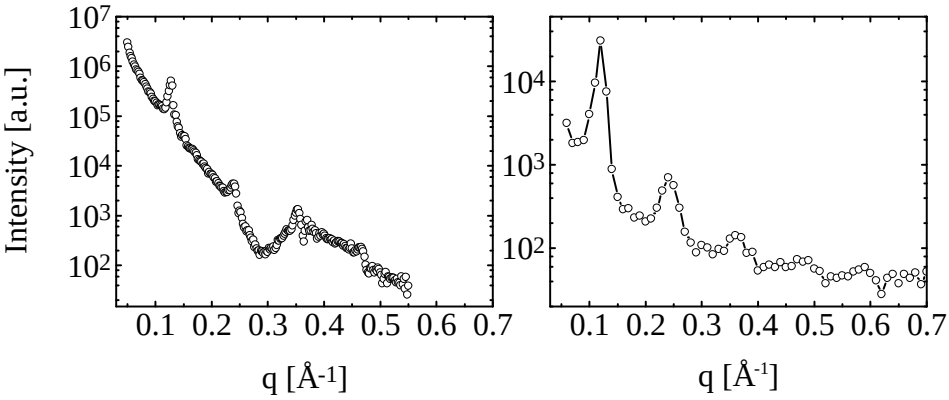

Figure 33. Reflectivity scan on [$Fe_{20}V_{30}$]. Left: x-ray data (○). Right: neutron data.

respect to the substrate.

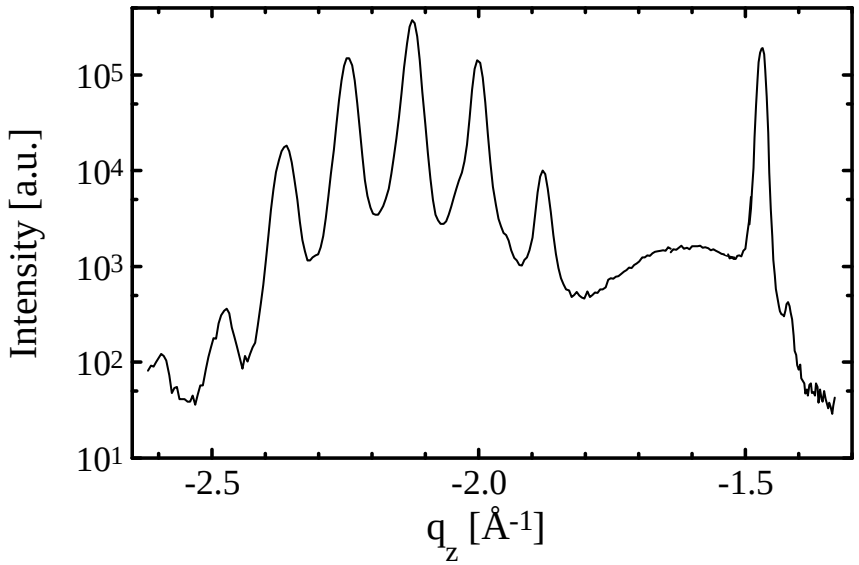

Figure 34. [10ℓ] scan on [$Fe_{20}V_{30}$] at 8500eV.

Figure 35 show two [10ℓ] scans on the [$Fe_{30}V_9$] superlattice. The units of the x-axis are reciprocal lattice units (r.l.u.) of the MgO substrate defined as 1 r.l.u. = $2\pi/a_{MgO}$= 1.492Å^{-1}.

In the upper part we have aligned the spectrometer on the superlattice (101) reflection. The broad peak at ℓ=1.05 is due to the Au (111) reflection from the cap layer and the background is mainly due to the tail from the MgO(111) reflection. The scattering from the Fe layers is about 20 times larger than from the V layers. This means that the influence of the V on the diffraction profile is small. Furthermore, the (110) reflections are closer to each other, and therefore we have a very symmetrical diffraction profile.

In figure 36 we have positioned the spectrometer on the central peaks of figure 35a and performed scans in the transverse direction. We observe that in addition to the intense central peak arising from our superlattice reflection, the transverse scans show a 'shoulder' at x=1.0 r.l.u.. Then we align the spectrometer on the commensurate position (1.0, 1.0, z) and perform another [10ℓ] scan, the result of which is shown in the lower part of figure 35. We see here that there appears

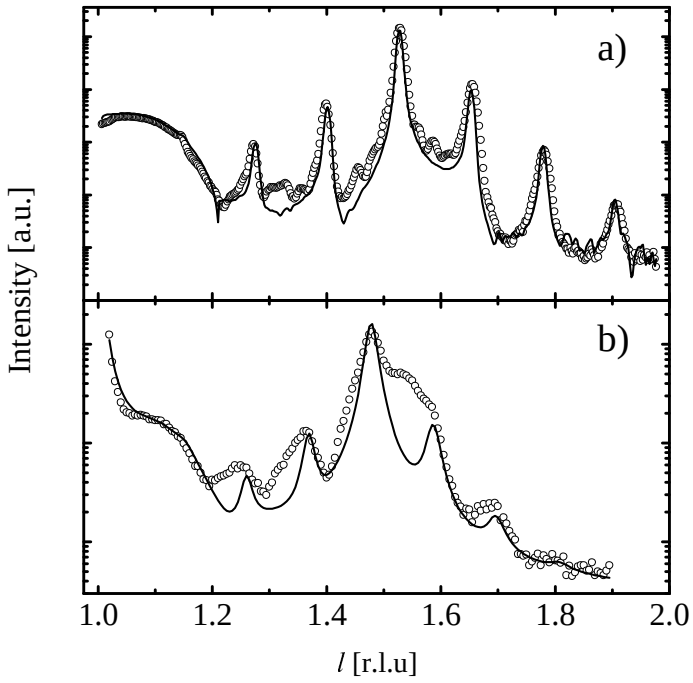

Figure 35. (1,0,ℓ) scans on [$Fe_{30}V_9$]. a) incommensurate component (1.02,0,ℓ) (○), fit (–) b) commensurate component (1,0,ℓ) (○), fit (–).

to be two components of the superlattice: one growing commensurately with the substrate and one growing incommensurately. The structural parameters of the fits of the two [10ℓ] scans are listed in table 2. The analysis shows that the incommensurate part of the superlattice is of high structural quality. The 'disorder' parameters σ_d and σ_n were found to be zero. The sigma parameters influence the line shape of the diffraction profile as well as the peak widths and relative intensities of the main peak to the side peaks. For the commensurate part of the superlattice both of these parameters had to be employed in order to model the data. This is consistent with the idea that the commensurate component is trying to adjust to the substrate lattice and thereby giving rise to more internal strain. We find that the lattice parameter in the modulation direction is smaller for the commensurate component which is what we would expect. In the commensurate component of the superlattice Fe is expanded to match the substrate lattice in the surface plane. It is therefore expected to compress along the modulation direction in order to conserve volume. For V the opposite behavior is observed.

In figure 37 we have plotted (h,l) for the peak positions in the two [10ℓ] scans. The solid symbols are the superlattice reflections, and the superlattice period of the two components can easily be identified. Also shown are the MgO (111) and the Au (111) reflections. From the latter we obtain the further information that the Au cap layer grows incommensurately with the superlattice. The unidentified peaks are denoted by open circles and an open square, and the grouping is our suggestion of how the peaks relate to each other. The superlattice model we use can not fit these peaks to the superlattice components. One possible explanation, which has not been investigated further, is that the two components of the superlattice are grown on top of each other. This would reduce the number of bi-layers for each superlattice. For a sufficiently small number of bi-layers, oscillations of the superlattice modulation could be seen between the main superlattice modulations.

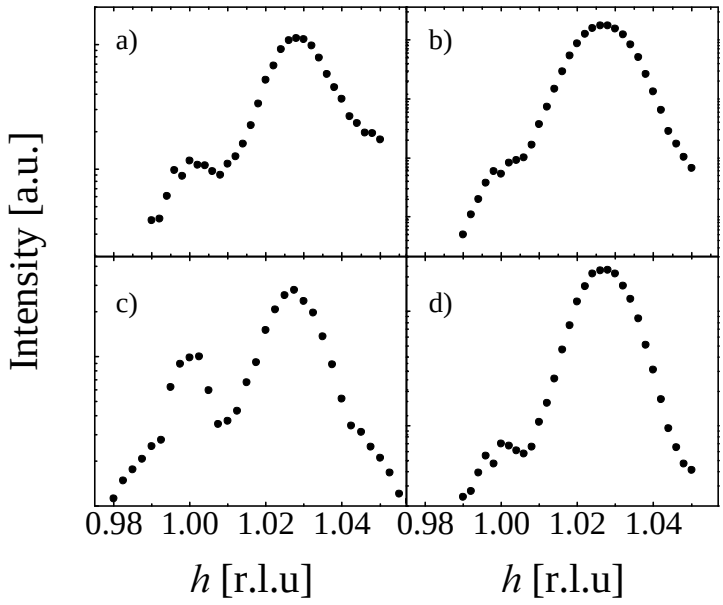

Figure 36. (h,0,z) scans on $[Fe_{30}V_9]$. a) z=1.395Å^{-1} b) z=1.457Å^{-1} c) z=1.505Å^{-1} d) z=1.673Å^{-1}.

		incommensurate		commensurate	
		Fe	V	Fe	V
d	[Å]	1.465	1.518	1.450	1.538
σ_d	[Å]	0.0	0.0	0.05	0.05
n	[ML]	22.4	4.00	20.8	5.55
σ_n	[ML]	0.0	0.0	0.5	0.5
δ_1	[Å]	0.0	0.0	0.0	0.0
δ_2	[Å]	0.0	0.0	0.0	0.0
d_{IF}	[Å]	1.56		1.45	
Λ	[Å]	39.0		38.6	

Table 2. Structural parameters for the commensurate and the incommensurate part of the $[Fe_{30}V_9]$ superlattice.

7.5 Energy scans

One example of the utilization of the tunability of the synchrotron x-ray wavelength is demonstrated in figure 38. Two identical $[00\ell]$ scans were performed on the $[Fe_{20}V_6]$ superlattice at energies of 7112eV and 7500eV. At an x-ray energy of 7500eV it is clearly seen that the background level is rather high. Comparing with the spectrum taken at the Fe K absorption edge at 7112eV we see that the background, which presumably arises from fluorescence from the Fe, is decreasing and that an extra superlattice peak at q=3.57Å^{-1} is visible.

Another example of the usefulness of tuning the wavelength is shown in figure 39. For the $[Fe_{20}V_{30}]$ superlattice we have positioned the spectrometer at a fixed value of the momentum transfer (q=4.507Å^{-1}) and then scanned the x-ray energy through the Fe K absorption edge at 7112 eV. In the upper part of the figure we see a regular dip in intensity when scanning through the edge, identifying Fe as the main source of the scattered intensity. In the lower part of the figure (q=4.023Å^{-1}) we mainly see an increasing background. In this way one can introduce another degree of element sensitivity to the diffraction analysis. Furthermore, one can even

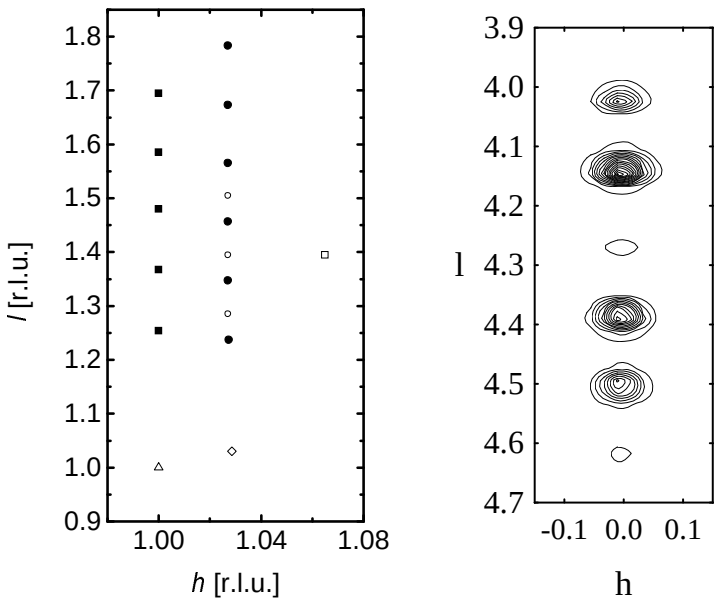

Figure 37. Left: reciprocal space-map in the vicinity of the (110) superlattice reflection for [$Fe_{30}V_9$]: (●) incommensurate component, (■) commensurate component, (△) MgO (111) reflection, (◇) Au (111) reflection. The peaks marked with (○) and (□) have not been resolved. Axis units are reciprocal lattice units of MgO. Only the peak positions are indicated. Right: reciprocal space map of the [$Fe_{20}V_{30}$] superlattice around the (002) reflection. Axis units are $Å^{-1}$.

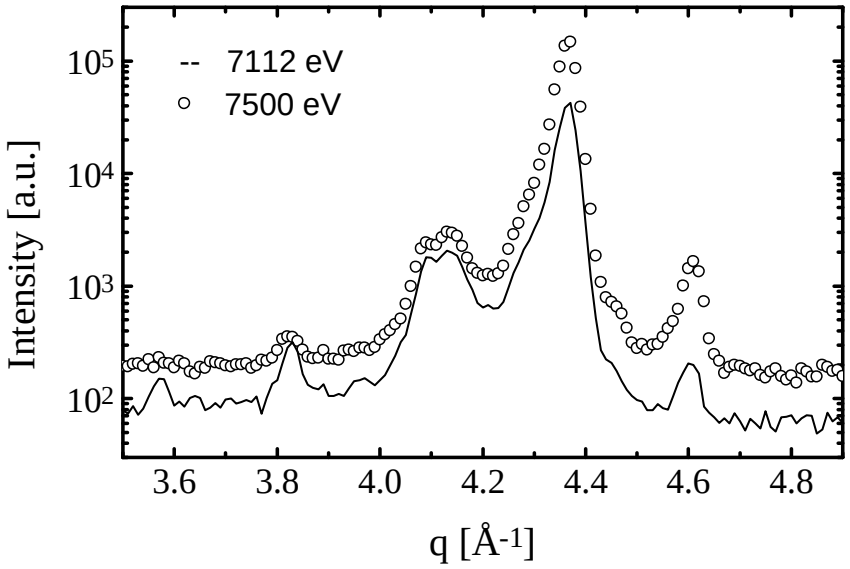

Figure 38. Two identical [00ℓ] scans on [$Fe_{20}V_6$].

use the absorption fine structure, clearly visible in the upper part of figure 39, to obtain information about the inter-atomic distances in the layers [50]. This could be especially useful when investigating superlattices where one element is in a structural transition and thereby may have a different number of nearest neighbors than for the bulk structure. At BW2 the energy interval within our reach is from 5000eV to 10000eV thus enabling us to perform energy scans over the absorption edges of elements from Ti to Zn which is nearly all 3d transition metals. However,

the instrumentation may impose certain limits of the actual range of reachable energies. This was the case during this study, where the absorption edge of V could not be reached.

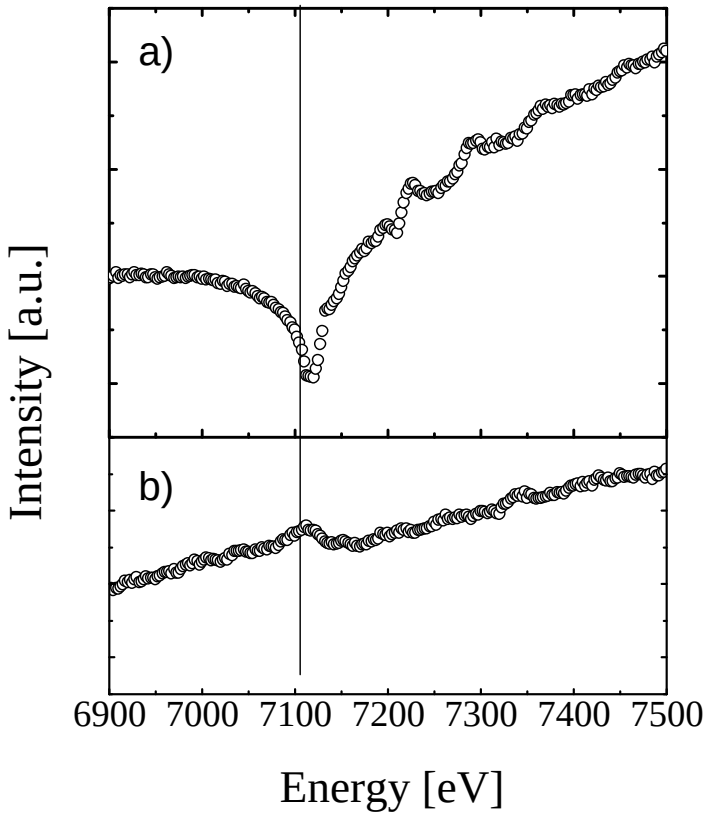

Figure 39. Energy scan on $[Fe_{20}V_{30}]$ through the Fe K edge. a) q=4.507Å^{-1}, b) q= 4.023Å^{-1}.

7.6 Growth temperature

In order to investigate the optimal growth temperature for the Fe/V system, a series of identical superlattices were grown at temperatures ranging from 393K to 813K. The low limit corresponds to the temperature of the sample after more than an hours cooling after the annealing. The high limit is chosen as 3/8 of the melting temperature of V.

For each superlattice, x-ray diffraction profiles were measured. Figure 40 show θ-2θ scans on $[Fe_{30}V_9]$ grown at 678K, 746K and 813K respectively. Two more $[Fe_{30}V_9]$ superlattices were grown at 393K and 523K.

Theoretical work has estimated that in order to grow metallic superlattices with good structural quality one should choose a substrate temperature of $3/8T_m$ where T_m is the melting point of the metal in consideration [26]. For Fe and V the melting temperatures are 1808K and 2163K respectively. Here it is not obvious which temperature one should apply, but an average gives a suggestion of 744K. We can easily see from figure 40 that a structural degradation has occurred at a growth temperature of 746K. For all five superlattices, $[10\ell]$ scans similar to the ones shown in figure 35 have been performed and the width of the central peak has been measured. The width is related to the structural coherence length along the modulation direction and a direct measure of the structural quality of

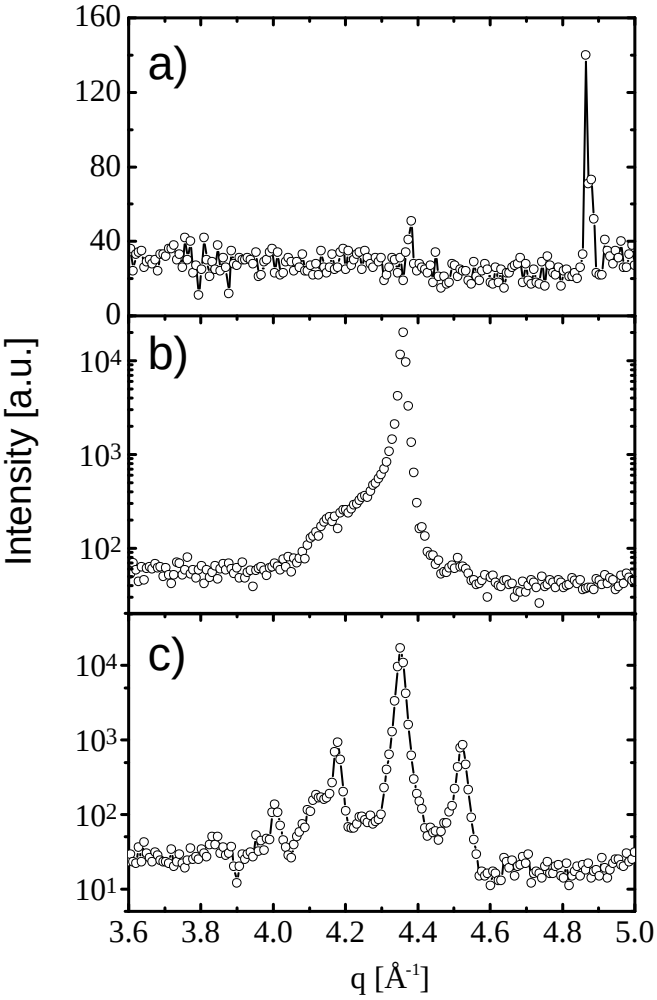

Figure 40. Identical [$Fe_{30}V_9$] superlattices grown at different substrate temperatures. a) T_g=813K, b) T_g=746K, c) T_g=678K.

the superlattices. Figure 41 shows the width of the central peak as a function of growth temperature. From this we estimate that the optimal growth temperature is about 600K. The data seem to preclude estimates for the lower limits of the growth temperature. Since mobility of the atoms on the surface is very important in the formation of smooth surfaces we suggest a growth temperature of 600K purely because no measurable degradation has occurred at this temperature. This is in agreement with a recent publication addressing the same issue [43].

7.7 Common properties

For all Fe/V superlattices investigated so far, there appears to be a tilt of the superlattice planes with respect to the substrate planes. This means that after aligning on the (002) MgO reflection, the spectrometer should be offset a small amount in θ in order to align on the superlattice peaks. Typical tilts are in the 0.1°–0.3° range but for [$Fe_{20}V_6$] the observed tilt was as large as 1.55° in a [100] direction. This matter has not been subject to further investigation. However, one could expect the elastic properties of the superlattices to play a fundamental role. For the Fe/V superlattices the width of the ω scans is typically 0.6°. The coherence lengths are about 450Å for the finest superlattices, corresponding to 56% of the

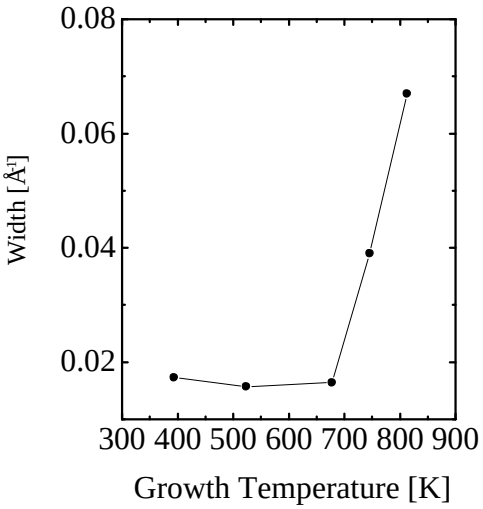

Figure 41. Width of the central superlattice peak for $[Fe_{30}V_9]$ as a function of growth temperature.

superlattice scattering coherent for $[Fe_{20}V_{30}]$ grown at 523K.

7.8 Discussion

When using the SUPREX program to fit the superlattice diffraction profiles one can in principle only fit θ-2θ or $[00\ell]$ scans. We have, however, used it to fit $[10\ell]$ scans as well. In order to do so we have taken advantage of the fact that the structure factor for a bcc lattice has the following symmetry: $F(h,k,l) = F(h-1,k,l+1)$, and applied the transformation on the (101) reflection. This is not strictly true for our superlattices because they are tetragonally distorted as discussed in section 5.3, but the error introduced is presumably small. The transformation will shift the derived lattice parameters slightly. This shift is, however, identical for the two spectra. Therefore the fit can still be used to compare the relative lattice parameters obtained from the analysis.

7.9 Summary

We have performed x-ray and neutron scattering experiments on Fe/V superlattices for structural analysis and comparison purposes. For the Fe/V system we have estimated the optimal growth temperature with respect to crystalline structure to be ≈600K and it is demonstrated that Fe/V superlattices of a high structural quality can be grown. Coherence lengths as large as 450Å have been observed. The Fe/V superlattices have been investigated by means of different types of scans in reciprocal space. These scans have provided evidence of coexisting commensurate and incommensurate components. All the investigated superlattices appear to be tilted a small amount with respect to the substrate and a tilt as large as 1.55° has been observed. The analysis gives estimates for the lattice parameters in the modulation direction of some superlattices which could provide a useful input to theoretical calculations where the bulk values traditionally are used. Examples of the advantages of the tunability of the synchrotron wavelength, applied to element specificity of the 3d transition metals are also given.

8 Cr/Mn superlattices

As mentioned in earlier sections, the interest in many superlattice systems stems from their magnetic properties. This is also the case for Mn, where total energy band calculations have predicted bcc Mn to be ferromagnetic at a cubic lattice parameter of $a = 2.79$Å [61]. Bulk Mn occurs in four different structures depending on temperature: α, β, γ and δ-Mn all of which are cubic structures with the number of atoms per unit cell ranging from 58 in α-Mn (see figure 42) to 2 for body centered cubic δ-Mn. Bcc δ-Mn is normally found at temperatures from 1143°-1290°C. The Cr/Mn system has been investigated with the primary focus on stabilizing the δ-Mn modification at room temperature [73]. For an account of other work on superlattices containing Mn as one constituent we refer to reference [72] and references therein.

The investigation presented in this section, is an attempt to provide detailed structural information for a series of Cr/Mn superlattices. The superlattices have been grown at the university of Konstanz on Ge and MgO substrates. In the case of the transition metals Cr and Mn, the bulk lattice constants at RT are $a_{Cr} = 2.884$Å [95], $a_{Mn} \approx 2.87$Å[14]. The lattice parameters of the substrates $a_{MgO} = 4.211$Å and $a_{Ge} = 5.657$Å both have a reasonable lattice match with Cr and Mn with the crystallographic orientations as explained in section 8.2.

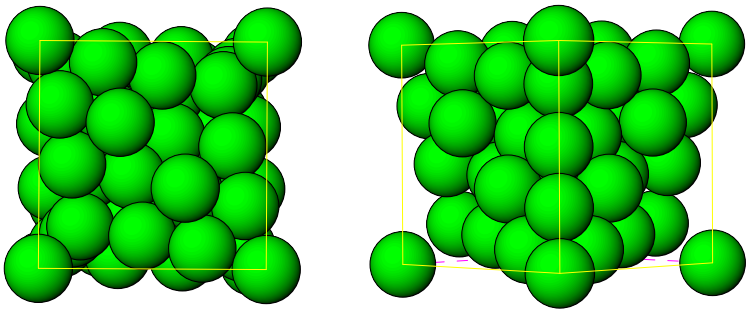

Figure 42. The α-Mn unit cell. Left: Viewed from the (100) direction. Right: Viewed from the (110) direction. The cube edge is 8.894Å.

8.1 Substrates and film growth

The substrates were: MgO(001)[15] with a miscut of less than 0.075°, Ge(001)[16] with a miscut of less than 0.01°. The MgO substrates were cleaned in Methanol and were then annealed at 600°C in ultra high vacuum for 30 minutes. The Ge substrates were Argon ion sputtered at 600°C for 12 hours. Auger electron spectroscopy revealed a small amount of carbon on the MgO substrates and virtually no contamination was seen on Ge. After in-situ annealing we let the samples cool, and started depositing the metals at 50°C. During growth the substrate temperature was in the range 50°C to RT. This is probably not the optimal temperature

[14]The value has been estimated by considering the lattice parameters of the neighboring bcc elements Cr and Fe, and is meant as a starting point for the investigation only.
[15]The MgO substrates were produced by Kelpin Kristallhandel, Germany.
[16]The Ge substrates were produced by Semiconductor processing company, USA.

with respect to crystalline quality of the superlattices [26], but other considerations such as well-defined interfaces with low interdiffusion for future magnetic investigations had to be taken into account. The MBE equipment is discussed in detail in reference [74]. Therefore, we will just mention that the metals are evaporated by electron beam evaporators and that the MBE system is equipped with a quartz microbalance for monitoring the deposition rates. In this MBE system a systematic deviation between the nominal thickness of the superlattices, derived from the quartz microbalance, and the results obtained from x-ray diffraction is also observed. The deviation is typically of the order of 6% and is discussed in section 3.1. Reflection high energy electron diffraction (RHEED) was used for monitoring the epitaxy, and for measurement of the in-plane surface lattice constants during growth. The samples were 1cm×1cm for MgO and 1cm×0.5cm for Ge. All superlattices were grown on a 20Å Fe seed layer and were terminated by a 40Å Cr cap layer. We denote the superlattices $[Cr_{40}Mn_x]_y$, with Mn thicknesses of 10, 15, 20 and 30Å respectively and the repetitions, y, adjusted to keep the total film thickness fixed at ≈2000Å. For the purpose of comparison between the two substrates two nominally identical superlattices with a Mn thickness of 20Å were grown: One on Ge(001) and one on MgO(001). Although it would be preferable to grow such superlattices simultaneously this is not possible with the MBE equipment. The samples were not rotated during growth.

8.2 Experimental details

The two types of scans were performed on the rotating copper anode at Risø in a standard two-axis setup for the θ-2θ scans and a four circle setup for the in-plane scans [48]. The four circle setup used a graphite monochromator and two pairs of double slits for controlling the beam divergence and the resolution of the spectrometer. The latter was estimated by the width of the Ge (004) peak to be 0.01Å^{-1} in the longitudinal direction. Sample alignment was done on the MgO {002} and Ge {004} reflections respectively. The crystallographic relations between the substrate and the superlattice (SL) are: $2a_{SL} \approx a_{Ge}$ and $\sqrt{2}a_{SL} \approx a_{MgO}$. Thus we expect that for Ge the axis of the unit cells are parallel, whereas for MgO they are rotated 45° relative to each other. In reciprocal space we then have SL(110) reflections coinciding with Ge(220) and with MgO(200) reflections. Scans along the modulation direction are denoted $[00\ell]$ scans and here $[001]_{SL} \parallel [001]_{MgO,Ge}$. For the in-plane measurements we scan in the $[110]_{Ge}$ direction through the $(110)_{SL}$ reflection for Ge substrates and in the $[100]_{MgO}$ direction through the $(110)_{SL}$ reflection. Only the $\{110\}_{SL}$ reflections were measured. Figure 43 shows the crystallographic orientations in reciprocal space as well as the scanning directions. The θ-2θ diffraction patterns were fitted with the model described in section 5.2.

The model operates with a superlattice description which have a number of parameters for each component of the superlattice as well as for the bi-layer. For each material X there is a 'bulk' value for the lattice parameter d_X and a non-integer number of scattering planes n_X with a fluctuation width of σ_{n_X}. In addition to this it is possible to introduce relaxation of the outmost three scattering planes of the layers. The lattice parameter of layer i is $d + \delta_1 e^{-\alpha i}$ (i=0,1,2) with α fixed at 0.55 [27]. For the bi-layer there are two parameters of interest: The number of bi-layers N and the interface distance d_{IF}. Only the interface distance was varied in the fitting procedure. Finally, the fitted spectrum was convoluted with a Gaussian resolution function.

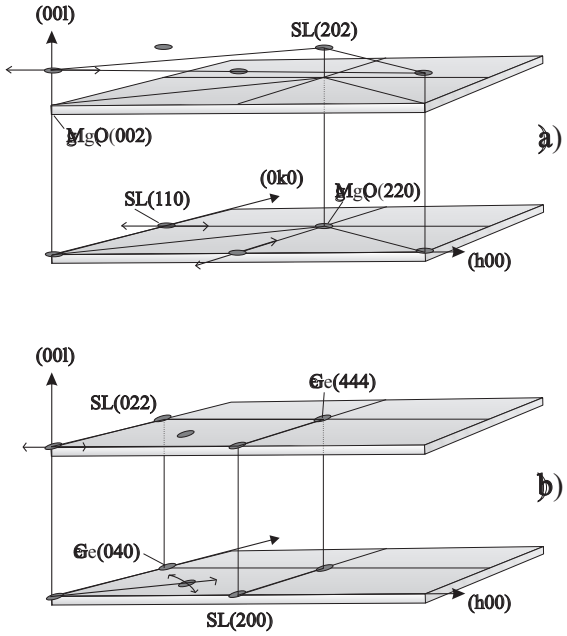

Figure 43. The crystallographic orientations of the superlattices viewed in reciprocal space. The two planes symbolize the substrate (hk0) and (hk2) planes, and the solid circles are the superlattice reflections. a) Superlattice orientation with respect to the MgO(001) substrate. The solid lines indicate half of the superlattice fcc unit cell. b) Ge(001). The solid lines indicate the fcc unit cell. For both figures some superlattice reflections have been omitted for clarity. The double arrows indicate the transverse scans through the superlattice reflections.

8.3 Results

Figure 44 shows the result of $[00\ell]$ scans performed on the superlattices grown on MgO(001) substrates together with the fitted spectra. Figure 45 shows $[00\ell]$ scans on the superlattices grown on Ge(001). The peak at 4.44Å^{-1} is the Ge(004) reflection. For superlattices grown on Ge(001) a Lorentzian centered at q=4.44Å^{-1} was added in order to fit the spectra.

In table 3 and 4 we list the structural parameters obtained from the analysis. It is seen that for all superlattices the lattice parameter of the Cr layers is very close to its bulk value. Since d_{IF} is of the order $d_X/2$, we estimate that the interfaces are relatively well defined with at most one monolayer of intermixing between Cr and Mn. The low values for the fluctuation of the layer thickness σ_n indicate that the manufacturing process is well controlled. We also see that both for Cr and Mn it was necessary to introduce relaxation/compression at the interfaces. When this is the case we have to calculate the average lattice parameters for the layers $\bar{d}_X$ from the parameters d_X, n_X and δ_i. These are listed in table 5. Here we observe that within the uncertainties of the parameters the lattice parameter for Cr can be regarded as constant, whereas the lattice parameter for Mn increases monotonically with the thickness of the Mn layer. Figure 46 shows the variation of the Mn lattice parameter with Mn thickness. Generally, the modelled intensity fits the experimental data quite well. For the superlattice with 10Å Mn (Figure 44a) it was necessary to employ a continuous fluctuation of the interface distance $\sigma_{d_{IF}} = 0.17$ in order to correctly fit the line profile. For the other superlattices no fluctuation of d_{IF} was employed.

Figure 47 shows two typical in-plane scans for Cr/Mn superlattices on MgO and

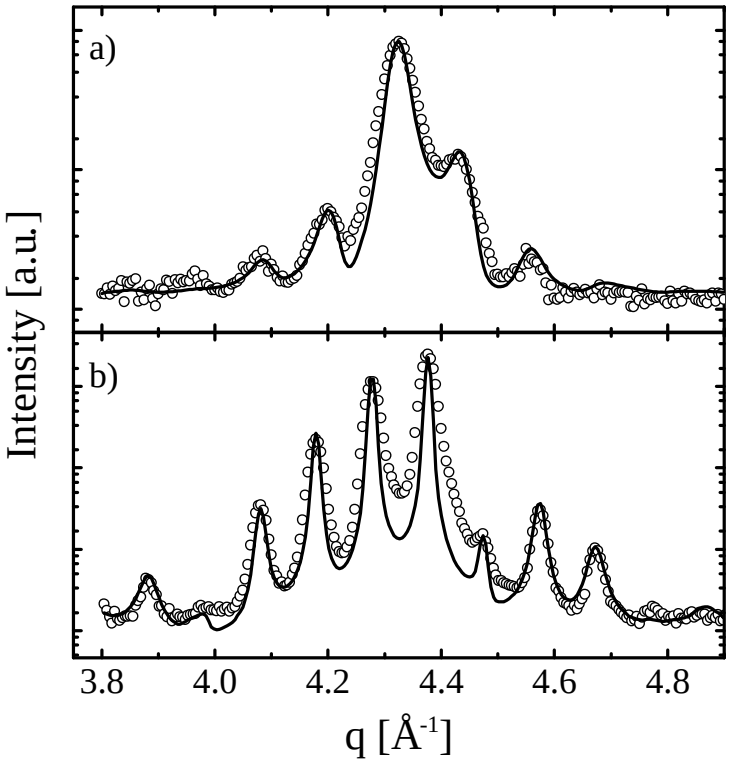

Figure 44. θ-2θ scans of Cr/Mn superlattices on MgO(001) (○), SUPREX fit (–). a) $Cr_{40}Mn_{10}$, b) $Cr_{40}Mn_{20}$.

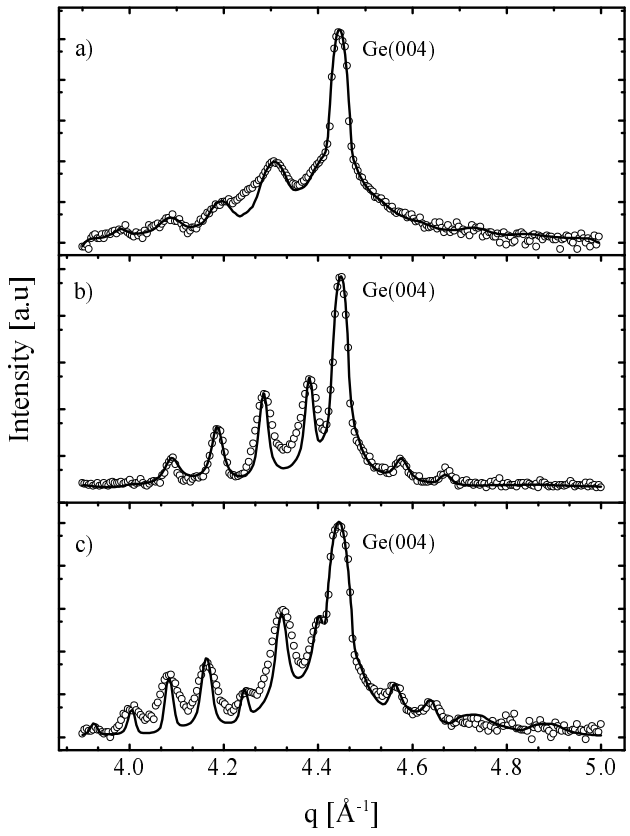

Figure 45. θ-2θ scans of Cr/Mn superlattices on Ge(001) (○), SUPREX fit (–). a) $Cr_{40}Mn_{15}$, b) $Cr_{40}Mn_{20}$, c) $Cr_{40}Mn_{30}$.

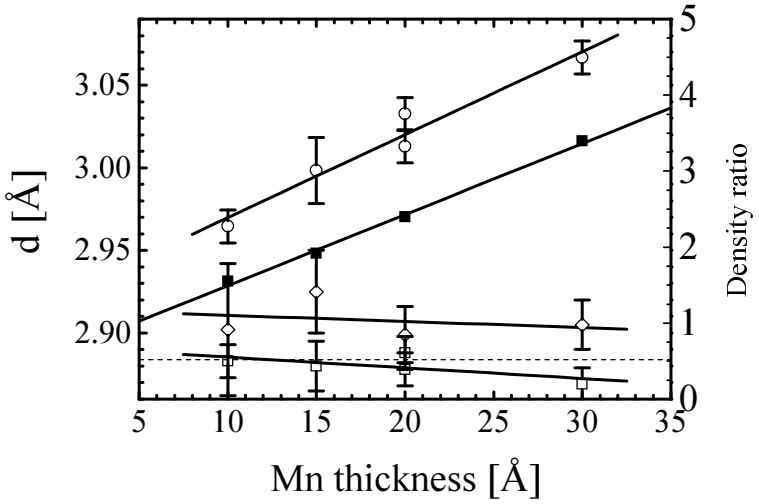

Figure 46. Left axis: Lattice parameters of Cr (□) and Mn (○) in the modulation direction and the common Cr/Mn in-plane lattice parameter (◇) as a function of layer thickness. The bulk value of the Cr lattice parameter (dashed line) is also indicated. Right axis: Density ratio η_{Cr}/η_{Mn} (■) as a function of Mn layer thickness.

Ge. For clarity we show one scan only for each substrate. Since the other scans are very similar we simply quote the results in table 5. For the Mn_{30} superlattice grown on Ge(001) we observe two main peaks: one originating from the superlattice at q= 3.063Å^{-1} and one from the Ge(220) reflection at q= 3.139Å^{-1}. We therefore conclude that Cr/Mn superlattices grow incommensurately on Ge(001). In addition to these peaks we see two small peaks below 2.9Å^{-1}. Transverse scans on the peaks show that they arise from polycrystalline material, presumably oxides on the surface of the samples. Since we believe that the peak at q= 3.063Å^{-1} is composed of both the Cr and the Mn (110) reflections, the width represents a minimum coherence length of the superlattice in the plane. For the same reasons, the uncertainties of the peak position, $\Delta_q = \pm 0.020$Å^{-1}, arise from the the distance between the peak positions of the two Gaussians fitted to the peak. For $[Cr_{40}Mn_{10}]$ on MgO we see one broad peak at q= 3.06Å^{-1}, which we interpret as the SL(110) reflection. This also means that the superlattice grows incommensurate with the substrate. Again, we see a peak below q= 2.9Å^{-1} which is thought to arise from polycrystalline material on the surface. For $[Cr_{40}Mn_{20}]$ grown on MgO we were unable to find the superlattice in-plane reflection.

We find that the coherence length along the modulation direction is larger for superlattices grown on Ge(001) than on those grown on MgO(001). The coherence lengths along the modulation direction ranges from 180Å to 600Å increasing with Mn thickness. The coherence length in the plane ranges from 140Å to 300Å. Table 5 shows the calculated tetragonal distortion c/a as a function of Mn thickness. It is seen that the c/a ratio increases with Mn thickness from $c/a = 1.022$ for $[Cr_{40}Mn_{10}]$ to $c/a = 1.056$ for $[Cr_{40}Mn_{30}]$.

8.4 Discussion

Here we first comment on the method we used to simulate the diffraction profile. In order to correctly fit the obtained spectra it was necessary to vary the densities ρ_X for the Mn and Cr layers. In the model the total scattering power of an atomic

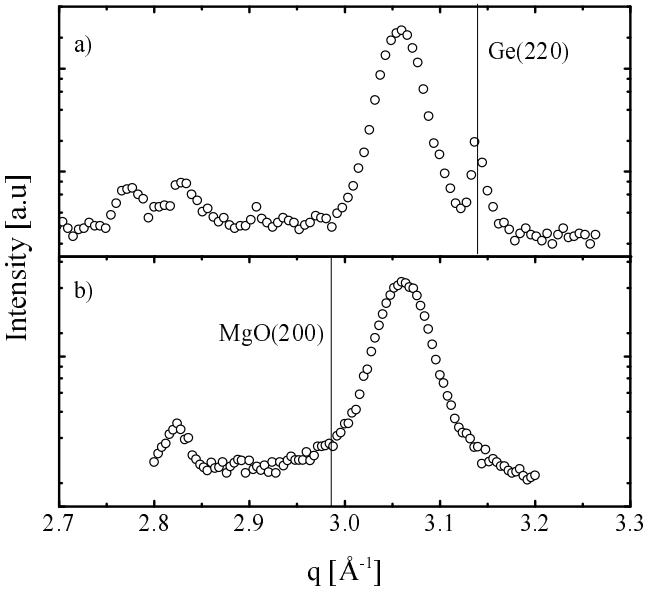

Figure 47. In-plane scans of Cr/Mn superlattices (○): a) $Cr_{40}Mn_{30}$ on Ge(001), b) $Cr_{40}Mn_{10}$ on MgO(001). The vertical lines indicate the positions of the substrate bulk reflections.

layer [27] is given by

$$\tilde{f}(q) = \rho_X f(q) F_{DW}(q) \tag{37}$$

where ρ_X is the density, F_{DW} is the Debye-Waller factor, $f(q)$ is the atomic form factor in which is included the small corrections Δf' and Δf".

This is generally valid for perfectly crystalline systems which always remain in the same structure. The effect of the Debye-Waller factor is to decrease the scattered intensity due to lattice vibrations in the material. In our case, we have a tetragonal distortion developing with the Mn thickness as presumably Mn is seeking its room temperature α structure. Therefore, disorder develops within the Mn layers as the thickness increases. This is not easily modelled within the framework of the described model.

The structure factor of the superlattice is proportional to the structure factor of the bi-layer, which we rewrite as

$$F_{SL}(q) \propto f_{\mathrm{Cr}} F_{\mathrm{Cr}}(q) + \frac{\eta_{\mathrm{Mn}}}{\eta_{\mathrm{Cr}}} f_{\mathrm{Mn}} F_{\mathrm{Mn}}(q) \tag{38}$$

where we define $\eta_X = \rho_X F_{DW}$. In our modeling we vary the ratio $\eta = \eta_{\mathrm{Cr}}/\eta_{\mathrm{Mn}}$. By doing so, we collect density changes, Debye-Waller factors and relative scattering power in one parameter. It is important to stress that η now represents a measure of the relative scattering intensities between the two materials. This means that changes in η are not necessarily caused by changes in Debye-Waller factors, but could also be due to reduced scattering power in for example the Mn layers. The model contains parameters for continuous fluctuations of lattice parameters which in come cases are relevant for fitting the spectra, but which are not applicable in our case [27]. We therefore have chosen the much simpler method described above, which reduces the number of parameters needed to fit the spectra by at least five. In figure 46 we show $\eta_{\mathrm{Mn}}/\eta_{\mathrm{Cr}}$, and it is seen that the ratio increases from 1.5 to 3.4 with increasing Mn thickness. This means that considerable disorder develops in the Mn layers, which is in expected when the Mn

is in the metastable δ-state transforming into the stable α-state with increasing thickness.

Since there are a large number of parameters that can be used to fit the spectra, one can often doubt the validity of the fit. This doubt can be effectively removed if one considers series of superlattices, because irregularities in the obtained parameters will show up very clearly. In our case, all layer thicknesses, number of scattering planes n, fluctuations σ_{n} and interface distances are seen to be consistent in all fits. With respect to production and reproducibility we see that the measured modulation thickness Λ is in good agreement with the nominal thicknesses with a positive deviation of about 6% except for the thickest film where the deviation is as large as 12.5%. This is not an indication of the precision of the MBE equipment but rather a matter of calibrating the quartz monitor. For the two superlattices with 20Å Mn the difference between the obtained bi-layer thickness is less than 0.8%. This comparison illustrates one advantage of using MgO substrates over Ge: we avoid the placement of a substrate peak in the middle of the superlattice profile, which otherwise would complicate the fitting. This may also ensure that no peaks are left out from the fitting, since a superlattice satellite can be hidden in the scattering from the Ge (004) reflection.

8.5 Summary

We have investigated Cr/Mn superlattices with x-ray diffraction in scattering geometries, probing momentum transfers along the modulation direction as well as in-plane. The superlattices grown on MgO(001) and Ge(001) substrates have a fixed Cr thickness, and the variation of the lattice parameter of Cr and Mn as a function of Mn thickness has been presented. The Mn lattice parameter is found to vary from 2.96Å to 3.03Å when the Mn layers range from 10Å to 30Å, whereas Cr can be regarded as having its bulk lattice parameter. In-plane scans show a constant common lattice parameter of Cr and Mn of 2.91Å. In-plane scans are demonstrated to be a good supplement to the standard diffraction techniques, and can be readily performed on a rotating anode with a four-circle geometry. The in-plane lattice constants are in agreement with RHEED measurements during deposition. Since RHEED is surface sensitive, we conclude that in this case no atomic rearrangement is occurring upon termination of the surface. The tetragonal distortions of Mn are found to be in the range 1.022 to 1.056.

The superlattices grown on Ge(001) generally show a better coherence along the modulation direction than those grown on MgO(001). We attribute this to the lower misfit between Fe and Ge (+1.4%) compared to Fe on MgO (-3.9%). If this is the case, it is remarkable that only 20Å Fe is enough to cause this difference throughout a superlattice thickness of 2000Å.

We introduce a simple model for taking structural disorder into account and the result of the analysis is in agreement with the idea that the Mn thin films are in a transition region between the metastable tetragonal distortion of δ-Mn and the stable α-Mn.

		$[Cr_{40}Mn_{10}]$		$[Cr_{40}Mn_{20}]$	
		Cr	Mn	Cr	Mn
d	[Å]	2.887	2.946	2.895	2.983
n	[ML]	15.2	4.37	15.2	7.5
σ_n	[ML]	0.8	0.6	0.9	0.3
δ_1	[Å]	-0.025	0.027	-0.041	0.06
δ_2	[Å]	-0.025	0.027	-0.015	0.08
Λ	[Å]	53.9		63.6	
d_{IF}	[Å]	1.538		1.529	

Table 3. Structural parameters of the superlattices grown on MgO(001) derived from SUPREX. d are the lattice constants of the superlattice components along the modulation direction. n is the number of scattering planes, σ_n the fluctuation in the number of scattering planes. δ_d is the interface relaxation, Λ is the modulation thickness and d_{IF} is the interface distance. Errors on the lattice parameters are ≈0.01Å.

		$[Cr_{40}Mn_{15}]$		$[Cr_{40}Mn_{20}]$		$[Cr_{40}Mn_{30}]$	
		Cr	Mn	Cr	Mn	Cr	Mn
d	[Å]	2.887	2.987	2.882	3.020	2.869	3.071
n	[ML]	14.9	6.0	15.23	7.62	14.91	11.69
σ_n	[ML]	1.0	0.4	1.2	0.4	0.3	0.3
δ_1	[Å]	-0.025	0.021	-0.041	0.021	0.0	-0.03
δ_2	[Å]	-0.025	0.042	-0.015	0.035	0.0	0.01
Λ	[Å]	58.1		64.1		78.8	
d_{IF}	[Å]	1.527		1.528		1.519	

Table 4. Structural parameters obtained from the fit for the superlattices grown on Ge(001). The parameters are explained in table 3. The error on the lattice parameters is about 0.013Å.

		Mn10	Mn15	Mn20	Mn20	Mn30
Substrate		MgO	Ge	MgO	Ge	Ge
$\bar{d}_{Cr}$	[Å]	2.883	2.880	2.888	2.878	2.869
$\bar{d}_{Mn}$	[Å]	2.965	2.998	3.013	3.033	3.067
$\bar{d}_{inplane}$	[Å]	2.902	2.925	n/a	2.899	2.905
c/a		1.022	1.025	n/a	1.046	1.056
ξ	[Å]	179	240	362	419	598
$\xi_{inplane}$	[Å]	166	140	n/a	300	228
η_{Cr}/η_{Mn}		1.55	1.92	2.4	2.4	3.4

Table 5. Average lattice parameters of Cr and Mn calculated from the data in table 3 and 4 and the common in-plane lattice parameter for the Cr/Mn calculated from scans similar to fig. 47. The tetragonal distortion c/a and the coherence lengths, ξ, in-plane and along the modulation direction. For unavailable parameters n/a is printed. Also shown is the ratio η_{Cr}/η_{Mn}.

9 Mn/X superlattices

In the previous section, an investigation of Cr/Mn superlattices with Mn layers from 10Å to 30Å was described. Here, we report on a study of V/Mn, Cr/Mn and Fe/Mn superlattices with very thin Mn layers, ranging from 5Å and up to 12.5Å. The V,Cr and Fe layers were 11Å thick and the superlattices have 40 repeats. The samples were grown on Ge (001) substrates on a 11Å thick Fe seed layer, and were terminated by 15 Å of V or Cr. The thickness of the Mn layers was chosen such that manganese was stabilized as δ-Mn [73]. The superlattices were grown at the University of Konstanz, where The x-ray scattering also was performed. The MBE equipment and the diffractometer are described elsewhere [72].

9.1 Initial analysis

Figure 48 shows the average lattice parameters derived from the position of the superlattice (002) reflections from figures 49, 50 and 53. Compared with the lattice parameters of bulk V (3.0231Å), Cr (2.8846Å), and Fe (2.8664Å), we find that the average lattice parameter is reduced for the V/δ-Mn system, whereas the average lattice parameters are increased for both the Cr/δ-Mn and the Fe/δ-Mn system. This can easily be explained by assuming a lattice parameter for δ-Mn somewhere between that of V and those of Cr and Fe. An increase of the lattice parameter of δ-Mn with respect to the Cr bulk lattice parameter is demonstrated for Cr/δ-Mn superlattices in reference [73].

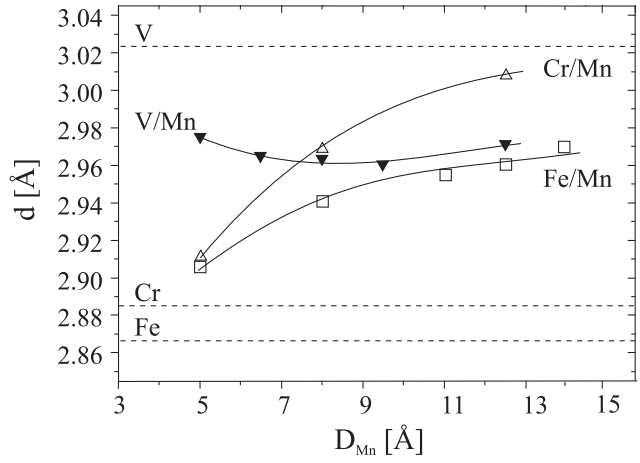

Figure 48. Average lattice parameter d in growth direction as a function of Mn thickness for $[M_{11}Mn_x]$ superlattices (M=Fe,V and Cr). Dashed lines represent bulk values for V, Cr and Fe, solid lines are guides to the eye.

9.2 Simulations

Figures 49 and 50 show the θ-2θ-scans of the V/δ-Mn and the Cr/δ-Mn superlattices together with the fitted spectra. All experimental data are corrected by Lorentz, polarization, and geometry factors. Simulations on the analogous series of Fe/δ-Mn superlattices fail, most probably due to a different stacking sequence or interdiffusion. The Fe/Mn measurements are shown in figure 53. We will comment on these superlattices later.

Satellite intensities are observable in our transition metal/δ-Mn superlattices when the Mn layers are thicker than 5Å ($\approx$ 3-4 ML). The number of satellites increases with increasing bilayer thickness Λ, and so do their intensities. The peak at $2\theta \approx 66°$ is the Ge(004) reflection, for which we have chosen a Lorenzian line shape, and subtracted its intensity from the original data prior to fitting.

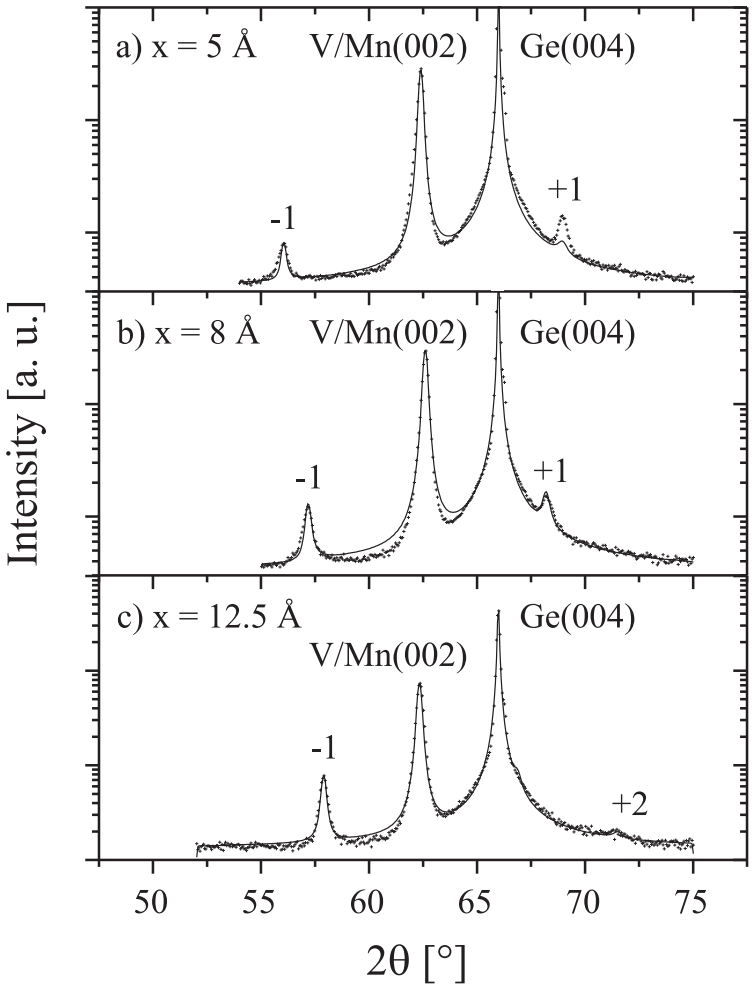

Figure 49. x-ray diffraction patterns and fitted results of V/δ-Mn-superlattices: a) [$V_{11}Mn_5$], b) [$V_{11}Mn_8$], c) [$V_{11}Mn_{12.5}$].(+): experimental data, (solid lines): fit. The satellites are denoted by their negative or positive orders).

All simulated data fit the experimental data very well, except figure 49(a), where we did not completely succeed in raising the intensity of the right first order satellite to the experimental values. In order to correctly fit the experimental spectra, it was necessary to model the distortions near the interfaces independently and sometimes even with opposite sign. This is a more complicated behavior than observed in section 8.3, where relaxation near the interfaces was symmetrical. Although the nomenclature of the superlattices indicates a symmetric stacking, this is not necessarily so: When growing a superlattice, we first produce one interface by growing material B on top of material A, whereas the next interface is made by growing A on top of B. This may well give rise to different distortions on successive interfaces. This behavior is displayed in figure 51, where the unstressed films A and B have different in-plane lattice parameters and therefore different

distortions in the growth direction for two adjacent interfaces.

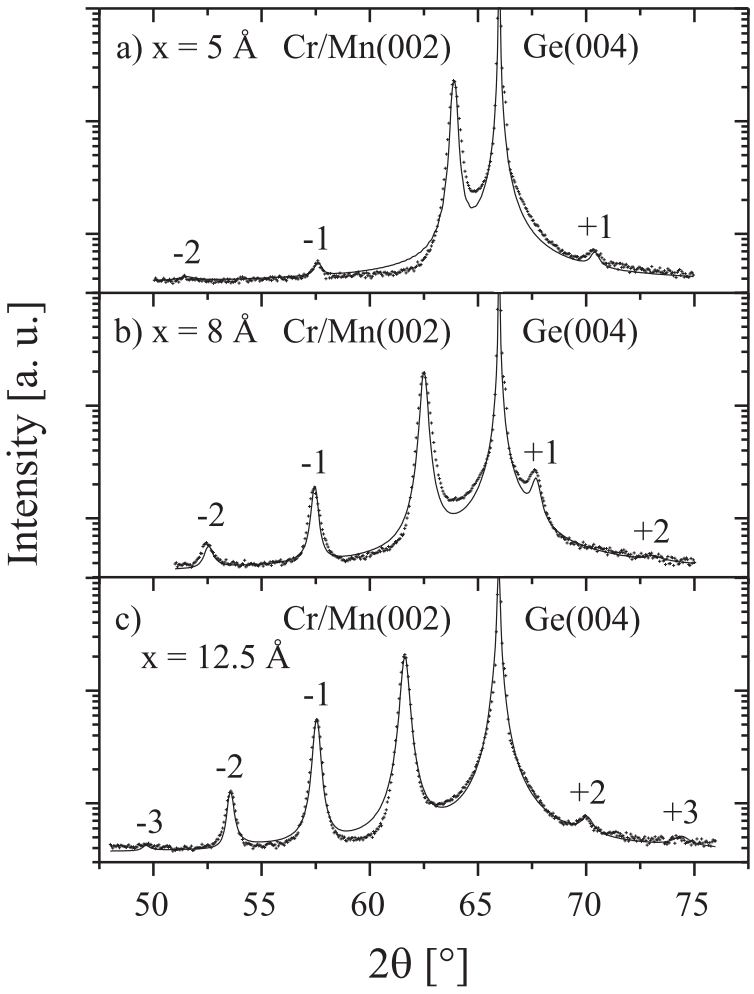

Figure 50. x-ray diffraction patterns and fitted results of Cr/δ-Mn-superlattices: a) [$Cr_{11}Mn_5$], b) [$Cr_{11}Mn_8$], c) [$Cr_{11}Mn_{12.5}$]. (+): experimental data, (lines): fit. The satellites are denoted by their negative or positive orders).

Although this simple picture does not fit all our results, it serves quite well to illustrate the occurrence of a non-symmetrical behavior at the interfaces. One may doubt whether the assumption of a constant unit cell volume is valid for thin films. But experiments show that even 500Å V on Ge(001)Fe_{11} has a larger lattice parameter in growth direction than expected from its bulk value. This is due to the large lattice mismatch of more than 5% between Fe and V. Therefore, the interpretation that the V expands in the growth direction to preserve its volume is well justified.

Despite the preceding discussion, not all distortions could be fitted with opposite sign. Although x-ray diffraction is a very powerful tool for structure determination, it still remains an integral method. It is therefore unlikely that x-ray diffraction will allow the determination of the very last details in systems consisting of a few monolayers only.

Since the discussed distortions have a large influence on the simulated intensity profile, we have tried to keep the fluctuations of the lattice parameters σ_d and the number of monolayers σ_m small when simulating the diffraction patterns. In

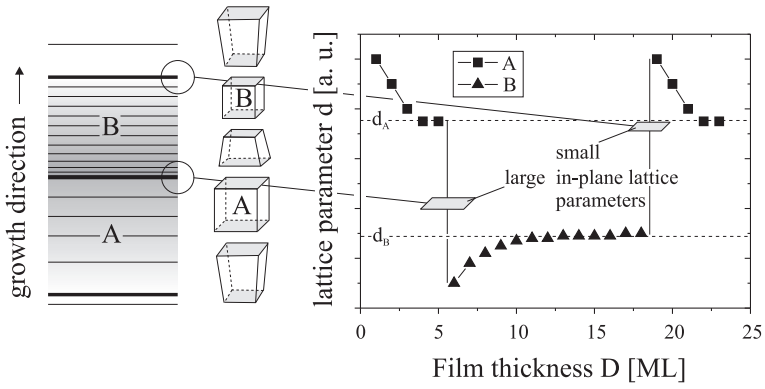

Figure 51. Model of a superlattice built up of the elements A and B having different (cubic) lattice parameters dA, dB. Assuming a constant unit cell volume and relaxation in the uppermost layers only, the interfaces will show a modulation in the lattice spacing distortions in growth direction. Dashed lines represent bulk lattice parameters for the elements A and B.

both the V/Mn and Cr/Mn systems, the number of bilayer repetitions had to be decreased for Mn thicknesses of 12.5Å in order to fit the widths of the satellites. The broadening of the peaks are likely to result from evolving structural disorder in the Mn layers as discussed in the previous section. The structural parameters are listed in tables 6 and 7.

As mentioned earlier, there is a deviation from the nominal thickness derived from the quartz monitor, and the measured thickness. The deviation is found to be less than 10% for the Cr/Mn system and less than 3.5% for the V/Mn system. One has to keep in mind that these values represent systematical but not statistical deviations, for they result from geometrical reasons during the individual growth processes. Since we use the density of the α-Mn modification for calibration of the quartz microbalance, the apparent increase in the bilayer thickness Λ is in fact an additional indication for an increased lattice parameter of the δ-Mn modification, corresponding to a reduced density in growth direction.

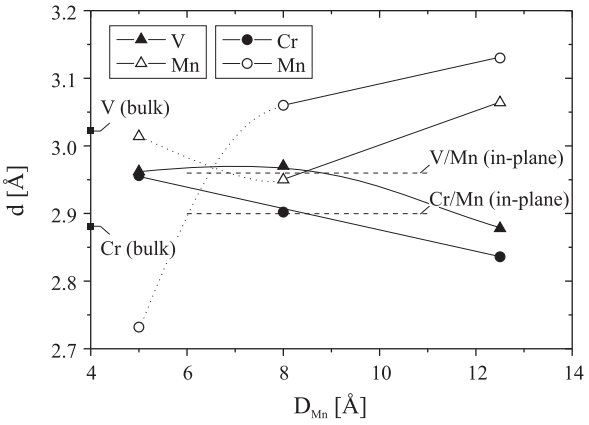

Figure 52. Lattice parameters d in growth direction for superlattices (M11Mnx)40.5, (M = V, Cr) as a function of the Mn layer thickness DMn. The values are calculated from tables 6 and 7, with respect to the definitions in figure 26. Dashed lines represent in-plane lattice parameters for thin V/δ-Mn and Cr/δ-Mn superlattices, straight and dotted lines are guides to the eye.

The real average values for the lattice spacings are shown in figure 52. To obtain these, we have summed up all individually calculated layer spacings from the values of tables 6 and 7. For the V/Mn and Cr/Mn systems the δ-Mn lattice

parameter increases with layer thickness, while the values for V and Cr decrease. The maximum lattice parameter for δ-Mn is about 3.06Å for the V/Mn series and 3.13Å for Cr/Mn. The resulting values for D_{Mn}= 5Å have to be interpreted with caution. In-plane lattice parameters of a similar series of M/δ-Mn superlattices, derived from other x-ray measurements [14], are also shown in figure 52.

As pointed out earlier, we did not succeed in simulating the observed intensities for the Fe/δ-Mn superlattices (figure 53). Here, the positions of the negative satellite orders seem to be influenced somehow, for they are not commensurate with the rest of the intensity profile. From investigations by means of magnetic measurements using a Faraday-susceptometer [1], it is very likely that intermixing takes place at the interfaces. The range of intermixing is found to correlate with the thickness of the Mn layers. We emphasize that fluctuations of the bilayer thickness Λ, possibly caused by the large total film thicknesses, can definitely be ruled out. Since Cr and Fe have almost identical lattice parameters, and the slope of the average lattice parameters of the Fe/δ-Mn system behaves very similar to that of the Cr/δ-Mn system (see figure 48), we suggest that, despite the occurrence of intermixing, a similar structural discussion for the Fe/δ-Mn system is valid.

Finally, the x-ray diffraction patterns of identical M/δ-Mn-superlattices (M = V, Cr or Fe) are shown in figure 54 for comparison. The difference in appearance, corresponding to a different crystallographic behavior, is evident.

9.3 Discussion

We have calculated the unit cell volume for the δ-Mn phase by using the lattice parameters a and c, from the in-plane measurements and the simulations respectively (figure 52). By averaging all data, excluding Mn thicknesses of 5Å, we derive a unit cell volume of about 26.68 $\pm$1.25Å^3, resulting in a cubic lattice parameter of $a = 2.985 \pm 0.05$Å. As pointed out in the previous discussion of figure 48, this value lies between the lattice parameters of V and Cr (or Fe). The most important result is that where the V in the V/δ-Mn system contracts in-plane as well as in the growth direction, we find δ-Mn to have an almost cubic structure for thin Mn layers in the V/Mn system. The behavior of V in the superlattice is quite unexpected, since it is different from the observed distortions of a single V film. This is not yet understood, but a similar behavior has been observed for Ce(111) grown on V(110) substrates [24, p.1310].

Nevertheless, the V/Mn system is found to be the first system, in which the high-temperature bcc δ-Mn modification has been stabilized.

9.4 Summary

We have compared superlattice diffraction profiles of δ-Mn together with Fe, V and Cr. From the derived results we estimate a cubic lattice parameter of $\approx$ 2.985Å for the δ-Mn modification for thin Mn layers, when grown in superlattices at room temperature. The actual value of the tetragonal distortion depends on both the lattice parameter of the adjacent metal and the thickness of the Mn layers. The tetragonal distortions are less than 10% in general, while the V/Mn system shows an almost cubic structure. Both of these results are in contrast to all surface studies of Mn films published before.

Since the transition metals V, Cr and Fe, which we have used in conjunction with Mn, all exhibit unique magnetic behavior in their bulk states (they are Pauli-

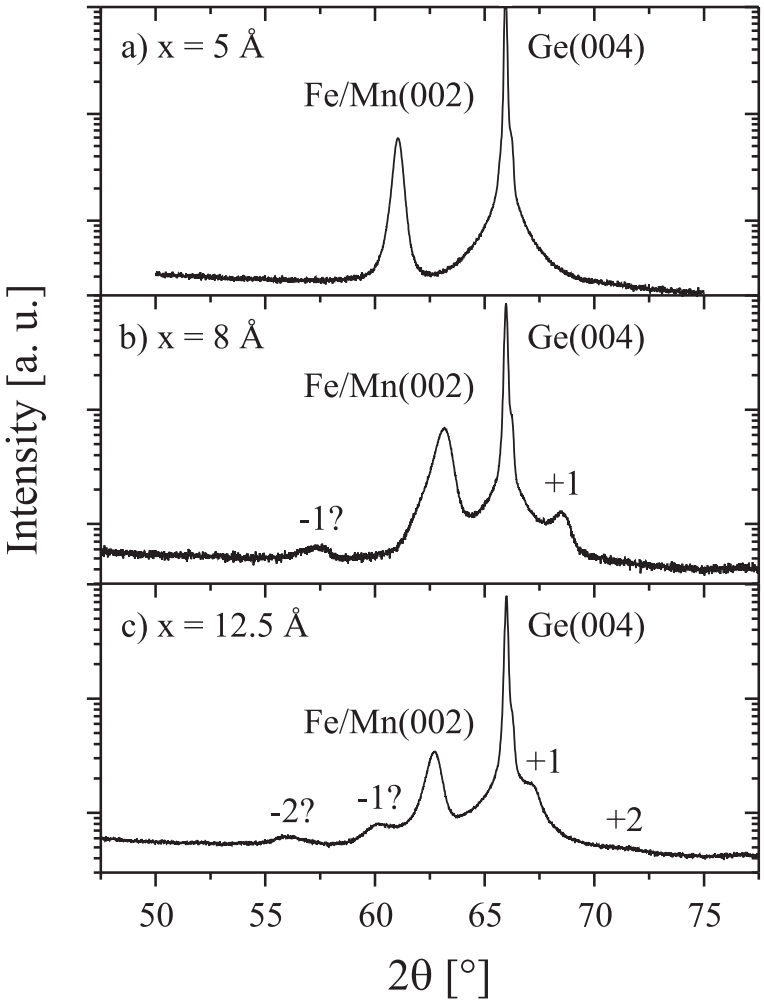

Figure 53. x-ray diffraction patterns of Fe/δ-Mn superlattices. a) [$Fe_{11}Mn_5$], b) [$Fe_{11}Mn_8$], c) [$Fe_{11}Mn_{12.5}$]. The satellites are denoted by their negative or positive orders.

paramagnets, antiferromagnets, and ferromagnets, respectively), we expect that new interesting details concerning the magnetism of the δ-Mn modification could be found. The first results concerning the oscillatory interlayer coupling and giant magnetoresistance have already been observed [1, 60].

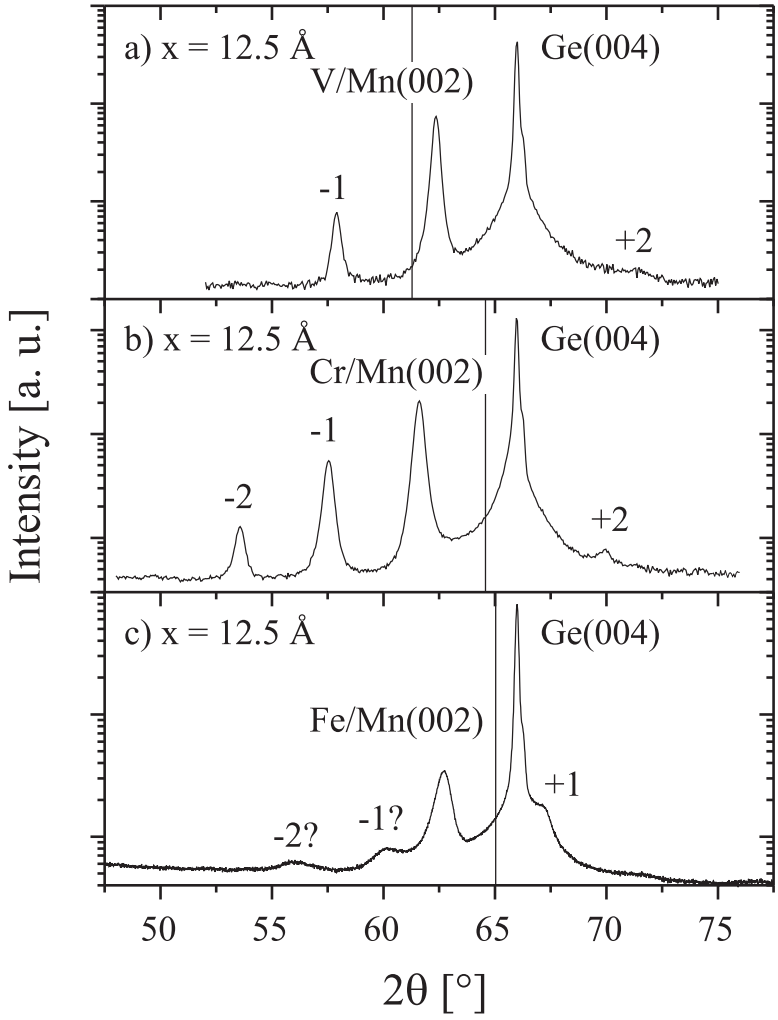

Figure 54. x-ray diffraction patterns of identical M/δ-Mn superlattices (M = V, Cr, Fe). a) $[V_{11}Mn_{12.5}]$, b) $[Cr_{11}Mn_{12.5}]$, c) $[Fe_{11}Mn_{12.5}]$, from figures 49, 50 and 53. The vertical lines indicate values for bulk V, Cr and Fe. The satellites are denoted by their negative or positive orders.

		$[V_{11}Mn_5]$		$[V_{11}Mn_8]$		$[V_{11}Mn_{12.5}]$	
		V	Mn	V	Mn	V	Mn
d	[Å]	1.488	1.476	1.486	1.477	1.490	1.486
σ_d	[Å]	0.01	0.01	0.023	0.02	0.01	0.01
n	[ML]	7.243	3.508	7.245	5.414	7.236	8.221
σ_n	[ML]	0.01	0.01	0.04	0.04	0.01	0.01
δ_1	[Å]	-0.024	0.151	-0.055	0.055	-0.084	0.086
δ_2	[Å]	0.001	-0.106	0.050	-0.050	-0.084	0.086
d_{IF}	[Å]	1.475		1.482		1.488	
σd_{IF}	[Å]	0.045		0.045		0.07	
z		37		30		25	

Table 6. Fitted results for V/δ-Mn-superlattices. n: number of scattering planes in each component of the bilayer, d: lattice spacing, δ_i: maximum distortion of the lattice spacing at the interface, d_{IF}: interface distance, z: number of bilayers, σ_i: standard deviation. α is chosen to be α= 0.55.

		$[Cr_{11}Mn_5]$		$[Cr_{11}Mn_8]$		$[Cr_{11}Mn_{12.5}]$	
		Cr	Mn	Cr	Mn	Cr	Mn
d	[Å]	1.443	1.516	1.445	1.578	1.408	1.595
σ_d	[Å]	0.016	0.00	0.00	0.00	0.00	0.017
n	[ML]	7.558	3.612	8.356	5.254	7.963	8.609
σ_n	[ML]	0.01	0.01	0.00	0.00	0.01	0.01
δ_1	[Å]	0.087	-0.086	0.009	0.038	-0.046	-0.111
δ_2	[Å]	0.032	-0.134	0.015	-0.145	0.083	-0.007
d_{IF}	[Å]	1.458		1.492		1.453	
σd_{IF}	[Å]	0.05		0.08		0.095	
z		25		30		20	

Table 7. Fitted results for Cr/δ-Mn-superlattices. n= number of scattering planes in each component of the bilayer, d= lattice spacing, δ_i= maximum distortion of the lattice spacing at the interface, d_{IF}= interface distance, z= number of bilayers, σ_i= standard deviation. α is chosen to be $\alpha = 0.55$.

10 Ho/Pr alloys

Investigations of the magnetic properties of rare earths have been carried out since the 1950s. The rare earths display a variety of magnetic structures depending upon temperature, pressure and magnetic field. Magnetic structures such as the basal-plane antiferromagnet, helix, cone, longitudinal wave and helifan structures have been identified. With the advent of the well controlled MBE technique, new systems for investigations, such as superlattices and thin film alloys, have been prepared. Thin films often show a deviation from bulk lattice spacings, which is dependent on film thickness. Adjusting the lattice spacing this way is equivalent to applying a pressure. Thin films stabilized in superlattices can therefore be considered as model systems for the pressure dependence of, for example magnetic properties. For rare earth superlattices, the propagation of long range magnetic order over nonmagnetic spacers is of particular interest [82]. For an early review on magnetic rare earth superlattices see [59]. Rare earth binary alloys of composition A_xB_{1-x} have also be employed in magnetic investigations. The composition parameter x can be varied from $x = 1$ which corresponds to the pure element A, to $x = 0$ for material B. Even though the structural and magnetic properties of the materials A and B are well known, intermediate concentrations of x can give rise to new structures. Pure Ho has the hcp crystal structure and a basal plane magnetic spiral structure at temperatures 20K<T<132K. Below 20K the moments tilt out of the plane and form a conical spiral. Pr has a dhcp crystal structure, and orders magnetically at 0.05K [45, p. 353], far below the temperatures relevant to this investigation. HoPr alloys will, if the growth conditions facilitate it, order as a single crystal. The crystal and magnetic structure of the HoPr alloys have been determined by x-ray and by neutron diffraction [30]. Table 8 lists the crystal structure and the Neel temperature of HoPr alloys as well as of pure Ho and Pr.

Composition	Structure	$c/2$ [Å]	T_N [K]
Ho[a]	hcp	2.809	131
$Ho_{80}Pr_{20}$	hcp	2.823	101.04
$Ho_{60}Pr_{40}$	hcp	2.846	64
$Ho_{50}Pr_{50}$	Sm	2.878	39.64
$Ho_{40}Pr_{60}$	Sm	2.882	31.5
Pr[b]	dhcp	2.958	0.05

[a] From a Ho thin film.

[b] Bulk Pr.

Table 8. Properties of pure Ho, Pr and alloys. The lattice parameters are measured at room temperature.

We see that the physical properties of the alloys seem to change with composition in a continuous way. By continuous, we mean that in the case of pure Ho and Pr we observe bulk like properties, whereas the lattice parameters and Neel temperatures of the alloys 'follow' the composition parameters x. For Ho concentrations of 0.5 and 0.4, the alloy has the Sm structure. The Sm structure can be constructed by the following closed-packed stacking sequence 'ABABCBCAC'. For comparison, the fcc structure has a stacking of 'ABC'. Using the notation in the *International tables*, we obtain the following positions of the atoms for the Sm structure: (0,0,0), $(\frac{2}{3},\frac{1}{3},\frac{1}{3})$, $(\frac{1}{3},\frac{2}{3},\frac{2}{3})$, $(0,0,\pm\mu)$, $(\frac{2}{3},\frac{1}{3},\frac{1}{3}\pm\mu)$, $(\frac{1}{3},\frac{2}{3},\frac{2}{3}\pm\mu)$, with

$\mu = 2/9$. Basically, the unit cell has nine equidistantly spaced planes, with a unit cell c-axis of ≈ 26Å.

10.1 X-ray magnetic scattering

Although theoretically realized in 1929, that x-rays scatter from the magnetic moment of electrons, the experimental demonstration was first given in 1972[17]. With the advent of synchrotron radiation the amount of work involving the resonant as well as non-resonant magnetic x-ray scattering has increased dramatically. X-ray magnetic scattering (XRMS) investigations on pure elements with large magnetic moments have already shown the strength of the technique: For holmium this has led to the introduction of spin slips in the magnetic structure [67]. Other examples are studies of magnetic order parameters of single crystals of Dy, Ho, Er and Tm, where the temperature dependence of up to four higher harmonic satellites was measured [38]. Examples of x-ray magnetic scattering studies of rare earth alloys are HoEr [71], DyLu [23] and HoPr [88]. Where neutron scattering has traditionally been the tool for magnetic scattering investigations, x-ray magnetic scattering is getting its foothold. Some of the advantages are: XRMS is element specific, has better resolution, can be performed on strong neutron absorbers, and can, ultimately, yield values for the orbital and spin angular momentum L and S. XRMS will briefly be touched upon here, but the reader is referred to the works of *Lovesey et.al.* [56] and *Blume et.al.* [8] for more details. The main result of the quantum theory of scattering with application to x-ray scattering is that we can now rewrite the atomic form factor $f(q)$, as

$$f = f(\bar{q},\omega) + f^M(\bar{q},\omega) + f^{RM}(\bar{q},\omega) \tag{39}$$

where the first term is the usual form factor plus the anomalous dispersion terms, the second term is the non-resonant magnetic scattering, and

$$f^M(\bar{q},\omega) = \frac{i\hbar}{2mc^2}[\bar{L}(\bar{q})\cdot\bar{A} + 2\bar{S}(\bar{q})\cdot\bar{B}] \tag{40}$$

the third term is the resonant magnetic scattering in the dipole approximation.

$$f^{RM}_{E1}(\bar{q},\omega) = \frac{3}{4\pi q}\{-i(\bar{\epsilon}'\times\bar{\epsilon})\cdot\bar{m}F_1 + (\bar{\epsilon}'\cdot\bar{m})(\bar{\epsilon}\cdot\bar{m})F_2\} \tag{41}$$

The vectors $\bar{A}$ and $\bar{B}$ depend on the polarization of the incident and scattered waves, $\bar{\epsilon}$ and $\bar{\epsilon}'$, as well as on the scattering geometry. The magnetic moment is denoted $\bar{m}$ and the strength of the energy dependent resonances is denoted F_i. In the formula for the resonant magnetic scattering, only the electric dipole transition is included. This transition corresponds to the $2p_{3/2} \rightarrow 5d_{5/2}$ transition for L_{III} edges and $2p_{1/2} \rightarrow 5d_{3/2}$ for L_{II} edges. The first term of equation 41 will contribute to magnetic satellites around the Bragg peaks. The second term will give second order magnetic satellites. For holmium, the second term is smaller than the first by a factor of 20 [29], and 2τ peaks were not observed in these investigations.

Synchrotron radiation, produced by bending magnets and traditional insertion devices, is highly linearly polarized, with the polarization vector in the plane of the ring[18]. Polarization vectors in the plane of the ring, and perpendicular to it, are called σ and π polarization respectively. In a vertical scattering geometry, charge

[17] For reviews see [67] and [55].
[18] At BW2 the polarization is ≈90%.

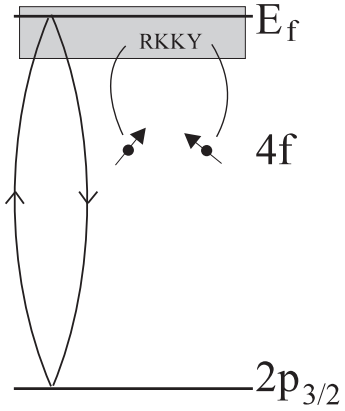

Figure 55. The resonant scattering process at the L_{III} edge: Localized $4f$ moments in the rare earths interact via the RKKY interaction mediated by the conduction electrons. Incident light promotes an electron from the $2p_{3/2}$ level into an empty state in the conduction band. Upon decay back to the $2p_{3/2}$ state, a photon is emitted giving rise to magnetic scattering. The polarization of the emitted photon is thus influenced by the 4f moments via the conduction electrons.

scattering scatters as $\sigma \rightarrow \sigma$. Magnetic scattering from the first term of equation 41 is pure $\sigma \rightarrow \pi$. This means that by applying polarization analysis we can separate charge scattering from magnetic scattering [67]. Polarization analysis is done by diffracting the scattered beam through an angle of approximately 90° by using appropriate analyzer crystals. Graphite (006) and copper (220) reflections give scattering angles of $\approx 90°$ for Ho L_{III} and Pr L_{II} respectively. Although polarization analysis causes the overall intensity to decrease, it does increase the signal to noise ratio.

10.2 Experimental details

The Ho_xPr_{1-x} alloys were grown in the Clarendon Laboratory, Oxford[19], and have been examined at Clarendon Laboratory, Risø and at the physics department at Brookhaven National Laboratory. Neutron and x-ray scattering studies have been performed on the samples. We will here focus on the resonant x-ray magnetic scattering results. The samples were composed as follows: A Nb buffer layer 2000Å thick was grown on a $(11\bar{2}0)$ sapphire substrate to prevent the chemically active rare-earth metals from attacking the substrates, after which a 1000Å Y seed layer was deposited. The 10000Å thick Ho_xPr_{1-x} alloys were then grown on the seed. Finally, the sample was capped with 300Å Y to limit the oxidation of the alloy. Further details about the growth conditions can be found in reference [89].

The samples were mounted in a helium filled Be container, which in turn was mounted in a cryostat. The samples were oriented with the $[00\ell]$ face in a vertical scattering geometry. The experiments were conducted at BW2 in Hamburg and at X22C at Brookhaven National Laboratory.

At the beamlines used in this study, the incident radiation can be tuned in the interval from 5 to 10 keV[20]. The absorption edges of Ho and Pr are listed in table 9, and it is seen that they all lie within the tunable range.

[19] By R C C Ward and M C Wells.
[20] At BW2 energies up to 20keV can be reached by removing the Au mirror.

†	L_I [keV]	L_{II} [keV]	L_{III} [keV]
Ho	9.394	8.918	8.071
Pr	6.835	6.440	5.964

† From [85].

Table 9. Absorption edges for Ho and Pr.

10.3 Results

Figure 56 shows a [00ℓ] scan of $Ho_{0.6}Pr_{0.4}$ alloy taken at the Ho L_{III} edge at a temperature of 10K. The alloy has the hcp structure. In addition to the structural peaks belonging to the alloy, the substrate and the buffer, magnetic peaks around the (002) and (004) reflections of the alloy are clearly seen. In this particular example, the magnetic wavevector $\tau = 2/9$ in reciprocal lattice units. Figure 57 shows a similar scan of the $Ho_{0.5}Pr_{0.5}$ alloy. This alloy has the Sm structure, which has been explained previously. The indexing of the peaks is referring to the Sm structure. The (009) reflection of the Sm structure corresponds to the (002) reflection of the hcp structure which is the basis for the x-axis. The magnetic satellites are, with reference to the hcp unit cell, located around (002) and (004), with $\tau = \frac{1}{3}$. In addition to the magnetic and structural peaks from the alloy, we also see peaks from the substrate, buffer and cap layer. The dynamical range of the two longitudinal scans is rather impressive, nearly nine orders of magnitude. To achieve this, the diffraction profiles are pieced together of many scans, each with the attenuation of the beam set to match the dynamical range of the detector. The widths of the (002) peaks in the longitudinal direction, give estimates of the structural coherence lengths of ≈700Å for $Ho_{0.6}Pr_{0.4}$ and ≈1600Å for $Ho_{0.5}Pr_{0.5}$. The magnetic coherence lengths, obtained from the width of the (002-τ) peaks, are approximately the same as the structural coherence lengths.

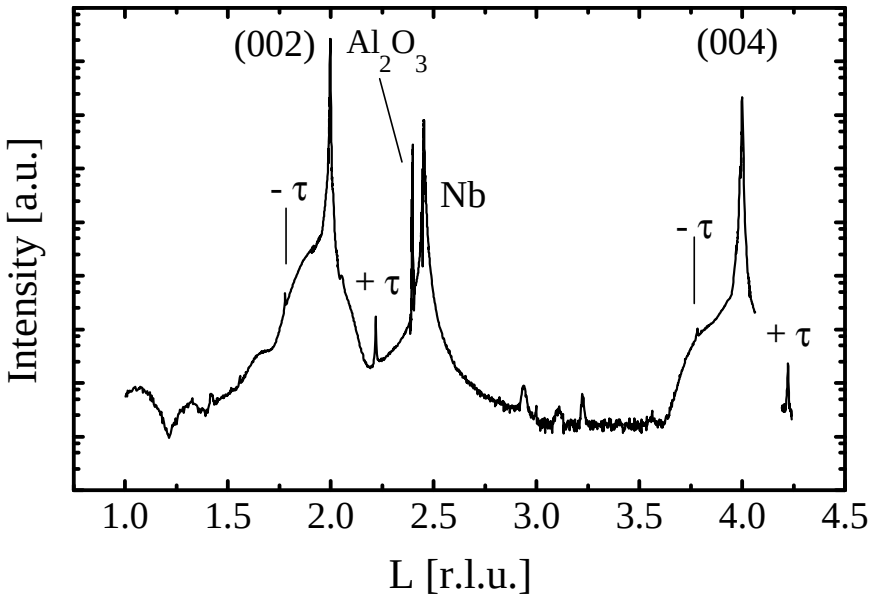

Figure 56. [00ℓ] scan on the $Ho_{0.6}Pr_{0.4}$ alloy taken at the Ho L_{III} edge and T=10K. The HoPr (002) and (004) reflections fall at 2 and 4 r.l.u. respectively. The sapphire substrate (11$\bar{2}$0) reflection and the (220) reflection of the Nb buffer are also seen. The magnetic satellites are located at (002±τ) and (004±τ) with $\tau = 2/9$. The broad peak at ≈1 r.l.u. and the peaks around 3 r.l.u. have not been identified.

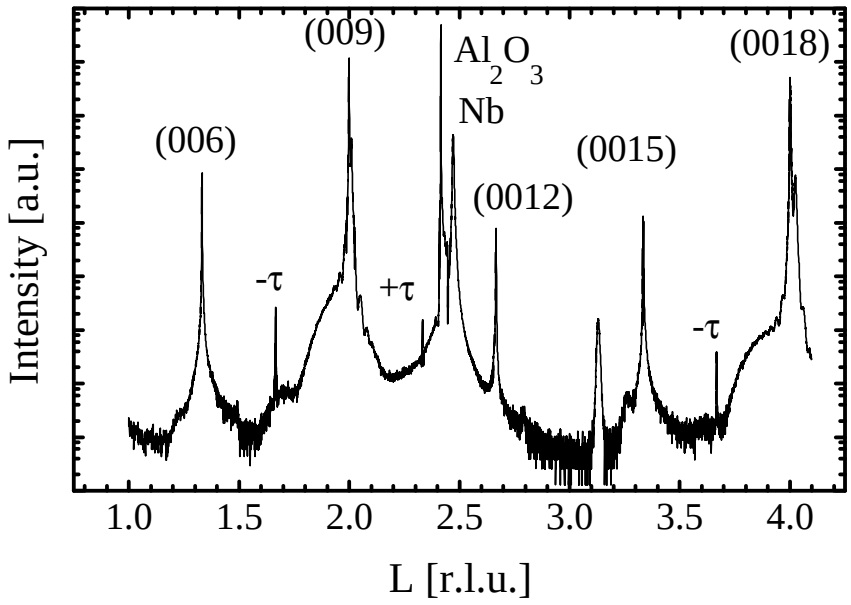

Figure 57. [00ℓ] scan on the $Ho_{0.5}Pr_{0.5}$ alloy taken at the Ho L_{III} edge and T=10K. The reflections are labeled after the Sm-like unit cell where $c = 25.9$Å. The x-axis is in r.l.u. of the hexagonal unit cell with $c = 5.76$Å, so the (009) reflection occurs at 2 r.l.u.. Again we see peaks arising from the sapphire substrate and the Nb buffer layer, and a peak from the Y cap layer is just resolved to the right of the (0018) peak. Magnetic satellites are located at (009$\pm\tau$) and (0018$-\tau$) with $\tau = 1/3$. The origin of the peak at 3.13 r.l.u. is not known.

In order to investigate whether the magnetic moments from Ho could induce a moment on Pr, resonant scattering was performed on the magnetic (002-τ) satellite at the L_{III} and L_{II} edges of Ho and Pr. Figure 58 shows the results of the energy scans. The resonance enhancement of the magnetic peaks is clear, although for Pr L_{III} the enhancement is very small indeed. The data were taken with a Ge(111) analyzer crystal in order to facilitate comparison of the intensities. The count rates are of the order of tens to hundreds of counts per seconds. The widths of the peaks are about 10eV and are the result of the true widths of the electronic transitions convoluted with the energy resolution of the monochromator. One of the main results of the energy scans on the magnetic satellite is that the ratio $\frac{IL_{III}}{IL_{II}}$ of the integrated intensities at the two absorption edges are fundamentally different for Ho and Pr. In the former case, the ratio is ≈ 10 and in the latter case, ≈ 0.1, which is in discrepancy with the simplest theories predicting the ratio to be unity for both edges [35].

In order to further investigate the magnetic peaks at (002$-\tau$) a series of longitudinal scans was performed at different temperatures. The measurement of intensities of magnetic peaks as a function of temperature is well known from neutron scattering [18]. Resonant x-ray magnetic scattering offers the further possibility of comparison of these 'temperature' scans at energies corresponding to the absorption edges of the elements in the alloys. Figure 59 shows the result of one such series of scans for the $Ho_{0.5}Pr_{0.5}$ alloy. The data are taken at the Ho L_{III} edge and the at the Pr L_{II} edge because here we obtain the highest resonant intensities. In order to suppress the effect of charge scattering, we employed polarization analysis selecting ($\sigma \rightarrow \pi$) magnetic scattering only. The data are fitted with a simple expression $A(T_N - T)^{2\beta}$, where T_N is found by linear fits to the data close to the transition temperature. The Neel temperature is found to be ≈ 40K, and the exponent $\beta \approx 0.5$. Table 8 lists the Neel temperatures for the

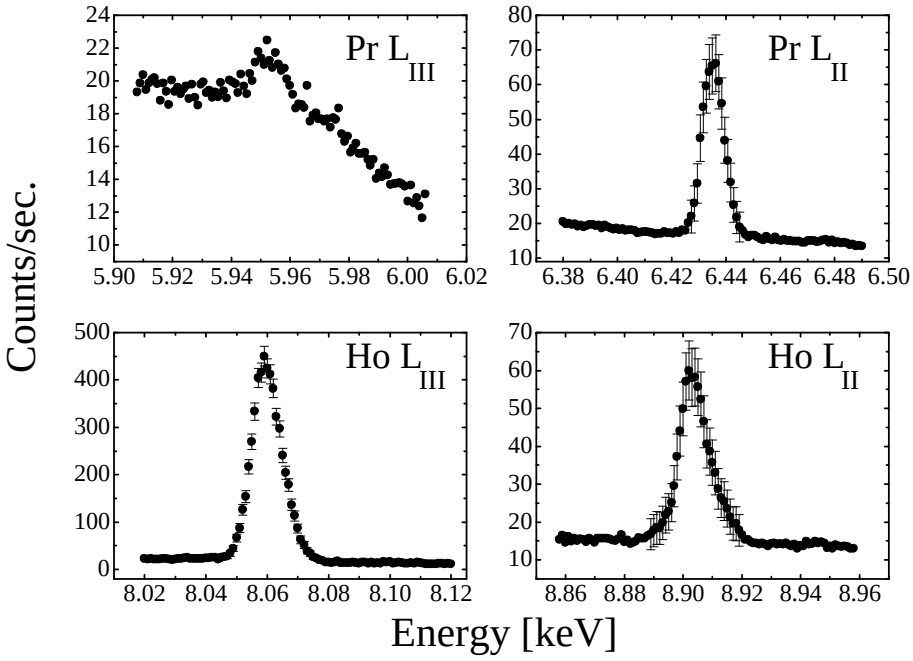

Figure 58. Energy scans on the $(002-\tau)$ peak of the $Ho_{0.5}Pr_{0.5}$ alloy at Ho and Pr L_{II} and L_{III} edges. Error bars are left out on the top-left figure for clarity.

alloys. These are in agreement with results obtained by neutron scattering on the $Ho_{0.6}Pr_{0.4}$ alloy [30].

There are rather large errors on the critical parameters obtained. This is mainly due to the low counting rates near the Neel temperature. Therefore, we do not attempt to extract quantitative information from these measurements. Nevertheless, we conclude that the two scans appear to be very similar.

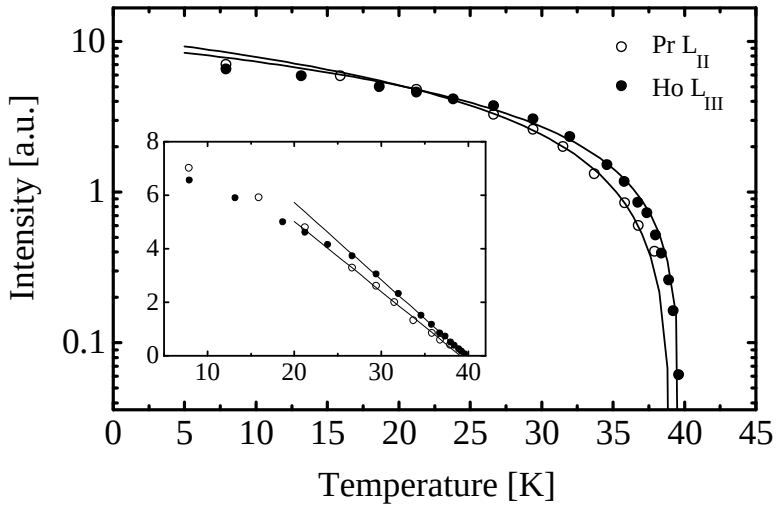

Figure 59. Temperature dependence of the magnetic satellite of the $Ho_{0.5}Pr_{0.5}$ alloy at the Ho L_{III} and Pr L_{II} edges. The data points are integrated intensities of the (002-τ) peak. Inset shows the data on a linear scale with the linear fit used to obtain T_N.

10.4 Summary

Structural and magnetic investigations have been performed on Ho_xPr_{1-x} alloys using resonant scattering techniques. The investigations included structural and magnetic analysis with Ge(111) analyzer crystals as well as polarization analysis with copper and graphite crystals. The analysis is in agreement with neutron scattering experiments. In addition, resonant enhancement of the magnetic peaks at the Pr edges indicates that Pr possesses an induced magnetic moment originating from the Ho. The analysis shows that the temperature dependence of the magnetic peaks appears to be identical at the two absorption edges. With the formulae for resonant x-ray scattering, there is the ultimate possibility of measuring the individual magnetic moments of, for example, Ho and Pr in alloys. Attempts have already been made to extract this information [23], but at the moment the branching ratio problem seems to prevent the reliable extraction of such information. Recently, new theoretical results have taken us one step further in the understanding of the branching ratios [86]. X-ray scattering may therefore, in the future, be able to contribute to the knowledge of electronic states of the rare earths. Finally, the experiments show the necessity of bright and tunable x-ray sources for the success of such studies.

11 Conclusion

Several MBE thin film and superlattice systems have been investigated during the course of this work. The investigations include growth of thin films and superlattices as well as structural and magnetic characterization. The structural characterization has been done mainly by x-ray diffraction, but neutron scattering experiments have also been performed. In the following, we will list the main results of the analysis for each investigation.

Fe/V superlattices have been grown by MBE. The optimal growth temperature of this systems is estimated to be 600K. The superlattices are of high structural quality (for metal superlattices) with coherence lengths of up to 450Å. Modelling of the diffraction profiles produces good fits and a detailed knowledge of the structural parameters for selected superlattices. For the Fe/V superlattices, comparisons are made between x-ray and neutron diffraction, for both high angle and reflectivity scans. Furthermore, the tunability of synchrotron radiation is utilized in order to enhance the superlattice diffraction profiles.

A series of Cr/Mn superlattices grown on Ge and MgO substrates has been subject to structural investigations. The Cr layers are of fixed thickness and the Mn layers vary from 10Å to 30Å. Both longitudinal scans and in-plane scans are performed. Good fits to the diffraction profiles are produced and the structural properties are presented. A method for simulating disorder in one component of the superlattice is demonstrated. The analysis shows that disorder develops with Mn thickness, which is consistent with our understanding of the allotropy of Mn.

Comparison is made between three superlattice systems: Fe/Mn, Cr/Mn and V/Mn. Again Cr has a fixed thickness (11Å), and Mn thicknesses of 5Å, 8Å and 12.5Å are investigated. These 'thin' superlattices are modelled, and in the case of V/Mn and Cr/Mn the structural parameters are presented. The Fe/Mn superlattices could not be fitted with the current model. We find longitudinal lattice parameters for Mn of up to 3.06Å and 3.13Å for V/Mn and Cr/Mn respectively. We estimate a cubic lattice parameter for Mn of 2.985Å. It is shown that the appearance of the diffraction profiles are quite different for the three systems. For Cr/Mn tetragonal distortions of Mn of 10% are seen, whereas for V/Mn the Mn is nearly cubic.

The results from an x-ray magnetic scattering experiment on HoPr alloys are presented. The $Ho_{0.5}Pr_{0.5}$ alloys has the Sm structure and the $Ho_{0.6}Pr_{0.4}$ alloy has the hcp structure. The magnetic (002-τ) satellites are investigated by means of resonant enhancement, by tuning the x-ray energy to the L_{II} and L_{III} edges for Ho and Pr. The temperature dependence of the magnetic peaks is measured for Pr L_{II} and Ho L_{III} respectively. A resonance enhancement is seen at the Pr L_{II} edge which is taken as an indication of the Pr possessing an induced magnetic moment. It has not been possible to estimate the magnitude of the moment.

Acknowledgments

I am indebted to Dr. Jörg Pohl from the University of Konstanz for generously sharing his samples and data with me. Without his help this thesis would appear very slim. Despite the distance from Copenhagen to Konstanz, the communication has always worked, and it has been a pleasure to work with him. Many thanks goes to John G. Larsen for his beautiful drawings, some of which are included in this work. Many warm thanks are extended to the GNU projects and the Free Software Foundation, by whose aid, contact with Bills programs have been minimized. The authors of SUPREX are greatfully acknowledged for their distribution of the program.

I would like to thank Ole Stender Nielsen for his many grammatical corrections and general comments. Steen Aa. Sørensen has provided me with an excellent limousine service throughout the final months of this work - a bottle of port is in the mail.

Finally I would like to acknowledge The Danish Research Academy and Risø for funding, my supervisor Robert Feidenhans'l for accepting my eight months leave to try 'real' work and i-data for granting me leave to finish the thesis.

References

[1] M. Albrecht, J. Pohl, E. U. Malang, J. Köhler, H. Wider, and E. Bucher. Magnetic properties of Fe/bct Mn superlattices grown by molecular beam epitaxy. *J. Magn. and Magn. Mat.*, 5:169, 1997.

[2] J. Ambrose Wolf. Structurelle gesichtspunkte der magnetischen wischenschichtkopplung im Fe/Cr/Fe-system. Technical report, Forschungszentrum Jülich GmbH, 1993.

[3] M. D. Antonik and R. J. Lad. Faceting, reconstruction, and defect microstructure at ceramic surfaces revealed by atomic force miscroscopy. *J. Vac. Sci. Technol. A*, 10(4):669, 1992.

[4] N. W. Ashcroft and N. D. Mermin. *Solid State Physics.* cbs publishing asia ltd., 1976.

[5] M. N. Baibich, J. M. Broto, A. Fert, F. Nguyen Van Dau, F. Petroff, P. Etienne, G. Creuzet, A. Friederich, and J. Chazelas. Giant magnetoresistance of (001)Fe/(001)Cr magnetic superlattices. *Phys. Rev. Lett.*, 61(21):2472–2475, 1988.

[6] L. H. Bennet and R. E. Watson, editors. *Magnetic Multilayers.* World Scientific, 1994.

[7] G. Binasch, P. Grünberg, F. Saurenbach, and W. Zinn. Enhanced magnetoresistance in layered magnetic structures with antiferromagnetic interlayer exchange. *Phys. Rev. B*, 39(7):4828–4830, 1989.

[8] M. Blume and D. Gibbs. Polarization dependence of magnetic x-ray scattering. *Phys. Rev. B*, 37(4):1779–1789, 1988.

[9] M. Born and E. Wolf. *Principles of optics.* Pergamon Press, Oxford, 1980.

[10] B. H. Bransden and C. J. Joachain. *Physics of atoms and molecules*. Longman Scientific & Technical, 1994.

[11] A. Brazdeikis. *Molecular beam epitaxy and properties of Bi-based superconducting cuprates*. PhD thesis, Kungl. Tekniska Högskolan, 1994.

[12] J. C. P. Chang, T. P. Chin, K. L. Kavanagh, and C. W. Tu. High-resolution x-ray diffraction of InAlAs/InP superlattices grown by gas source molecular epitaxy. *Appl. Phys. Lett.*, 58(14):1530–1532, 1991.

[13] K. K. Choi, M. Dutta, R. P. Moerkirk, C. H. Kuan, and G. J. Iafrate. Application of superlattice bandpass filters in 10μm infrared detection. *Appl. Phys. Lett.*, 58(14), 1991.

[14] M. J. Christensen and J. Pohl. In-plane scattering studies. Private communication, 1995.

[15] M.J. Christensen, R. Feidenhans'l, and M. Nielsen. Fe/V superlattices: X-ray and neutron-scattering investigations. *Vacuum*, 46(8-10):1113–1115, 1995.

[16] R. Coehoorn. Relation between interfacial magnetism and spin-dependent scattering at non-ideal Fe/Cr and Fe/V interfaces. *J. Magn. and Magn. Mat.*, 151:341–353, 1995.

[17] J. B. Cohen and J. E. Hilliard, editors. *Local Atomic Arrangement studied by X-Ray Diffraction*, volume 36. Gordon and Breach Science publishers, 1965.

[18] Malcom F. Collins. *Magnetic critical scattering*. Oxford university press, 1989.

[19] L. E. Davis, N. C. MacDonald, P. W. Palmberg, G. E. Riach, and R. E. Weber. *Handbook of auger electron spectroscopy*. Physical Electronics Industries, Inc., 2 edition, 1976.

[20] W. Drube, H. Schulte-Schrepping, R. Schmidt, and Materlik G. Design and performance of the high-flux/high-brightness x-ray wiggler beamline BW2 at HASYLAB. *Rev. Sci. Instrum.*, 66(2):1668, 1995.

[21] J. DuMond and P. Youtz. An x-ray method of determining rates of diffusion in the solid state. *J. Appl. Phys.*, 11, May 1940.

[22] Y. Endoh, K. Kawaguchi, N. Hosoito, T. Shinjo, T. Takada, Y. Fujii, and T. Ohnishi. Structure modulation of Fe-V artificial superstructure films. *J. Phys. Soc. Jap.*, 53(10):3481–3487, 1984.

[23] B. A. Everitt, M. B. Salomon, B. J. Park, C. P. Flynn, T. Thurston, and Doon Gibbs. X-ray magnetic scattering from nonmagnetic Lu in a Dy/Lu alloy. *Phys. Rev. Lett.*, 75:3182, 1995.

[24] L. M. Falicov, Daniel T. Pierce, S. D. Bader, R. Gronsky, Kristl B. Hathaway, Herbert J. Hopster, David N. Lambeth, S. S. P. Parkin, Gary Prinz, Myron Salamon, Ivan K. Schuller, and R. H. Victora. Surface, interface and thin-film magnetism. *J. Mater. Res.*, 5(6):1299–1340, 1990.

[25] R. Feidenhans'l. *Surface structure determination by X-ray diffraction*. Surface Science reports. North-Holland-Amsterdam, 1989.

[26] C. P. Flynn. Constraints on the growth of metallic superlattices. *J. Phys. F*, 18:L195, 1988.

[27] E. Fullerton, I. K. Schuller, H. Vanderstraeten, and Y. Bruynseraede. Structural refinement of superlattices from x-ray diffraction. *Phys. Rev. B*, 45(16):9292–9310, 1992.

[28] R. A. Gibaud, A. andCowley, D. F. McMorrow, R. C. C. Ward, and M. R. Wells. High-resolution x-ray scattering study of the structure of niobium thin films on sapphire. *Phys. Rev. B*, 48(19):14463, 1993.

[29] Doon Gibbs, D: R. Harshman, E. D. Isaacs, D. B. McWhan, D. Mills, and C. Vettier. Polarization and resonance properties of magnetic x-ray scattering in holmium. *Phys. Rev. Lett.*, 61(10):1241–1244, 1988.

[30] J. P. Goff, C. Bryn-Jacobsen, D. F. McMorrow, J. Jensen, G. J. McIntyre, J. A. Simpson, R. A. Cowley, R. C. C. Ward, and M. R. Wells. The interplay between structure and magnetism in Ho_xPr_{1-x} alloys I: neutron scattering. *In preparation*, 1997.

[31] P. Granberg, P. Isberg, B. Hjörvarsson, P. Nordblad, and R. Wäppling. To be submitted. *J. Magn. and Magn. Mat.*, 1997.

[32] A. Guinier. *X-ray diffraction in crystals, Imperfect Crystals, and Amorphous Bodies*. W. H. Freeman and Company, 1963.

[33] F. Hajdu. Revised parameters of the analytic fits for coherent and incoherent scattered x-ray intensities of the first 36 atoms. *Acta Cryst.*, A28:250, 1972.

[34] N. Hamada, K. Terakura, and A. Yanase. Distribution of magnetic moments near the Fe-V interface: band-structure calculation and local-environment effect. *J. Phys. F: Met. Phys.*, 14:2371–2378, 1984.

[35] J. P. Hannon, G. T. Trammell, M. Blume, and Doon Gibbs. X-ray resonance exchange scattering. *Phys. Rev. Lett.*, 61(10):1245–1248, 1988.

[36] G.R. Harp, S.S.P. Parkin, W.L. O'Brien, and B.P. Tonner. X-ray magnetic-circular -dichroism study of Fe/V multilayers. *Phys. Rev. B*, 51(5):3293, 1995.

[37] J. R. Heffelfinger, M. W. Bench, and C. Barry Carter. On the faceting of ceramic surfaces. *Surface Science*, 343:L1161–L1166, 1995.

[38] G. Helgesen, J. P. Hill, T. R. Thurston, and Doon Gibbs. X-ray scattering study of higher harmonic satellites near the antiferromagnetic phase transitions in rare-earth metals. *Phys. Rev. B*, 52(13):9446–9454, 1995.

[39] J. E. Hilliard. Artificial layer structures and their properties. In J. M. Cowley, J. B. Cohen, M. B. Salamon, and B. J. Wuensch, editors, *Modulated Structures*, 1979.

[40] B. Hjörvarsson, J. A. Dura, P. Isberg, T. Watanabe, T. J. Udovic, G. Andersson, and C. F. Majkrzak. Reversible tuning of the magnetic exchange coupling in Fe/V (001) superlattices using hydrogen, submitted to. *Phys. Rev. Lett.*, 1997.

[41] N. Hosoito, K. Kawaguchi, T. Shinjo, T. Takada, and Y. Endoh. Magnetic properties of Fe-V multilayered films with artificial superstructures. *J. Phys. Soc. Jap.*, 53(8):2659–2667, 1984.

[42] P. Isberg. *Preparation and properties of Fe/V superlattices*. PhD thesis, Uppsala University, 1997.

[43] P. Isberg, B. Hjörvarsson, R. Wäppling, E. B. Svedberg, and L. Hultman. Growth of epitaxial Fe/V(001) superlattice films. *Vacuum*, 48:483, 1997.

[44] R. W. James. *The optical principles of the diffraction of X-rays*. Bell, 1962.

[45] J. Jensen and A. R. Mackintosh. *Rare Earth Magnetism*. Clarendon Press, Oxford, 1991.

[46] M. Kolář, B. Iochum, and L. Raymond. Structure factor of 1D systems (superlattices) based on two-letter substitution rules: I. δ (Bragg) peaks. *J. Phys. A: Math. Gen.*, 26:7343–7366, 1993.

[47] P. Koorevaar, Y. Suzuki, R. Coehoorn, and J. Aarts. Decoupling of superconducting V by ultrathin Fe layers inV/Fe multilayers. *Phys. Rev. B*, 49(1):441–449, 1994.

[48] J. G. Larsen. Metalliske supergitre - fremstilling og karakterisering. Master's thesis, Risø National Laboratory, 1995.

[49] B. Lebech and L. S. Petersen. *Neutron scattering facilities at the research reactor DR3*. Risø, Denmark, 1990.

[50] B. Lengeler. X-ray absorbtion and reflection in material sciences. *Advances in solid state physics*, 29:53–73, 1989.

[51] B. Lewis and J. C. Anderson. *Nucleation and growth of thin films*. Academic Press, New York, 1978.

[52] Leybold. *Thin film thickness and rate monitor manual*, 1988.

[53] J.-P. Locquet, D. Neerinck, L. Stockman, Y. Bruynseraede, and I. K. Schuller. Long-range order and lattice mismatch in metallic superlattices. *Phys. Rev. B*, 38(2):3572–3575, 1988.

[54] J.-P. Locquet, D. Neerinck, L. Stockman, Y. Bruynseraede, and I. K. Schuller. Discrete and continuous disorder in superlattices. *Phys. Rev. B*, 39(18):13338–13342, 1989.

[55] S. W. Lovesey. Magnetic photon scattering. *J. Phys. C: Solid State Phys.*, 20:5625–5639, 1987.

[56] S. W. Lovesey and S. P. Collins. *X-ray scattering and absorbtion by magnetic materials*. Oxford university press, 1996.

[57] Z. H. Lu, D. J. Lockwood, and J.-M. Baribeau. . *Nature*, 378:258, 1995.

[58] J. E. Mahan, K. M. Geib, G. Y. Robinson, and R. G. Long. A review of the geometrical fundamentals of reflection high-energy electron diffraction with application to silicon surfaces. *J. Vac. Sci. Technol. A*, 8(5):3692–3700, 1990.

[59] C. F. Majkrzak, J. Kwo, M. Hong, Y. Yafet, Doon Gibbs, C. L. Chien, and J. Bohr. Magnetic rare earth superlattices. *Advances in Physics*, 40(2):99–189, 1991.

[60] E. U. Malang. *Unknown title*. PhD thesis, Universität Konstanz, 1996.

[61] P.M. Marcus and V.L. Moruzzi. Magnetism of metastable phases: Band theory and epitaxy. *JAP*, 63(8):4045, 1988.

[62] J. W. Matthews, editor. *Epitaxial growth*, volume A. Academic Press, New York, 1975.

[63] J. E. Mattson, E. E. Fullerton, C. H. Sowers, and S. D. Bader. . *J. Vac. Sci. Technol. A*, 13:276, 1995.

[64] J. G. Miller and D. I. Bolef. Acoustic wave analysis of the operation of quartz-crystal film-thickness monitors. *J. Appl. Phys.*, 39(11):5815–5816, 1968.

[65] J. G. Miller and D. I. Bolef. Sensitivity enhancement by the use of acoustic resonators in cw ultrasonic spectroscopy. *J. Appl. Phys.*, 39(10):4589–4593, 1968.

[66] Z. Mitura and Mikolajczak P. Computer simulation of x-ray spectra of metallic superlattices. *J. Phys. F: Met. Phys.*, 18:183–195, 1988.

[67] D. E. Moncton, D. Gibbs, and J. Bohr. Magnetic x-ray scattering with synchrotron radiation. In *Nuclear Instruments and Methods in Physics Research*, volume A246, pages 839–844. North-Holland (Amsterdam), 1986.

[68] G. Müller, P. Středa, D. Weiss, K. von Klitzing, and G. Weimann. Giant magnetoresistance in lateral surface superlattices. *Phys. Rev. B*, 50(12):8938–8941, 1994.

[69] H. Nakamatsu, A. Sudo, and S. Kawai. ICISS observation of MgO(100) surfaces with vacancies. *Surf. Sci.*, 223:193–200, 1989.

[70] S. S. P. Parkin. . *Phys. Rev. Lett.*, 67:3598, 1991.

[71] D. B. Pengra, N. B. Thoft, M. Wulff, R. Feidenhans'l, and J. Bohr. Resonance-enhanced magnetic x-ray diffraction from a rare-earth alloy. *J. Phys. C*, 6:2409–2422, 1994.

[72] J. Pohl. *Metastabile Phasen in der Metallepitaxie*. PhD thesis, Universität Konstanz, September 1995.

[73] J. Pohl, E.U. Malang, J. Köhler, and E. Bucher. Growth, structural characterization, and stability of thin Cr/δ-Mn(001) superlattices. *J. Vac. Sci. Technol. A*, 13(2), 1995.

[74] J. Pohl, E.U. Malang, B. Scheele, J. Köhler, M. Ch. Lux-Steiner, and E. Bucher. Structure of Fe/δ-Mn superlattices grown by molecular beam epitaxy. *J. Vac. Sci. Technol. B*, 12(6), 1994.

[75] P.M. Reimer, H. Zabel, C.P. Flynn, and J.A. Dura. Extraordinary alignment of Nb films with sapphire and the effects of added hydrogen. *Phys. Rev. B*, 45(19):11426, 1992.

[76] F. Reniers, L. P. Delplancke, A. Asskali, V. Rooryck, and O. VanSinay. Glow discharge sputtering deposition of thin films of Ag, Cr, Cu, Ni, Pd, Rh and their binary alloys onto NaCl and MgO experimental parameters and epitaxy. *Applied Surface Science*, 92:35–42, 1996.

[77] I. K. Schuller. New class of layered materials. *Phys. Rev. Lett.*, 44:1597, 1980.

[78] W. Sevenhans, M. Gijs, Y. Bruynseraede, H. Homma, and I. K. Schuller. Cumulative disorder and x-ray line broadening in multilayers. *Rap. Comm.-Phys. Rev. B*, 34:5955, 1986.

[79] J. Smiths. Magnetic multilayers. *Physics World*, 1992.

[80] F. Stillesjö, B. Hjörvarsson, and B. Rodmacq. Studies of interdiffusion and alloy formation in Fe/V multilayers using hydrogen as a local probe. *J. Magn. and Magn. Mat.*, 126:102–104, 1993.

[81] Y. Suzuki, H. Kikuchi, and N. Koshizuka. Observation of RHEED intensity oscillation in the growth of Ag on Ag(100) single crystals. *Jap. J. Appl. Phys.*, 27(7):1175, 1988.

[82] P. P. Swaddling, R. A. Cowley, R. C. C. Ward, M. R. Wells, and D. F. McMorrow. Magnetic structures of holmium-lutetium alloys and superlattices. *Phys. Rev. B*, 53(10):6488–6498, 1996.

[83] M. A. Tomaz, W. J. Antel Jr, W. L. O'Brien, and G. R. Harp. Induced V moments in Fe/V(100), (211) and (110) superlattices studied using x-ray magnetic circular dichroism. *J. Phys. C*, 9:L179–L184, 1997.

[84] T. Tsakalakos. Mechanical properties and diffusion of metallic superlattices. *J. Vac. Sci. Technol. B*, 4(6):1447–1457, 1986.

[85] D. Vaughan. X-ray data booklet. Lawrence Berkley Laboratory, 1986.

[86] Michel van Veenendaal, J. B. Goedkoop, and B. T. Thole. Branching ratios of the circular dichroism at rare earth L_{23} edges. *Phys. Rev. Lett.*, 78(6):1162–1165, 1997.

[87] A. Vega, A. Rubio, L. C. Balbas, Dorantes-Davila J., S. Bouarab, C. Demangeat, A. Mokrani, and H. Dreyssé. Antiferromagnetic interlayer coupling in Fe/V and Fe/Cr. *J. Appl. Phys.*, 69(8):4544–4546, 1991.

[88] A. Vigliante, M. J. Christensen, J. P. Hill, G. Helgesen, S. Aa. Sørensen, D. F. McMorrow, Doon Gibbs, R. C. C. Ward, and M. R. Wells. Interplay between structure and magnetism in HoPr alloys II: a resonant x-ray magnetic scattering study. *In preparation*, 1997.

[89] R. C. C. Ward, M. R. Wells, C. Bryn-Jacobsen, R. A. Cowley, J. P. Goff, D. F. McMorrow, and J. A. Simpson. MBE growth and characterization of light rare-earth superlattices. *Thin Solid Films*, 275:137–139, 1996.

[90] B. E. Warren. *X-ray diffraction*. Dover Publications, Inc., 1990.

[91] G. L. Weissler and R. W. Carlson, editors. *Vacuum Physics and Technology*, volume 14. Academic Press, 1979.

[92] A. J. C. Wilson, editor. *International tables for crystallography*, volume C. Kluwer Academic Publishers, Dordrecht, 1992.

[93] H. K. Wong, B. Y. Jin, H. Q. Yang, J. B. Ketterson, and J. E. Hilliard. Superconducting properties of V/Fe superlattices. *J. Low Temp. Phys.*, 63(3–4), 1986.

[94] D. P. Woodruff and T. A. Delchar. *Modern techniques of surface science*. Cambridge solid state science series. Cambridge University Press, 1986.

[95] R. W. G. Wyckoff. *Crystal Structures*, volume 1. Interscience Publishers, 2 edition, 1963.

[96] S. Zhang, P. M. Levy, and A. Fert. Conductivity and magnetoresistance of magnetic multilayered structures. *Phys. Rev. B*, 45(15):8689, 1992.

Symbol tables

Symbol	Meaning
μ_0	Permeability of vacuum
h	Planck's constant
$\hbar$	Planck's constant divided by 2π
m	Electron mass
c	Velocity of light in vacuum
e	Elementary charge

Table 10. Fundamental symbols.

Symbol	Meaning
α_i	Incident angle of radiation
α_f	Exit angle of radiation
ω	Sample rotation
θ	Detector rotation
χ	Cradle rotation
q	Magnitude of the momentum transfer
$\bar{q}$	Momentum transfer vector
$\bar{k}$,$\bar{k}_i$	Incident wavevector
$\bar{k}'$,$\bar{k}_f$	Scattered wavevector
$\bar{\varepsilon}$	Polarization of incident radiation
$\bar{\varepsilon}'$	Polarization of scattered radiation
a, b, c	Lattice parameters
h, k, l	Miller indices
d_{hkl}	Interplanar distance
τ_{hkl}	$2\pi/d_{hkl}$

Table 11. Geometrical symbols from scattering geometries and spectrometry.

Symbol	Meaning
$\bar{m}$	Magnetic moment vector
$\bar{L}$	Total angular momentum
$\bar{S}$	Total spin
τ	Magnetic momentum transfer
ω	Angular frequency
M	Molar mass

Table 12. Other symbols.

Abbreviations

In order to avoid referencing to an explanation whenever a new acronym is introduced a list of frequently acronyms is provided. Wherever an explanation is appropriate the acronym may also be explained in the text.

AES	Auger Electron Spectroscopy
AFM	Atomic Force Microscopy
bcc	Body Centered Cubic
BNL	Brookhaven National Laboratory
CCD	Charge Coupled Device
DRI	Dansk Rumforsknings Institut
fcc	Face Centered Cubic
FWHM	Full Width at Half Maximum
HASYLAB	HAmburgerSYnchrotronstrahlungsLABor
hcp	Hexagonal close packed
LEED	Low Energy Electron Diffraction
LUCS	Layered Ultrathin Coherent Structure
MBE	Molecular Beam Epitaxy
ML	MonoLayers
NSLS	National Synchrotron Light Source
QMS	Quadrupole Mass Spectroscopy
RHEED	Reflection High Energy Electron Diffraction
RT	Room Temperature
SL	SuperLattice
STM	Scanning Tunneling Microscopy
SUPREX	SUPerlattice REfinement from X-rays
TEM	Transmission Electron Microscopy
UHV	Ultra High Vacuum
XRD	X-Ray Diffraction
XRMS	X-Ray Magnetic Scattering

Thin film table

This is a listing of the thin films and superlattices that has been produced at Risø and at Konstanz. A few of the mentioned films has not been subject to investigation as for example films grown on NaCl since RHEED showed that the film wasn't of sufficiently high quality to warrant further investigations. Many of these samples has been grown by the MBE group at University of Konstanz.

Table 13. Samples grown at Risø: Film ID, description, substrate, bi-layer repeats (if a superlattice), growth temperature and the person responsible for the film production.

Film	Description	substrate	repeats	T_g [°C]	responsible
MBE105	Ag(50)/Au(30)	MgO	50	185	MJC
MBE106	Fe(20)/V(30)	MgO	20	363	MJC
MBE109	Fe(30)/V(9)	MgO	20	400	MJC
MBE111	Fe(20)/V(6)	MgO	20	406	MJC
MBE112	MBE problems	MgO			MJC
MBE113	MBE problems	MgO			MJC
MBE114	Mgo/Fe/MgO	MgO		200	MJC
MBE115	Fe(20)/Au(8)	MgO	20	200	MJC
MBE116	Fe(30)/V(9)	MgO	20	405	MJC
MBE117	Fe(30)/V(9)	MgO	20	473	MJC
MBE118	Fe(30)/V(9)	MgO	20	540	MJC
MBE119	Au(1000)	Mica		79	MJC
MBE120	Au(25)/Fe(396)	NaCl		90	MJC
MBE121	Fe(x)	NaCl		250	MJC
MBE122	Au(300)	NaCl		300	MJC
MBE123	Nb(287)	Al_2O_3		800	MJC
MBE138	Fe(30)/V(12)	MgO	20	60	MJC
MBE141	MBE problems	MgO			MJC
MBE144	Cu(20)/Ag(20)	MgO	20	120	JL
MBE148	Au(23)/Cr(20)	MgO	23	330	JL
MBE151	Cr(10)/Au(20)	MgO	16	RT	JL
AM001	Fe(30)/V(9)	MgO	20	120	AM
AM002	Fe(30)/V(9)	MgO	20	250	AM
AM003	Fe(9)/V(9)	MgO	20	135	AM
AM004	Fe(20)/V(9)	MgO	20	150	AM
AM005	Fe(9)/V(6)	MgO	20	150	AM

Table 14. Samples grown at University of Konstanz. Descriptions as in the previous table.

Film	Description	substrate	repeats	T_g [°C]	responsible
M065	Mn(30)/Fe(30)	Ge	16	RT	JP
M067	Mn(10)/Fe(10)	Ge	46	RT	JP
MF50	Mn(50)/Fe(50)	Ge	12	RT	JP
M116	Cr(40)/Mn(30)	Ge	28	RT	JP
M150	Cr(40)/Mn(20)	MgO	33	RT	JP
M151	Cr(40)/Mn(20)	Ge	33	RT	JP
M152	Cr(40)/Mn(10)	MgO	40	RT	JP
M153	Cr(40)/Mn(15)	Ge	36	RT	JP
M224	Fe(11)/Mn(12.5)	Ge	40	RT	JP
M226	Cr(11)/Mn(12.5)	Ge	40	RT	JP
M231	Fe(11)/Mn(8)	Ge	40	RT	JP
M232	Fe(11)/Mn(5)	Ge	40	RT	JP
M233	V(11)/Mn(8)	Ge	40	RT	JP
M234	Cr(11)/Mn(8)	Ge	40	RT	JP
M235	Cr(11)/Mn(5)	Ge	40	RT	JP
M236	V(11)/Mn(5)	Ge	40	RT	JP
M237	V(11)/Mn(12.5)	Ge	40	RT	JP

Bibliographic Data Sheet **Risø–R–980(EN)**

Title and author(s)

Epitaxy, Thin films and Superlattices

Morten Jagd Christensen

ISBN	ISSN
87–550–2298–7	0106–2840

Dept. or group	Date
Department of Solid State Physics	May 30, 1997

Groups own reg. number(s)	Project/contract No.

Pages	Tables	Illustrations	References
85	14	59	96

Abstract (Max. 2000 char.)

This report is the result of structural investigations of 3d transition metal superlattices consisting of Fe/V, Cr/Mn, V/Mn and Fe/Mn, and a structural and magnetic study of a series of Ho/Pr alloys.

The work includes preparation and characterization of substrates as well as growth of thin films and Fe/V superlattices by molecular beam epitaxy, including in-situ characterization by reflection high energy electron diffraction and Auger electron spectroscopy. Structural characterization has been done by x-ray diffraction and neutron diffraction. The x-ray diffraction experiments have been performed on the rotating copper anode at Risø, and at synchrotron facilities in Hamburg and Brookhaven, and the neutron scattering was done at the Danish research reactor DR3 at Risø. In addition to longitudinal scans, giving information about the structural parameters in the modulation direction, non-specular scans were also performed. This type of scans gives information about in-plane orientation and lattice parameters.

From the analysis, structural information is obtained about lattice parameters, epitaxial strain, coherence lengths and crystallographic orientation for the superlattice systems, except Fe/Mn superlattices, which could not be modelled. For the Ho/Pr alloys, x-ray magnetic scattering was performed, and the crystal and magnetic structure was investigated.

Descriptors INIS/EDB

CHROMIUM; CRYSTAL GROWTH; GERMANIUM; IRON; MAGNESIUM OXIDES; MANGANESE; MOLECULAR BEAM EPITAXY; SUBSTRATES; SUPERLATTICES; THIN FILMS; VANADIUM; X-RAY DIFFRACTION

Available on request from:
Information Service Department, Risø National Laboratory
(Afdelingen for Informationsservice, Forskningscenter Risø)
P.O. Box 49, DK–4000 Roskilde, Denmark
Phone (+45) 46 77 46 77, ext. 4004/4005 · Fax (+45) 46 75 56 27 · Telex 43 116